2011

Multilayered Planar Periodic Subwavelength Microstructures For Generating And Detecting Circularly Polarized Thermal Infrared Radiation

Samuel Lanning Wadsworth
University of Central Florida

MULTILAYERED PLANAR PERIODIC SUBWAVELENGTH MICROSTRUCTURES FOR GENERATING AND DETECTING CIRCULARLY POLARIZED THERMAL INFRARED RADIATION

by

SAMUEL LANNING WADSWORTH
B.S. University of Rochester, 2006
M.S. University of Central Florida, 2010

A dissertation submitted in partial fulfillment of the requirements
for the degree of Doctor of Philosophy
in the College of Optics and Photonics: CREOL & FPCE,
at the University of Central Florida
Orlando, Florida

Summer Term
2011

Major Professor: Glenn D. Boreman

ABSTRACT

Generation and detection of circularly-polarized (CP) radiation in the 8- to 12-μm band of the infrared (IR) spectrum is crucial for polarization sensing and imaging scenarios. There is very little naturally occurring CP radiation in the long-wave IR band, so that useful functionalities may be obtained by exploiting preferential radiation and transmission characteristics of engineered metamaterials. Conventional CP devices in the IR utilize birefringent crystals, which are typically bulky and expensive to manufacture. The operation of these devices is generally optimized at a single wavelength. Imaging in the long-wave IR is most often broadband, so that achromatic CP-device behavior is highly desirable from a flux-transfer viewpoint. Also, size, weight and cost are significant drivers in the design of practical IR systems. Thus a solution is sought with a convenient thin planar form factor. This dissertation will demonstrate a novel planar periodic subwavelength-microstructured approach derived from classical radiofrequency meanderline designs that are able to generate CP radiation over a broad IR band while maintaining a low fabrication profile. We investigate issues regarding efficiency as a function of the number of layers in the device structure; reflective, transmissive, and emissive behavior; strategies for broadband achromatization; and thermal-isolation requirements between the active blackbody reservoir and the top of the planar device, to achieve a given degree of polarization. Theoretical, numerical, and experimental findings are presented that confirm the feasibility of this class of devices for use in a wide variety of situations, from polarization imaging and spectroscopy to industrial laser processing and machining.

This dissertation is dedicated to the memory of David J. Van Blerkom, a man of wit, humor, and infinite insight. May he rest in eternal peace.

ACKNOWLEDGMENTS

There are several persons that I wish to thank who helped me with the related research and work included in this dissertation. First and foremost, Dr. Glenn D. Boreman deserves a huge amount of credit for allowing me the unique opportunity to learn and experience first-hand independent research in the IR Systems Lab. Without his vision, guidance, and patience, none of this would have ever been possible.

I would especially like to thank Guy Zummo for assisting in many experimental endeavors, facilitating repairs of the fabrication equipment in the IR Systems Lab cleanroom, and training on measurement and deposition systems. I also express gratitude for Dr. Ivan Divliansky, who personally trained me on proper use of the Leica electron-beam lithography system, as well as helping with fabrication-related problems and research efforts. Furthermore, I acknowledge Ed Dein for training and assistance with the dual-gun UHV e-beam evaporator.

As far as collaborative efforts are concerned, I acknowledge Alan Rakes from DRS Optronics Division and Dr. Larry Pezzaniti from Polaris Sensor Technologies Inc. for tasking challenging design and fabrication endeavors that focus upon optimized real-world system performance.

Both present and past members of the IR Systems Lab have contributed to this dissertation in some way, shape, or form. They are Dr. Jeff Tharp, Dr. James Ginn, Dr. David Shelton, Dr. Javier Alda, Dr. Brian Slovick, Dr. Peter Krenz, Dr. Wilson Caba, Dr. Ed Kinzel, Lauren Rich, Joseph Shalenko, Dr. Jeffrey Bean, Dr. Brian Lail, Jeff D'Archangel, LtC. Louis

Flourence, Alex Dillard, Larry Schneider, Ismael Quijano, Robert Brown, Daniel Mullally, and Bill Franklin.

I would also like to acknowledge the members of my dissertation committee, which consists of my advisor Dr. Glenn Boreman, Dr. Aristide Dogariu, Dr. Winston Schoenfeld, and Dr. Brian Lail.

Finally, I am ever grateful for my parents and family members for supporting me throughout the dissertation writing process.

TABLE OF CONTENTS

LIST OF FIGURES

LIST OF TABLES

LIST OF SYMBOLS/ABBREVIATIONS

Al..... Aluminum

AR..... Axial Ratio

ARC..... Anti-Reflection Coating

Au..... Gold

β..... Wave Propagation Constant

BaF_2..... Barium Fluoride

BCB..... Benzocyclobutene

CdS..... Cadmium Sulfide

CMOS..... Complementary Metal-Oxide-Semiconductor Process

CP..... Circular Polarization/Circularly Polarized

CO_2..... Carbon Dioxide

δ..... Differential Phase Shift/Phase Retardance

DUT..... Device Under Test

ε_0..... Permittivity of Free Space

e-beam..... Electron-Beam

EMT..... Effective Medium Theory

EOT..... Extraordinary Optical Transmission

F/#..... F-number

FF..... Fill-Factor

FDT..... Fluctuation-Dissipation Theorem

FDTD ..... Finite-Difference Time Domain

FEM ..... Finite Element Method

FIB ..... Focused Ion-Beam

FPA ..... Focal Plane Array

FSS ..... Frequency Selective Surface

Γ ..... Amplitude Reflection Coefficient

HFSS ..... High-Frequency Structure Simulator

HgCdTe ..... Mercury Cadmium Telluride

IR ..... Infrared

IR-VASE ..... Infrared Variable-Angle Scanning Ellipsometry

k ..... Wave Propagation Vector

λ ..... Free-Space Wavelength of Light

LC ..... Liquid Crystal

LHCP ..... Left-Handed Circularly Polarized

LP ..... Linear Polarizer

LWIR ..... Long-Wave Infrared

MoM ..... Method of Moments

MWIR ..... Mid-Wave Infrared

μm ..... Micron/Micrometer (10^{-6} meters)

Ni ..... Nickel

NIR ..... Near-Infrared

p – polarized ..... Polarization Component in the Plane of Incidence

PhC.....Photonic Crystal

PMM ..... Periodic Method of Moments

PSA .....Polarization State Analyzer

ψ .....Auxiliary Angle of Polarization Ellipse

QWP.....Quarter-Wave Plate/Retarder

RF.....Radio-Frequency

RHCP .....Right-Handed Circularly Polarized

s – polarized .....Polarization Component Perpendicular to the Plane of Incidence

SEM ..... Scanning Electron Microscopy

SPP.....Surface Plasmon Polariton/Surface Phonon Polariton

τ .....Amplitude Transmission Coefficient

TE.....Transverse Electric

THz ..... Terahertz (10^{12} Hertz)

Ti .....Titanium

TM..... Transverse Magnetic

TMM ..... Wave Transmittance Matrix Method

UHV ..... Ultra-High Vacuum

ω .....Angular Frequency of Radiation

Z_0 ..... Characteristic Free-Space Impedance (377 Ω)

ZEP 520-A7 .....Methyl Styrene/Chloromethyl Acrylate Copolymer

CHAPTER 1: INTRODUCTION

1.1 Rudimentary Foundations of Electromagnetic Field Polarization

Polarization is one of the most fundamental characteristics of propagating fields and waves. It is employed throughout all forms of physics that attribute wave-like behavior to common observables that can be described in vector field notation [1–10]. In the most complex of scenarios, a full three-dimensional formalism is required to describe the polarization of a given field distribution [5,6]. However, we will abide by a simple two-dimensional description of optical wave polarization, which effectively describes the trace of the electric field vector as the field propagates through space [3,7–9]. This formalism is acceptable since a) light is an electromagnetic wave whose propagation is governed by the vector Helmholtz equation, and b) an arbitrary distribution of waves can be written as a discrete summation of plane waves over an angular spectrum of spatial frequencies [3,8–10]

$$\vec{E} = \sum_n E_n \cdot \hat{e}_n \cdot \exp(i \cdot (\vec{k}_n \cdot \vec{r} - \omega t)) . \tag{1}$$

The above expression not only satisfies Helmholtz wave propagation equation, it also showcases the polarization basis vector $\hat{e}_n$, whose orientation must be orthogonal to the propagation wave vector $\vec{k}_n$ by way of Maxwell's divergence formulas, otherwise known as the transversality requirement [1–3]

$$\hat{e}_n \cdot \vec{k}_n = 0 . \tag{2}$$

Thus, the field polarization basis is orthogonal to the direction of propagation, and exists within the plane of constant phase.

To get a better picture of just how polarization is defined within a two-dimensional geometric plane, the electric field vector of Equation 1 can be decomposed into respective *s* and *p* – polarized amplitude components of the field, which upon multiplication with the complex conjugate of the total field (and some additional manipulation), yields the normalized intensity distribution that obeys the equation of an ellipse

$$\frac{E_s^2}{E_{0s}^2} + \frac{E_p^2}{E_{0p}^2} - 2\frac{E_s E_p}{E_{0s} E_{0p}} \cos\delta = \sin^2\delta \,. \tag{3}$$

In the previous formula, E_{0s} and E_{0p} are the electric field amplitudes in the *s* and *p* coordinate directions, and δ is the differential phase shift between the two orthogonal amplitudes, such that $\delta = \delta_s - \delta_p$ [3,7–9]. This is the characteristic polarization ellipse of the optical field, which is shown below on Figure 1.

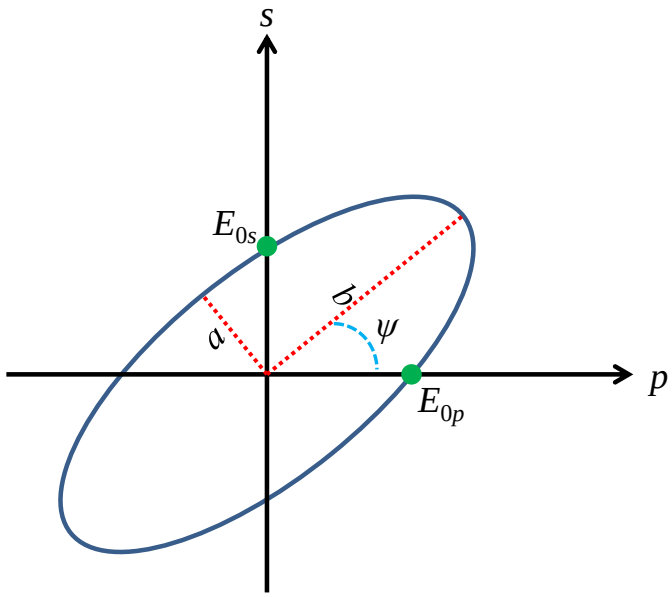

Figure 1: Polarization ellipse of optical field, with parameters described in the text.

With regard to the geometrical description of the polarization ellipse, there are a few related parameters that determine the orientation and evolution of the polarization basis vector as the field propagates through space. Specifically, as shown in Figure 1, the auxiliary angle ψ defines the ratio between *s* and *p* – polarized amplitudes, since

$$\tan\psi = E_{0s}/E_{0p}\,, \tag{4}$$

and the ratio between major (*b*) and minor (*a*) axes of the polarization ellipse is given as

$$AR = b/a = 1/\tan(0.5\cdot\arcsin[\sin(2\cdot\psi)\cdot\sin\delta])\,. \tag{5}$$

The axial ratio (AR) in Equation 5, along with the phase shift δ, can completely determine any state of the polarization ellipse defined by Equation 3 [8,9]. This is because the AR defines the two-dimensional equivalent of the boundary of the polarization ellipse, whereas the phase shift δ (or phase lag) dictates the eccentricity of the elliptical shape that describes the evolution of the polarization basis vector. Thus, upon propagation of the optical wave given by Equation 1, the trace of the electric field is able to take on different shapes defined by the parameters of the characteristic polarization ellipse of Equation 3. The following table illustrates this concept and defines the fundamental states of polarization for specific values of AR and δ.

Table 1: Discrete states of the polarization ellipse.

Polarimetric Values	**State of Polarization**	**Depiction of Polarization**
$\delta = 0$, AR = 0	Linear *s* – polarized	
$\delta = 0$, AR = ∞	Linear *p* – polarized	
$\delta = 0$, AR = +1	Linear +45° polarized	
$\delta = 0$, AR = –1 or $\delta = \pi$, AR = +1	Linear –45° polarized	
$\delta = \pi/2$, AR = +1	Right-handed circular polarized	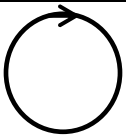
$\delta = -\pi/2$, AR = +1	Left-handed circularly polarized	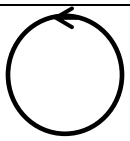
$0 < \delta < \pi$, $0 < AR < \infty$	Right-handed elliptical polarized	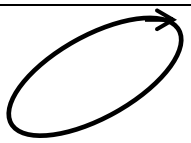
$0 > \delta > -\pi$, $0 < AR < \infty$	Left-handed elliptical polarized	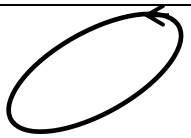

Although this is sufficient information for classifying any state of polarization, there are other methods that are more suitable for systems-level description of how optical components can change or alter the polarization basis upon interaction with an incident field.

1.1.1 Stokes Vector Notation for Optical Polarization

The change in polarization upon transmission through, or reflection from, an arrangement of optical system components can be formulated by a system of matrices that effectively models the modulation of the optical intensity associated with each discrete polarization state [3,7–9]. This is especially useful for physical measurements that quantify the state of polarization, since intensity can always be determined with the appropriate detection system at infrared (IR) or visible wavelengths. Amplitude quantities, such as those demonstrated previously, are not immediately resolvable due to the rapid field oscillations associated with IR and visible frequencies.

Intensity-based polarization is the most common method of acquiring and evaluating the polarization signature of measured optical fields, and can thus be represented in vector notation by the corresponding Stokes vector coefficients

$$\bar{S} = \begin{bmatrix} S_0 \\ S_1 \\ S_2 \\ S_3 \end{bmatrix} = \begin{bmatrix} E_{0s}^2 + E_{0p}^2 \\ E_{0s}^2 - E_{0p}^2 \\ 2E_{0s}E_{0p}\cos\delta \\ 2E_{0s}E_{0p}\sin\delta \end{bmatrix} = \begin{bmatrix} I_s + I_p \\ I_s - I_p \\ I_{+45} - I_{-45} \\ I_{RHCP} - I_{LHCP} \end{bmatrix}, \tag{6}$$

where S_0 is the total intensity, S_1 is the intensity associated with *s* or *p* linear polarization, S_2 indicates the amount of linear polarization oriented at a ±45° angle, and S_3 portrays the quantity of right-handed or left-handed circular polarization (RHCP, LHCP), respectively [3,7–9]. In addition to the polarization ellipse parameters that are included in Equation 6, notice how each of the Stokes parameters, aside from S_0, are defined by subtractive differences between the intensities of orthogonal polarization states. Not surprisingly, this originates from the

fundamental interference laws of Fresnel and Arago for partially-polarized light, which G.G. Stokes incorporated into his mathematical description of optical polarization [8,9].

To account for a change in the polarization signature upon transmission through an optical system, the final state of polarization can be obtained via a successive multiplication of matrices that resemble the characteristics and behavior of each optical element that the field encounters. Since the Stokes vector is represented by the 4 element column vector of Equation 6, the corresponding Mueller matrix of a system component would be given by a 4 by 4 matrix that acts directly upon the input Stokes vector [3,8,9], such that

$$\bar{S}_{out} = \bar{M}_N \cdot \bar{M}_{N-1} \cdot \ldots \cdot \bar{M}_2 \cdot \bar{M}_1 \cdot \bar{S}_{in}, \tag{7}$$

where $\bar{M}_N$ is the last matrix in a system of N components. Aside from effectively modeling the evolution in polarization through an optical system, this convention forms the basis for all polarimetry-related measurements that will be discussed throughout this dissertation.

1.1.2 Detection, Generation, and Uniqueness of Circular Polarization

With regard to all possible states of polarization that can be expressed by the polarization ellipse of Equation 3, circular polarization (CP) is inherently unique in that it is the only state that scribes a circular path within the two-dimensional plane of constant phase. In terms of the ellipse parameters, it can be effectively achieved by an AR of 1 and a δ of $\pm\pi/2$, depending upon which handedness is preferred (see Table 1). Since both field amplitudes are the same and the field vector rotates consistently as the electromagnetic wave propagates through the system, CP achieves a level of uniformity that provides equal *s* and *p* amplitudes that are out of phase by a

quarter of a wave [7–9]. This is actually quite useful and often necessary for many applications that require polarization uniformity from CP light. However, we must first be able to both generate and detect CP that can be utilized in such situations.

The basic principle behind the detection of a randomly polarized field consists of separate intensity-based measurements using specified orientations of polarization-sensitive components. As depicted in Figure 2, a simple measurement setup is comprised of a linear polarizer (LP) and quarter-wave plate (QWP), where upon the impinging optical field encounters the QWP first before proceeding on towards the LP and, eventually, the detector.

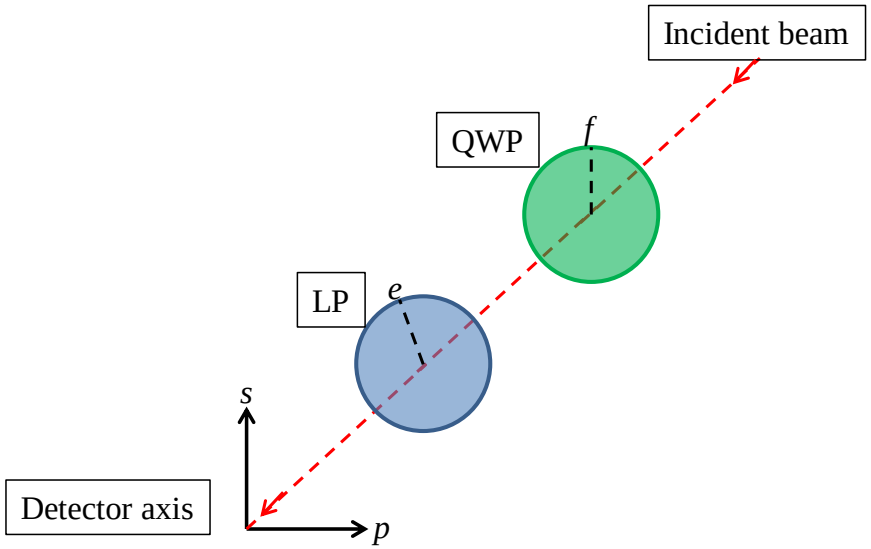

Figure 2: Measurement setup for determination of Stokes parameters, where LP is a linear polarizer with extinction axis *e*, and QWP is a quarter-wave plate with fast axis *f*.

The canonical equations that embody the detection of the Stokes parameters are given by the addition and subtraction of intensities measured with the polarizing components in specific configurations

$$I(\theta = 0^\circ, \delta = 0) + I(\theta = 90^\circ, \delta = 0) = S_0, \tag{8}$$

$$I(\theta = 0^\circ, \delta = 0) - I(\theta = 90^\circ, \delta = 0) = S_1, \tag{9}$$

$$I(\theta = 45^\circ, \delta = 0) - I(\theta = 135^\circ, \delta = 0) = S_2, \tag{10}$$

$$I(\theta = 45^\circ, \delta = \pi/2) - I(\theta = 135^\circ, \delta = \pi/2) = S_3, \tag{11}$$

where θ is the angle of the transmittance axis of a LP, and $\delta = \pi/2$ is representative of the QWP element that is inserted just before the LP [3,8]. Interestingly enough, Equation 11 is the only measurement routine that requires the QWP component, since the others do not need an additional quarter-wave phase shift for detection of S_0 through S_2. Thus, the QWP is absolutely essential for detection of the intensity associated with CP. Moreover, it also has to be utilized in the generation of CP, since the Mueller matrix system equation that acts upon a randomly polarized beam can be expressed as

$$\overline{M}_{QWP} \cdot \overline{M}_{LP}(\theta = 45^\circ) \cdot \overline{S}_{in} = 0.5 \cdot [S_0 + S_2 \;\; 0 \;\; 0 \;\; -(S_0 + S_2)], \tag{12}$$

where $\overline{M}_{QWP}$ and $\overline{M}_{LP}$ are the Mueller matrices for a QWP and LP, respectively [8]. The output Stokes vector of Equation 12 can be normalized by $S_0 + S_2$, which yields perfect CP. Therefore, QWPs are the mainstay for detection and generation of light that has a significant investment in S_3.

1.2 Classical Optical Elements for Modulation and Detection of CP Fields in the IR

In general, a QWP, or quarter-wave retarder, is a functional optical device that provides a $\pi/2$ phase shift between orthogonal components while maintaining an AR of 1 between the transmitted or reflected fields [3,7,8]. Its name stems from the fact that it delays the phase

between the two perpendicular components by a quarter of a wave, which is exactly similar to the conditions imposed by a propagating CP field. Thus, the QWP is irrefutably tied with the physical mechanism of CP light, which makes it indispensible for applications relating to the detection or modulation of CP. Of the purported mechanisms that enable QWP behavior, we shall first concentrate on the so-called 'classical' material systems that were developed and proposed many years before the recent growth in nanostructured materials research. Specifically, classical optical QWPs for the IR spectrum present their own set of unique challenges in the design and manufacturing of such components, particularly because of the limited availability of materials that exhibit QWP characteristics and suitable power transmission that would match customer or system specifications.

1.2.1 Crystalline Waveplates

Optical crystals that are utilized in QWPs exhibit a physical phenomenon known as birefringence, which is that orthogonal components of light travel at different phase velocities due to the anisotropy of the respective crystal axes [7,8,10]. If a given crystal has separate refractive indices associated with each orthogonal crystal axes, then the phase lag accumulated upon propagation through the medium can be expressed as

$$\delta = (2\pi/\lambda)\cdot(n_e - n_o)\cdot d\,, \tag{13}$$

where λ is the free-space wavelength of light, n_e and n_o are the extraordinary and ordinary refractive indices of orthogonal crystal axes, and d is the thickness of the material [7,8]. The ordinary and extraordinary refractive indices are differentiated by the effective speed at which

light can propagate along the respective crystal axis. In most cases, $n_e > n_o$, so the phase velocity would be greater along the axis corresponding to the ordinary refractive index.

In the design of crystalline QWPs, specifically for IR wavelengths, one encounters a number of problems related to the materials engineering, spectral, and angular performance. First off, there are only a few select materials that exhibit appropriate birefringence in the IR regime, and even so, there is an intrinsic finite difference between the ordinary and extraordinary refractive indices, meaning that most of the engineering work comes from tuning the thickness d so that QWP behavior ($\delta = \pi/2$) is attained. If we use quartz as an example, the difference between ordinary and extraordinary indices at 3.39 μm wavelength is [11]

$$n_e - n_o = 0.0065 \pm 0.0001. \tag{14}$$

Inserting this information into Equation 13 yields approximately 130 μm for the required thickness. As far as material stability is concerned, this presents a vital predicament in that a true 0^{th}-order waveplate at 3.39 μm would be extremely thin, fragile, and therefore susceptible to mechanical stresses. Although one could add 2π radians to the left-hand side of Equation 13, which would increase the effective thickness, the QWP would no longer be a true 0^{th}-order retarder, and would exhibit severe amounts of dispersion even over a narrow waveband [8,9,11–13]. This is shown in Figure 3, which plots the phase retardance against the normalized wavelength for 0^{th} and multi-order waveplates. The slope of each curve is proportional to $1/\lambda$, since the derivative of Equation 13 with respect to wavelength results in a $1/\lambda$ term that is multiplied by the *total* phase shift provided by the wave retarder [12,13].

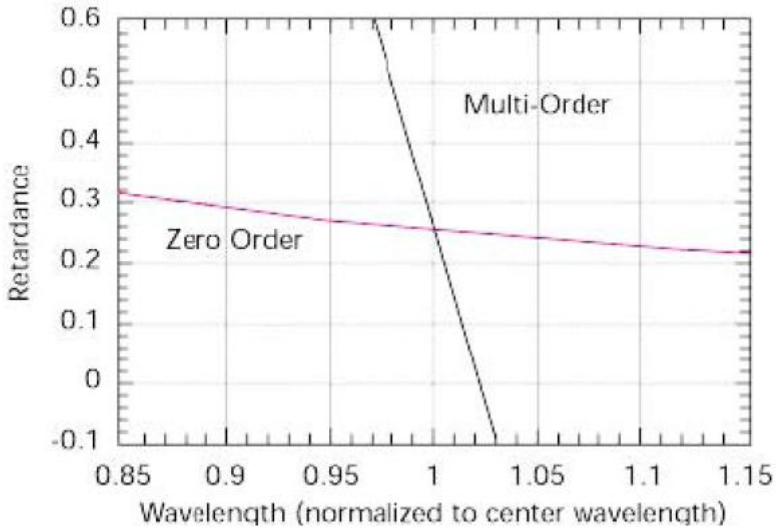

Figure 3: Dispersion of phase retardance for zero and multi-ordered crystalline waveplates (from [12]).

In addition to the spectral instability of the phase retardance, crystalline waveplates also suffer from being extremely dependent upon the angle of incident illumination [12,13]. As shown in the following figure, 0^{th}-order waveplates are actually more sensitive to oblique angles than multi-order retarders, although both are hardly ideal for applications that require a broad angular spectrum of incident radiation. Notice how the phase retardance shifts by $\lambda/10$ with only a slight tilt of 10° along either crystal axis.

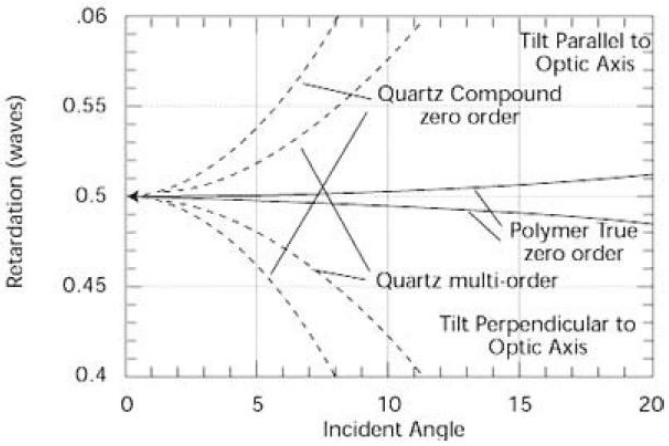

Figure 4: Angular sensitivities of common wave retarder materials (from [12]).

We shall now discuss a few other complications in the performance and manufacture of crystal QWPs for the IR spectrum, the most significant of which is the material properties. The optical properties of birefringent quartz presents a good example, because not only is the phase shift dependent upon the wavelength of operation, but the power transmission actually cuts off just below 5 μm [14,15]. This behavior is characteristic of all such oxide crystals in the IR, which increases the difficulty in locating a suitable birefringent crystal for long-wave infrared (LWIR, 8 – 12 μm) applications. Although there are crystalline materials that function as waveplates in the LWIR, such as cadmium sulfide (CdS), the transmittance is limited by the Fresnel scattering coefficients at each interface, which would require the application of an anti-reflection (AR) coating to increase the power transmission to appropriate levels. Unfortunately, this also increases the cost and complexity of fabricating CdS QWPs for the LWIR band, not to mention the potential sensitivity to incident angles and spectral wavelengths that would be introduced by the addition of the AR coating. Therefore, because of the expensive and fragile manufacturing process, QWPs for the LWIR are typically fabricated for placement within a 1

inch diameter mount that is more suitable for single-wavelength bench-top laser operation. Figure 5 depicts a crystalline QWP in a standard mount, which effectively limits the potential area of illumination and angular spectrum (or numerical aperture) of a converging focused beam.

Figure 5: QWP component in a standard mount, which limits the effective numerical aperture of an incoming beam (image taken from http://www.iiviinfrared.com/waveplates online).

Because of the aforementioned limitations on crystalline QWPs for the IR, it would behoove us to search for more effective solutions that could overcome the characteristic disadvantages of spectral, angular, and material sensitivities.

1.2.2 Reflective Prism Thin Film Retarders

Phase retardation between two orthogonal field components can arise from other physical mechanisms other than birefringence, which is exclusively limited to anisotropic material systems. A simple case of this can be found in the fundamental Fresnel scattering equations for reflected polarized amplitudes from a planar interface

$$\Gamma_s = \frac{n_1 \cdot \cos\theta_i - n_2 \cdot \cos\theta_t}{n_1 \cdot \cos\theta_i + n_2 \cdot \cos\theta_t}, \tag{15}$$

$$\Gamma_p = \frac{n_1 \cdot \cos\theta_t - n_2 \cdot \cos\theta_i}{n_1 \cdot \cos\theta_t + n_2 \cdot \cos\theta_i}, \tag{16}$$

where n_1 and n_2 are the refractive indices of the incident and transmitted medium, θ_i and θ_t are the incident and transmitted angles with respect to the surface normal, and Γ_s and Γ_p are the *s* and *p* – polarized amplitude reflection coefficients, respectively [3,7–10]. The incident and transmitted angles are related by Snell's law of refraction, $n_1 \cdot \sin\theta_i = n_2 \cdot \sin\theta_t$. In a reflective multilayer optical system, the complex amplitudes of Equations 15 and 16 can be modified by altering the incident angle and optical path length that accrues over multiple reflections. By doing so, the phase differential between *s* and *p* – polarized amplitude components of the reflected field can be tuned to a value of π/2, the necessary requirement for QWP operation. However, the trick in this instance is to engineer such a system that would utilize the phase retardance upon reflection while maintaining an AR of 1 and a high power throughput.

The most common form of reflective IR QWPs presented in the literature have been comprised of multiple prisms [16–18], both without and with thin-film layers [19,20] that are designed to impart a phase retardance between the optical path lengths of the reflected *s* and *p* – polarized modes. The advantage of using prisms comes from their versatility in controlling the output angle and orientation of the CP field. Although the standard configuration of reflection from a 45° angle of incidence has been demonstrated [18,20], other orientations are feasible with re-arrangements to the system of prims and thin film layers. As an example, this allows for the light path to continue in its original trajectory [17,19], which is preferable for some optical system designs. Additionally, reflective prism QWPs have exhibited achromatic phase retardance over a given IR band [18,20], which is a drastic improvement over the spectrally dependent

behavior of crystalline QWPs. The power reflection coefficients for both *s* and *p* polarizations have also been optimized for their fullest potential.

With the aforementioned benefits of reflective prism thin-film QWPs for the IR, one would presume that their acceptance would be widespread across industry and academia. However, their usefulness only comes across in certain situations, since most prism retarders are expensive to manufacture and rather bulky in size, which limits the number of systems for potential integration. Their size is the most limiting constraint, as shown in Figure 6, since the majority of optical systems for IR polarization analysis, or polarimetry, expect the QWP and other polarizing components to be placed just before the focal plane array (FPA) detector. Unfortunately, this aspect is unavoidable, since multiple prisms and reflections within are necessary for obtaining the $\pi/2$ phase differential, although this adds significantly to the cost, weight, and size of the corresponding optical system that would contain such QWP technology.

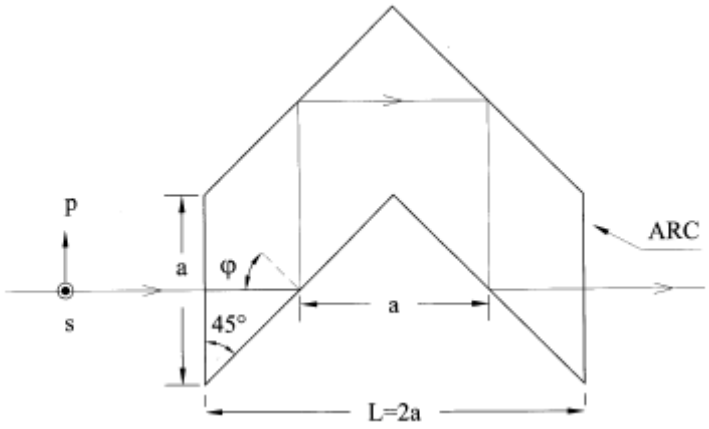

Figure 6: In-line chevron prism retarder, which consists of multiple prisms and an anti-reflection coated (ARC) side, which adds to the expense of the component (from [17]).

1.2.3 Birefringent Films and Liquid Crystals

As an alternative to crystalline retarders in the IR, birefringent films and liquid crystals (LCs) have been proposed for QWP operation, since the physical mechanism of phase retardance originates from the same exact principle of material index anisotropy [21–25]. Though LCs have been used extensively in the visible as phase shifting devices, especially for flat panel display technologies [21,22], their use in the IR hinges upon the achromaticity of the differential phase shift and power transmission that can be extracted over a given waveband. LCs and polymer films are very similar in their physical composition, in that dipole-shaped molecules are arranged in a lattice configuration while suspended in an immersion dielectric fluid or film, as Figure 7 demonstrates.

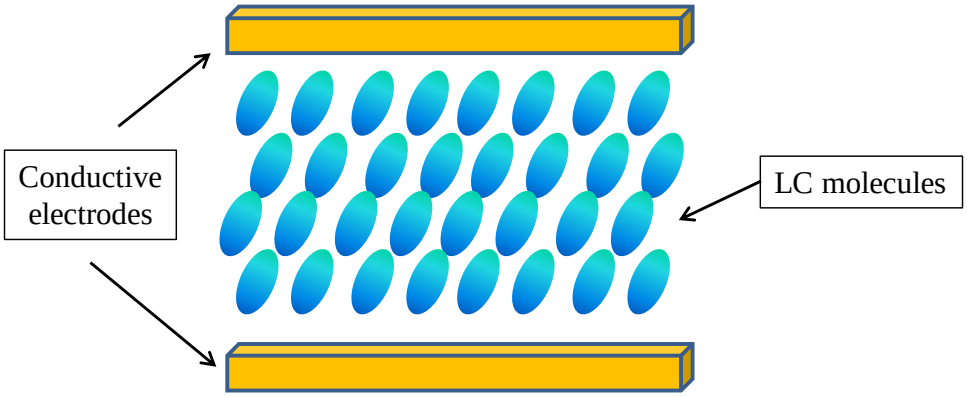

Figure 7: Schematic of LC system consisting of dipole-shaped LC molecules, whose orientation is controlled by an applied voltage between the two conductive electrodes.

In the case of LCs, the material anisotropy can be controlled by applying a voltage between two conducting plates that bound the medium, which helps to orient the dipole-shaped molecules and effectively tune the birefringence [24]. This is inherently useful in applications where the center operational wavelength changes, such that the birefringence can be controlled to achieve the

intended QWP behavior at a given wavelength. Like most birefringent medium, the phase retardance from LCs and polymer films exhibits spectral dispersion, although not as much as crystalline waveplates. This spectral dispersion can be augmented to result in a near-achromatic phase shift with the inclusion of multiple layers of LCs or polymer films [21]. Although birefringent polymer films are, by definition, not tunable in the same sense as LCs, the desired phase retardance can be obtained by simply rotating the polymer film until the necessary birefringence is achieved [25]. Furthermore, as shown on Figure 4, the angular sensitivity of 0^{th}-order polymer and LC films is extremely attractive for applications that feature high numerical aperture focusing objectives or a wide angular spectrum of incident radiation.

It would seem that polymer and LC technologies cover all the necessary features of device performance that were lacking in bulk crystal wave retarders, especially since LC polymer films can be integrated onto any transparent substrate while maintaining a low profile. In retrospect, this is the closest to an ideal QWP for the IR as one can achieve without having to resort to micro-structured surfaces and materials. Nonetheless, there are some deficiencies associated with this technology, most of which are related to power transmission throughput of the LC and polymer materials. Birefringent polymer films in particular have exhibited very poor transmittance in the IR due to the material absorption associated with OH^- vibrational/rotational phonon modes [23,25]. In contradistinction, LCs do not retain so much absorption as polymer films, although the multiple layers of LC film required for achromatic phase retardance could severely degrade the transmission throughput. Since a single ideal LC layer exhibits approximately 10% power attenuation [24], the 5 or 6 layers required for a spectral dispersion-free phase shift [21] would limit the amount of power that could be detected by an IR FPA

system. Thus, the desired achromatic QWP characteristics and high percentage of power transmission would have to be simultaneously achieved by some other method.

1.3 Novel Subwavelength Microstructures as QWPs and Phase Retarders

The advent of microstructured optical devices changed the landscape of what was possible regarding the control of light on a microscopic scale [26]. This revolution and discovery of optical effects that could be manipulated at a subwavelength scale heralded the implementation of novel devices and materials, such as photonic crystals, diffractive optical elements, metamaterials, and other microstructures [26–76]. Not surprisingly, polarization modulation was one of the principle applications imposed on the first subwavelength gratings fabricated for IR and visible wavelengths [27–34]. Since then, a wealth of new designs for submicron gratings, photonic crystals, and metamaterials, have garnered new interest in attempting to engineer QWPs and circular polarizers that would exhibit broadband achromatic characteristics while maintaining a high percentage of power throughput. Other performance metrics, such as angular sensitivity and ease of fabrication/integration into an optical system, have also been considered in the design of such structures. Therefore, what follows is a brief overview of the current technologies that have been proposed for subwavelength microstructured QWPs and circular polarizers for operation in the thermal IR bands.

1.3.1 Form-Birefringent Retarders

Birefringence is the most fundamental phenomenon for obtaining a differential phase shift between two orthogonal field components, so it is only natural that we attempt to engineer such a microstructure that replicates this exact physical mechanism. One of the most important optical effects that is exploited by subwavelength microstructures is the Maxwell-Garnett effective medium theory, which yields a macroscopic value for the refractive index that can be specifically designed and adjusted by changing the composition of subwavelength features that comprise the bulk medium [10,26]. From-birefringent retarders make use of this effect to emulate birefringence on a macroscopic scale by fabricating high aspect-ratio anisotropic gratings from a high-index material, the subwavelength nature of which provides an effective refractive index over the depth of the grating [27–34]. The grating periodicity and amplitude, among other parameters, can be designed with a certain wavelength spectrum and differential phase retardance in mind, so this technology has immediate implications for the visible and IR spectrums. A scanning electron microscope (SEM) image of a sample form-birefringent grating is shown below in Figure 8.

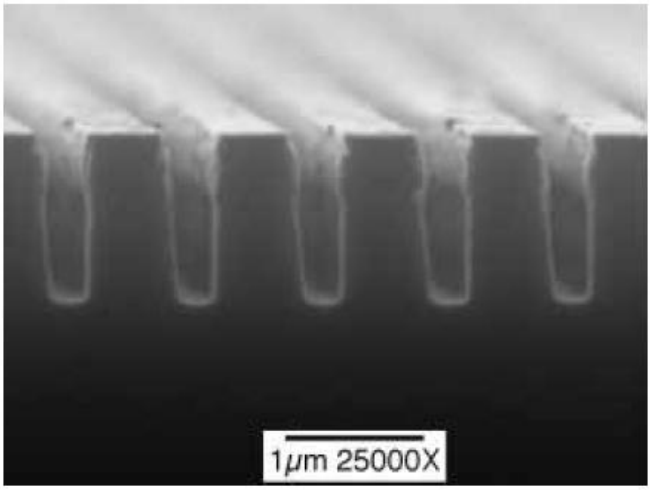

Figure 8: Form-birefringent QWP (from [27]).

If the percentage of surrounding filling material within a single periodic unit cell of the structure can be quantified by the value *FF*, then the effective refractive indices of the *s* and *p* – polarized modes can be formulated as

$$n_s = (n_1^2 \cdot FF + n_2^2 \cdot (1 - FF))^{1/2}, \tag{17}$$

$$n_p = ((1/n_1^2) \cdot FF + (1/n_2^2) \cdot (1 - FF))^{-1/2}, \tag{18}$$

where n_1 is the index of the surrounding material adjacent to the grating (usually air), and n_2 is the index of the grating material, which is normally selected as a high-index, yet transparent, semiconductor substrate [27–31]. The choice of a semiconductor material for the substrate facilitates fabrication of the subwavelength gratings by anisotropic reactive etching methods [27–29,32,34], and allows for subsequent integration onto any conceivable optical system component or multilayer photonic material system. Such attributes have prompted extensive investigations into form-birefringent structures as QWPs for the IR spectrum, where they have found particular use in imaging polarimetry systems [35,36,38].

The measured differential phase shift and transmittance of subwavelength form-birefringent gratings, such as the one shown in Figure 8, have been demonstrated as being significantly superior to bulk crystalline retarders in the IR regime. References [27] and [34] specifically show modeled and measured achromatic QWP behavior from the retrieved phase retardance of form-birefringent gratings for the mid-wave infrared (MWIR, 3 – 5 μm) band. The transmitted power is also appropriate for use in high-throughput systems, although the measured value of approximately 60%, which originates from the Fresnel reflections off the back side of the substrate [27,34,35], could be improved by the application of a broadband anti-reflection coating (ARC). However, to the best of our knowledge, angular sensitivity of the polarization and transmission metrics of form-birefringent retarders have not been evaluated in either numerical simulations or experimental measurements. A typical measurement routine of form-birefringent gratings is performed in collimated space [34,35], which limits the incident angles to those that are purely normal to the surface of the grating. Therefore, there could be a significant variation in performance when oblique incidence angles are factored into the assessment of such devices. Regardless, subwavelength form-birefringent retarders hold a veritable promise of replacing conventional crystalline waveplates in the thermal IR, especially where polarization imaging applications and low-profile device integration are of utmost importance.

1.3.2 Metamaterials, Photonic Crystals, and Microstructured Surfaces

From here onwards, we shall mention a few other technologies and material systems for subwavelength IR QWP components that have not received as much attention as form-

birefringent gratings, particularly with respect to functionality and feasibility of device integration into thermal polarimetry imagers. Photonic crystals (PhCs) comprise a general class of microstructured material that exhibits a spatially varying dielectric function with a pre-defined periodicity, which allows for the formation of photonic band gaps that forbid light propagation within a certain frequency band and spatial wavevector spectrum [37,39–43]. The spatially varying refractive index is enabled by microstructured inclusions and/or fabrications of subwavelength inhomogeneous features that allow for submicron control of light. In addition to the formation of photonic band gaps, this allows for effective control of the refractive indices along specified crystal axes of the PhC, thereby resulting in an artificial birefringent medium. Alternatively, QWP characteristics can also be acquired by the realization of polarization band-gaps in a PhC, which can effectively isolate the right-handed or left-handed CP spectrum of the transmitted signal [37]. In the present literature, the majority of PhC waveplates have been investigated as numerical studies purely for feasibility and design concerns [39,40], with only a few being actually implemented in the radio-frequency (RF), terahertz (THz), and near-IR (NIR) regimes [41–43]. This is most likely due to the complexity of fabrication and difficulty of scattering parameter measurements. Nonetheless, the possibility for design and construction of a PhC QWP in the IR spectrum is wide open for further research, although fabrication would be hindered by increasing complexity and feature size of the two-dimensional or three-dimensional subwavelength photonic lattices.

Another interesting candidate for subwavelength IR QWPs is microstructured surfaces that operate in reflection. Similar to form-birefringent retarders, subwavelength gratings and micromachined surfaces impart a phase retardance to the incident field upon reflection that,

when tuned properly via structural parameter adjustments, can provide the necessary $\pi/2$ phase shift for QWP behavior. The actual physical mechanism in this instance depends upon the type of material that is utilized in the construction of the microstructured surface. For instance, dielectric pillars on a metal substrate can be fashioned to exhibit form-birefringence in reflection, as seen in [44]. However, other structures may entirely consist of highly-reflective metals that are patterned into subwavelength grating features. In this case, the reflected retardance originates from the phase lag between the *s* and *p* – polarized current modes or surface waves that are induced upon the metallic grating elements [45,46]. Whatever the physical principle may be, subwavelength reflective QWPs have been demonstrated as being highly efficient in converting linear polarization into CP at the specified design frequency while simultaneously maintaining high reflectivity [44–46]. The low profile nature of such microstructured subwavelength reflection gratings enables cost-efficient fabrication and integration into compact polarimetry systems. With regard to the spectral performance of microstructured surface-relief gratings, the reflected phase retardance is typically optimized over a very narrow spectrum around the center design wavelength, which limits the functional achromaticity of the reflective QWPs [44,45]. Further investigations may yield improved performance along these lines.

Metamaterials constitute an incredibly wide-ranging tapestry of artificial materials that are comprised of micropatterned subwavelength metallic inclusions, which can be arranged periodically in planar two-dimensional or fully three-dimensional configurations [47–50]. Their periodic nature leads to the formation of phenomena similar to photonic band gaps of PhCs, such that the induced currents and surface waves exhibit plasmonic band gaps that elicit specific control over the excitation frequency and spatial wavevector of surface plasmon polaritons

(SPPs) on the subwavelength conducting metallic elements [47,49,50]. This direct control over the plasmonic behavior of metamaterials allows for the discovery and investigation of other related properties, such as negative refraction [47,51,52], super-lensing [53], second harmonic generation [54], extraordinary optical transmission (EOT) [55,56], and bi-anisotropy [57], to name a few. Not surprisingly, QWPs can be designed with some of these effects in mind, which make metamaterials the most versatile components available for achieving an achromatic CP spectrum.

Although a wide variety of designs and configurations can be considered, we shall focus upon two particular cases that can be differentiated into planar two-dimensional and three-dimensional metamaterials. The most popular example of the latter was recently theorized and fabricated as an array of conducting helical wires that invoke special optical properties, such as bi-anisotropy and polarization-exclusive Bragg reflection, which leads to polarization band gaps [37,58–61]. Figure 9 depicts a helical wire array that was optimized for RHCP transmission in the IR spectrum.

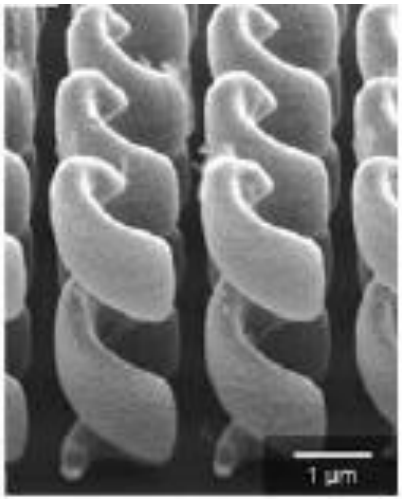

Figure 9: SEM of gold helix photonic metamaterial for broadband IR transmission of RHCP (from [58]).

The obvious limiting factor in this instance is not the performance, but the severe complexity of fabricating such an intricate three-dimensional structure, which was carried out via focused ion beam lithography [58,60]. Thus, even though the polarimetric output parameters may not be as ideal, planar two-dimensional metamaterials serve as a viable alternative that can be easily fabricated and optimized to replicate QWP behavior [62–68]. Furthermore, multiple layers of planar metamaterials can be stratified over each other to provide the necessary differential phase shift while enhancing the transmittance of the multilayer stack [66,72]. Reflective wave retarders comprised of planar metamaterials have also been demonstrated [64]. Physical mechanisms ranging from chirality [65] and effective medium theory (EMT) [67,69] to equivalent circuit models [63,70–73] have been incorporated in the design phase of such structures for achieving optimal polarization and throughput metrics. Along with their compact profile and CMOS-compatible fabrication process, planar two-dimensional subwavelength metamaterials represent a versatile realm of technology that must be considered when discussing potential alternatives to

conventional IR QWPs and circular polarizers. An example of a planar chiral metamaterial waveplate is shown below on Figure 10.

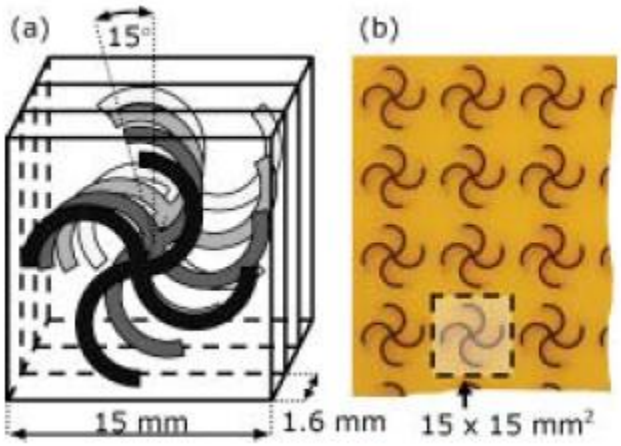

Figure 10: Multilayer planar chiral metamaterial for polarization modulation (from [52]).

Among the prospective technological candidates that have been listed thus far, planar metamaterials represent an area that is unique to subwavelength IR QWPs in that many designs have been offered, but few have been optimized and scrutinized for consideration in broadband thermal imaging systems. Considering the aforementioned advantages, it would behoove us to at least attempt a design that offers achromatic quarter-wave retardance along with the best power throughput possible for optimum system performance. Coincidentally, many two-dimensional metamaterials for polarization modulation "borrow" their designs from planar frequency-selective surfaces (FSSs) that have been presented in the decades prior to the recent expansion in metamaterials and plasmonics-related research. These FSSs can be scaled down from the RF and THz regimes to the IR, thereby providing functional FSS behavior in the IR spectrum [74–76]. In the following chapters, we will employ a specific FSS design that will enable achromatic QWP

behavior in *both* transmission and reflection, along with some other capabilities that have yet to be demonstrated anywhere else.

1.4 Broadband Circularly-Polarized Thermal Emission

As with transmission and reflection, it would also be desirable to control the electromagnetic polarization of thermally emitted fields from subwavelength composite structures. Specifically, a broadband CP signature, such as the one obtained from achromatic circular polarizers and QWPs, is highly coveted not only for reasons stated in Section 1.1.2, but because the generation of CP seldom occurs in the natural thermal ambiance of the IR spectrum (both MWIR and LWIR) [8,9]. Therefore, the construction of an artificial source of CP emission would provide a valid CP target for testing subwavelength QWP components in thermal polarimeters, and would also mark active thermal objects by emitting an artificial CP signature. Such applications pertaining to IR imaging polarimetry and spectroscopy would immediately benefit from devices that could emit a broad spectrum of CP radiation when thermally excited.

In the classical regime, most thermal sources are inherently broadband emitters, which are incoherent and unpolarized by definition [77–79]. However, in recent years, novel subwavelength structures have been shown to exhibit atypical thermal properties, such as polarized coherent directional emission over a narrow spectrum of wavelengths [80,81]. This behavior is due to the excitation of coherent p – polarized surface waves along the interface of the subwavelength grating structure, which a) modify the local optical density of states, and b) coherently interfere in the near field, the sum of which produces a highly-directional narrow-

band linear-polarized thermal source that can be observed in the far field [80,81]. Because such structures resemble the form-birefringent gratings of the previous section, it would be interesting to evaluate the polarization-dependent thermal properties of other subwavelength microstructures, such as planar periodic metamaterials and FSSs. In particular, since multilayered PhCs have already been demonstrated as being capable of emitting a broadband CP signature [82–84], it would be a huge benefit to extract a broadband CP emission spectrum from planar periodic FSSs due to the ease of fabrication and implementation as low-profile thermal targets. Furthermore, experimental studies of CP thermal emission are a rarity as far as literature is concerned [85], so it shall be seen if planar metamaterials and FSSs can yield broadband CP emission and, more importantly, circumvent characteristic theorems and physical laws pertaining to thermal excitation that may impede our progress in obtaining thermally emitted CP fields.

1.5 Thesis

The fundamental goal of this dissertation is to present a novel subwavelength microstructured material system that is able to generate and detect broadband CP radiation in the IR spectrum. Due to its versatility and compactness, a planar periodic subwavelength FSS design shall be proposed in the form of a meanderline grating. This structure shall be explored in depth with regard to its functional behavior and design, and will be implemented as multilayer transmissive and reflective achromatic quarter-wave retarders for converting linear polarization into circular polarization over a broad thermal IR waveband. Optimization of the output polarimetric and throughput parameters will be performed where necessary, which will

substantiate comparisons between multilayered meanderline retarders and contemporary alternatives. In addition, the meanderline retarders will also find use in the broadband thermal emission of CP radiation, which is made possible by the inclusion of a thermal isolation layer of aerogel dielectric. All aforementioned multilayered meanderline gratings are fabricated and measured to validate the simulated designs. Additional studies will be presented that consider realistic scenarios and operational situations directly corresponding to pertinent applications of subwavelength meanderline gratings in the IR.

1.6 Prior Publications and Financial Support Disclosure

Portions of this research were originally published and/or submitted to peer-reviewed journals. Specifically, Chapters 2 and 3 include results and related discussions that were documented in [86], [87], and [88], whereas Chapter 4 contains material submitted to [89].

The research that was performed in relation to Section 3.1.3, which pertains to the transmission throughput study of multilayer meanderline retarders, was partially funded by DRS Optronics Division, and the Florida High-Tech Corridor Council.

Additional support, particularly regarding the content of Chapter 4, was provided by the Laboratory Directed Research and Development program at Sandia National Laboratories. Sandia is a multiprogram laboratory operated by Sandia Corporation, a Lockheed Martin Company, for the United States Department of Energy's National Nuclear Security Administration under Contract DE-AC04-94AL85000.

CHAPTER 2: THEORY, DESIGN, FABRICATION, AND CHARACTERIZATION OF MULTILAYERED MEANDERLINE QUARTER-WAVE RETARDERS FOR THE INFRARED

2.1 Theory and Functional Behavior of Multilayer Meanderline Frequency-Selective Surfaces

Contrary to the current perception, metamaterials have existed long before negative refraction was first encountered [47,52,53]. The use of subwavelength structures for modifying the electromagnetic properties of optical fields has been present ever since the 1960's, which coined the word 'frequency-selective surfaces' (FSSs) for such devices [90–92]. Coincidentally, many designs of metamaterial structures found in the current literature originated from FSS work in the radio-frequency (RF) regime [67,93]. The meanderline wave retarder is one such element that has been scaled down in size from the RF to function in the thermal IR band [86,87,94–100].

A meanderline FSS is a patterned subwavelength metallic structure that can be designed and fabricated with multiple layers on a planar substrate. Its behavior is often compared with artificial birefringence, such that an incident linearly-polarized wave encounters a phase delay between two orthogonal field components that are parallel and perpendicular to the meanderline array periodicity [86,94–100]. The fundamental mechanics behind the imparted wave retardance and birefringence can be described by an assortment of methods, such as effective medium theory (EMT), equivalent circuit models, current path-length delay, modal waveguide aperture admittance, and other electromagnetic analysis techniques [86,87,92,94–97,101–103]. Many of these approaches require solving for the field and current distributions on the meanderline FSS elements, which ultimately determines the phase retardance between the scattered field components. However, it is often difficult to analytically verify the magnitude of the imparted

phase delay that originates from the orthogonal surface current elements and field distributions on the meanderline geometry. Such analysis is often relegated to computational techniques, such as the method of moments (MoM), which utilize a generalized scattering matrix approach to solve for the infinitesimal field and current elements on the scattering geometry [90,94,96,97,103]. Therefore, to explain the principles of operation in a more generalized form, the equivalent transmission line circuit model of the meanderline system can be implemented as an effective description of the phenomenological behavior [86,92,94–96]. Such equivalent circuit methods have been often used to determine and validate the behavior of FSSs and metamaterials over a wide range of frequencies [70–73]. The equivalent transmission line circuit of a single meanderline layer is displayed in tandem with a scanning electron micrograph (SEM) image of a meanderline array on Figure 11.

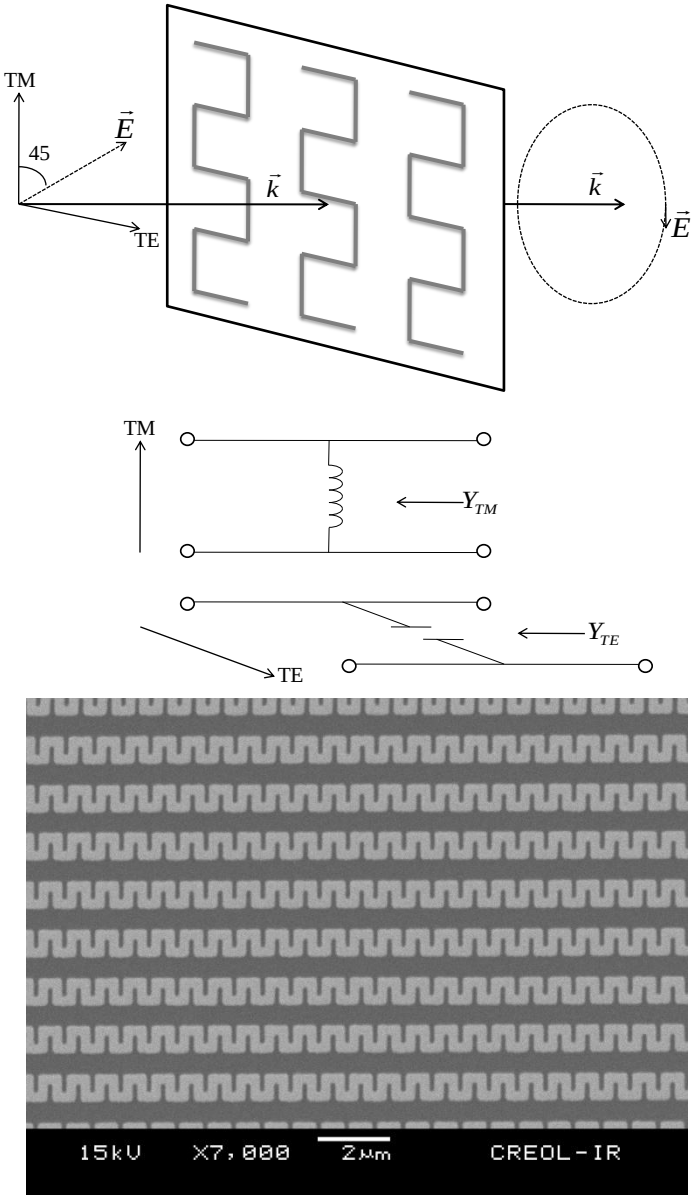

Figure 11: Equivalent circuit model of a meanderline FSS and corresponding SEM image of a single microstructured meanderline layer.

2.1.1 Equivalent Circuit Model for Transmissive Meanderline Retarders

We shall first consider the equivalent behavior of a meanderline FSS that operates in transmission. As will be shown later on, the equivalent transmission line circuit can be thought

of as a lumped (or shunt) impedance discontinuity that represents the ability of an electromagnetic field to impinge upon the corresponding structured surface. Given an incident polarized plane wave upon the meanderline structure, the polarization basis vector can be decomposed into two orthogonal components that are parallel and perpendicular to the meanderline axis. With reference to Figure 11, these components would be in the TM and TE directions, respectively. The polarization field that is parallel to the axis (TM) induces a large resonant current that circulates throughout the conducting meanderline elements, which can be thought of as an equivalent inductive impedance. Likewise, the polarization component perpendicular to the meanderline axis (TE) propagates between parallel segments of the meanderline circuit, which imparts a capacitive-type impedance upon the field. After propagation through the meanderline retarder, the polarization components exhibit a phase shift due to the opposing lumped impedances associated with the orthogonal TE and TM modes [86,92,94–96]. Although the scaling of meanderline elements to the IR introduces additional loss mechanisms that are rarely considered in the RF [104], the fundamental behavior remains unperturbed.

To further clarify the properties of the meanderline FSS in terms of the equivalent circuit model, we can establish a relationship between circuit transmission line and optical multilayer theories. Since the meanderline element thickness is much smaller than the wavelength, it can be modeled as an infinitesimally thin sheet that has equivalent surface impedance, which can therefore be combined with the surrounding media as an effective surface-impedance discontinuity. From optical multilayer theory [105,106], we know that the reflection from a surface interface can be written in terms of the surrounding material impedance. Therefore,

transmission through a multilayered meanderline structure can be modeled as a thin-film optical coating with the appropriate equivalent surface impedance at the meanderline surface discontinuity. Thus, what follows is a hybridization of both circuit transmission line [70–73, 86,92,94–96,107] and optical multilayer theory [105,106] for describing the transmission of IR radiation through multilayered meanderline wave retarders. This description is used to formulate our multilayer designs in obtaining optimum transmission throughput.

Consider a generic multilayer structure comprised of multiple meanderline layers that are separated by interstitial layers of dielectric media. Assume that the first meanderline layer is facing towards free space, and that each corresponding dielectric layer that proceeds a given meanderline layer can be combined into a sort of replicated unit cell. Referring to Figure 12, each effective unit cell can be described in terms of the surrounding material impedance, the propagation through the dielectric medium, and the equivalent surface impedance discontinuity that represents the FSS layer. Mathematically, this can be written as

$$Y_k = Y_0 \cdot n_k = 1/Z_k \ , \tag{19}$$

$$\beta_k = 2\pi n_k / \lambda_0 \ , \tag{20}$$

where Y_k is the material admittance for the dielectric layer of the k^{th} unit cell, β_k is the associated propagation constant, n_k is the complex index of refraction, Y_0 is the characteristic admittance of free space (1/377 Siemens), and λ_0 is the free space wavelength. The equivalent surface admittance of the meanderline layer is given by Y_{mk}, and t_k is the thickness of the dielectric layer. At this point, it should be noted that the equivalent impedance of the materials and surface layers

can be written in terms of admittance values. This will be done throughout the rest of the dissertation.

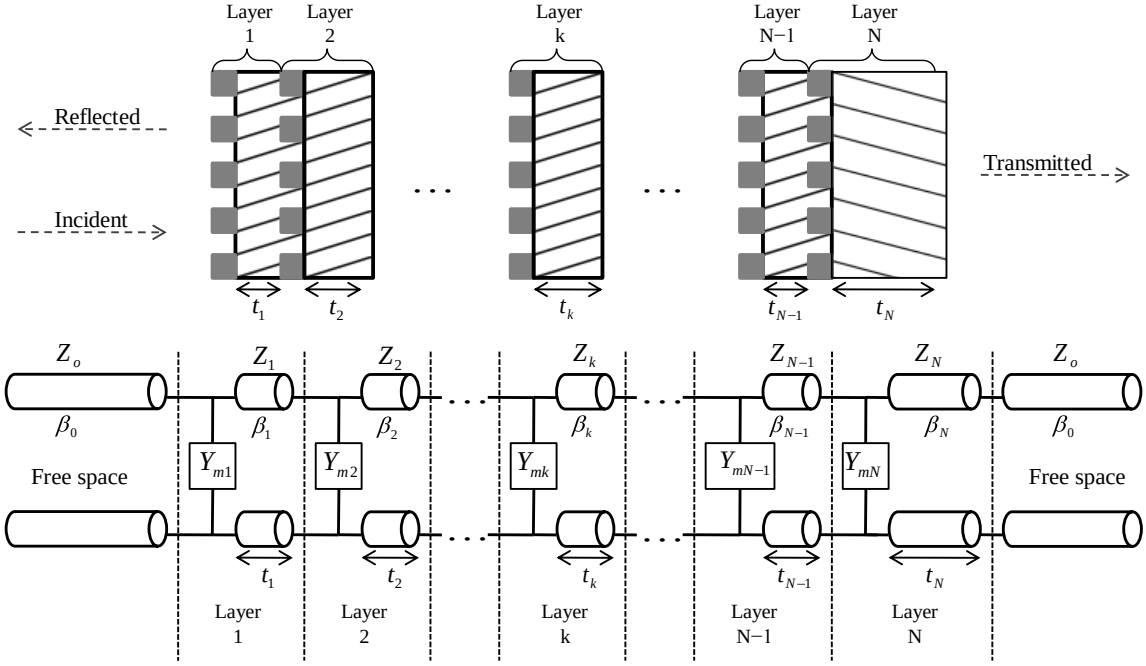

Figure 12: Cross-section of a multilayer meanderline polarizer with corresponding circuit model. Note that the k^{th} unit cell (meanderline surface with dielectric layer) is the repeating element in the multilayer stack.

To determine the transmission coefficient from a multilayer structure, each individual meanderline-dielectric layer combination can be written in terms of a wave transmission matrix [107] that describes the surface admittance discontinuity at the meanderline layer and the propagation through the dielectric layer. For the k^{th} unit cell of the multilayered structure,

$$T_k = T_B \cdot T_A, \tag{21}$$

$$T_A = \frac{1}{2} \cdot \begin{bmatrix} \left(1+\frac{Y_{k-1}}{Y_k}\right) - \frac{Y_{mk}}{Y_k} & \left(1-\frac{Y_{k-1}}{Y_k}\right) - \frac{Y_{mk}}{Y_k} \\ \left(1-\frac{Y_{k-1}}{Y_k}\right) + \frac{Y_{mk}}{Y_k} & \left(1+\frac{Y_{k-1}}{Y_k}\right) + \frac{Y_{mk}}{Y_k} \end{bmatrix}, \tag{22}$$

$$T_B = \begin{bmatrix} \exp(i\beta_k t_k) & 0 \\ 0 & \exp(-i\beta_k t_k) \end{bmatrix}. \tag{23}$$

In the preceding equations, Y_{k-1} is the material admittance of the dielectric layer for the $(k\text{-}1)^{th}$ unit cell. The individual matrices T_A and T_B represent the surface admittance discontinuity and the propagation through the dielectric layer, respectively. For a multilayer system with N respective unit cells, the total system matrix would be

$$\overline{T} = \begin{bmatrix} \overline{T}_{11} & \overline{T}_{12} \\ \overline{T}_{21} & \overline{T}_{22} \end{bmatrix} = T_N \cdot T_{N-1} \cdot \ldots \cdot T_k \cdot \cdots \cdot T_2 \cdot T_1 . \tag{24}$$

As an added correction, if the last unit cell in the system has a finite dielectric thickness whose back side faces towards free space, we can say that

$$T_N = T_C \cdot T_B \cdot T_A , \tag{25}$$

where T_A and T_B are the same as Equations 22 and 23 for $k = N$, and T_C is given by

$$T_C = \frac{1}{2} \cdot \begin{bmatrix} 1 + \frac{Y_N}{Y_0} & 1 - \frac{Y_N}{Y_0} \\ 1 - \frac{Y_N}{Y_0} & 1 + \frac{Y_N}{Y_0} \end{bmatrix}. \tag{26}$$

The individual matrix elements in Equation 24 can then be utilized to obtain the complex amplitude reflection and transmission coefficients

$$\Gamma = -\overline{T}_{12} / \overline{T}_{11} , \tag{27}$$

$$\tau = \det(\overline{T}) / \overline{T}_{11} . \tag{28}$$

In Equation 28, $\det(\overline{T})$ is the determinant of the system matrix, and is given by the expression Y_0/Y_f, where Y_f represents the admittance of the final optical layer. In most cases, Y_f is free space,

so the value of $\det(\overline{T})$ results in unity. Likewise, the power reflection and transmission coefficients are the following

$$R = |\Gamma|^2 , \tag{29}$$

$$T = |\tau|^2 \cdot \mathrm{Re}(n_f) , \tag{30}$$

where n_f is the complex index of refraction of the last medium through which the optical wave propagates. Since the multilayered structure is surrounded by free space, n_f is just the refractive index of air.

It should be mentioned at this point that the wave transmittance matrix method (TMM) works perfectly assuming the incident radiation retains a high degree of coherence upon propagation through the layers. For typical thermal IR sources, this is somewhat true, since the longitudinal coherence is on the order of the wavelength [3,7], and most of the dielectric layers are thin enough to be well below the effective medium wavelength λ_0/n. However, the substrate thickness is comprised of hundreds of wavelengths, such that the phasing term of the TMM approach, given by Equation 23, washes out. Therefore, if the equivalent matrix of the substrate is given by T_N in Equation 25, then one should only consider the Fresnel scattering coefficients at the material boundaries, thereby ignoring or omitting T_B from the expression.

Considering that the TMM approach has been prescribed for analyzing multilayer meanderline polarizers, it would be worthwhile to derive, in terms of output TMM parameters, the common polarimetric observables that are associated with wave retarder characteristics. However, it should be noted that a single TMM calculation can only handle one polarization state and frequency at a time, which means that the meanderline admittances Y_{mk} have to be

extracted separately for each orthogonal polarization at a single frequency. The procedure for determining Y_{mk} will be discussed momentarily. For now, we write the differential phase shift imposed by the meanderline wave retarder as

$$\delta = \pm\left|\arctan(\mathrm{Im}(\tau_{TE})/\mathrm{Re}(\tau_{TE})) - \arctan(\mathrm{Im}(\tau_{TM})/\mathrm{Re}(\tau_{TM}))\right|, \tag{31}$$

where the $\pm$ sign indicates the choice of axes with respect to the meanderline element. Therefore, it can be seen that the resultant TMM transmission coefficients from Equation 28 directly relate to the phase shift acquired upon propagation through the multilayer meanderline structure. Additionally, one can also extract a quantity known as the axial ratio of the polarization ellipse [8,9,86]

$$AR = 1/\tan[0.5 \cdot \arcsin\{\sin\delta \cdot \sin 2\psi\}]. \tag{32}$$

The auxiliary angle in Equation 32 is the angular ratio of the transmitted orthogonal polarization states [8]

$$\psi = \arctan(\left|\tau_{TE}/\tau_{TM}\right|). \tag{33}$$

Thus, since the axial ratio and differential phase shift are all that's needed for complete characterization of the polarization ellipse [8,9], the TMM approach can be utilized to predict the polarimetric performance of a multilayered meanderline retarder by simply evaluating the respective complex scattering coefficients given in Equations 27 and 28. When used in conjunction with numerical simulations, TMM can assist in optimizing the multilayered structure for maximum transmittance throughput, which can be written as a geometrical average between the two polarization states

$$T_{total} = 0.5 \cdot (T_{TE} + T_{TM}). \tag{34}$$

This design facet is absolutely essential, especially since competing technologies have already demonstrated high transmission throughput in the IR spectrum [27–34].

Finally, we turn our attention to the retrieval of the meanderline layer admittance Y_{mk}, which lies at the crux of the TMM method. The fact of the matter is that all variables in the cascaded matrix equation need to be accounted for, so if there are N unknown admittances, then either N equations are required, or an iterative approach needs to be applied. Having only a singular system matrix given by Equation 24, we shall use the latter method for procuring the meanderline admittances by invoking a layer-by-layer approach. This involves the assistance of a numerical full wave solver, notably ANSYS HFSS, to perform the extraction process that would otherwise have to be attempted by similar methods, such as the periodic moment method, integral equation methods, and mode matching techniques [90,91,94–97,103] to name a few. The details concerning numerical modeling with ANSYS HFSS shall be relegated to another section in the present chapter.

Continuing with the admittance parameter retrieval, we select the meanderline layer of interest, say layer j, in the multilayer structure. The other meanderline layers in the stack are temporarily removed from the model so that the j^{th} layer is the only one remaining. With reference to Equations 22 and 23, Y_{mk} is non-zero when $k = j$. Otherwise, $Y_{mk} = 0$ for all $k \neq j$. The equivalent model in the numerical full wave solver reflects this condition. Then, the remaining structure is solved within the HFSS program and the complex amplitude reflection coefficient in Equation 27 is acquired for both TE and TM polarizations. Since there is only one meanderline admittance to solve for with regard to each polarization state, Equation 27 can then be used to determine Y_{mk}. For instance, a single-layer meanderline polarizer ($N = 1$) will have the following

complex amplitude reflection coefficient, which is determined from the system matrix parameters of Equation 24 and solved directly within HFSS

$$\Gamma = \frac{-\left(e^{-i\beta_1 t_1}\cdot\left(\frac{Y_1}{Y_0}-1\right)\cdot\left(\frac{Y_0}{Y_1}+\frac{Y_{m1}}{Y_1}+1\right)+e^{i\beta_1 t_1}\cdot\left(\frac{Y_1}{Y_0}+1\right)\cdot\left(\frac{Y_0}{Y_1}+\frac{Y_{m1}}{Y_1}-1\right)\right)}{e^{-i\beta_1 t_1}\cdot\left(\frac{Y_1}{Y_0}-1\right)\cdot\left(-\frac{Y_0}{Y_1}+\frac{Y_{m1}}{Y_1}+1\right)-e^{i\beta_1 t_1}\cdot\left(\frac{Y_1}{Y_0}+1\right)\cdot\left(\frac{Y_0}{Y_1}-\frac{Y_{m1}}{Y_1}+1\right)}. \quad (35)$$

Solving for the meanderline admittance Y_{m1} will then yield the following

$$Y_{m1} = \frac{2Y_0Y_1\Gamma\cos(\beta_1 t_1) - i\cdot\sin(\beta_1 t_1)\cdot((\Gamma+1)\cdot Y_1^2 + (\Gamma-1)\cdot Y_0^2)}{(\Gamma+1)\cdot(Y_1\cos(\beta_1 t_1) + i\cdot Y_0\sin(\beta_1 t_1))}. \quad (36)$$

The solutions for the admittances of a 2-layer or 3-layer meanderline polarizer structure will be fairly similar to Equation 36, but with more propagation constants and reflection terms to account for the inclusion of additional layers. Note that the meanderline admittance in Equation 36 depends upon which of the two reflection coefficients are inserted into the formula, since the geometry of the structure indicates anisotropic behavior for the respective incident TE and TM polarizations [86,92,94–100]. For instance, if the complex TE reflection coefficient is used, then the resulting admittance will correspond to the TE mode of the meanderline polarizer layer. Likewise, the admittance for the TM mode will be obtained by using the complex TM amplitude reflection coefficient.

This concludes the formulation of the TMM algorithm, which solves each layer one at a time and combines the solved admittances into the cascaded system matrix given by Equation 24. This segmented approach is consistent with other methods that solve for the meanderline admittances separately on a layer-by-layer basis [86,95–97], such that each meanderline layer is

effectively acting on its own without any coupling between adjacent layers. Therefore, comparisons between the TMM approach and solving the entire structure within HFSS are quite useful, especially for determining any differences in the numerical results that are due to mutual admittance coupling and other full wave effects. Furthermore, the TMM will be used in conjunction with HFSS to optimize the interlayer dielectric thickness that results in an admittance-matched multilayer meanderline structure, which indicates that a maximum transmission throughput and corresponding reflection minimum has been obtained. Results from both of these numerical techniques will be compared to the experimental transmission data from an assortment of multilayer meanderline polarizers.

It should be mentioned that although the TMM approach was performed for a single wavelength at normal incidence, it can be done over multiple frequencies at various non-zero angles of incidence with only a slight modification to the formulas in the current section [95].

2.1.2 Equivalent Circuit Model for Reflective Meanderline Retarders

The equivalent circuit model for reflective meanderline FSS retarders is drastically similar to the one that was just detailed in the previous section for transmissive components. In fact, all of the aforementioned methodologies and respective equations of Section 2.1.1 can be used for reflective meanderline systems, except that a few differences must be taken into account when modeling the corresponding structures with the TMM approach. First off, instead of a transparent substrate, the meanderline layer sits on a planar dielectric layer above a reflective metallic groundplane, as demonstrated in Figure 13.

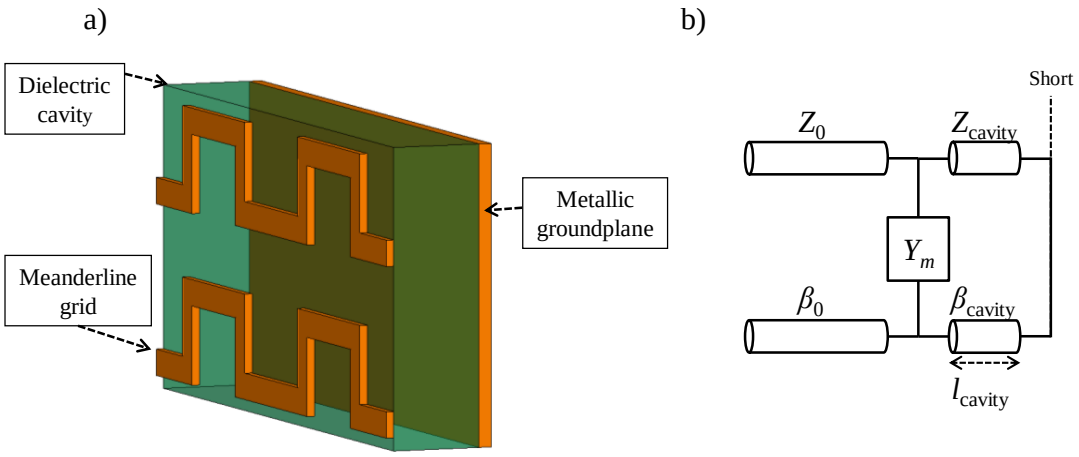

Figure 13: Diagram of a) meanderline geometry patterned on a dielectric cavity above groundplane, and b) equivalent circuit model of multilayer dielectric system with meanderline discontinuity Y_m as the shunt admittance.

The meanderline structure of Figure 13 is fabricated on a dielectric layer, so the meanderline-dielectric surface collectively represents a single planar discontinuity that can be modeled as a single shunt admittance element [86,92,95], which is subsequently added to the equivalent circuit of the planar dielectric and groundplane. The dielectric layer is represented by finite-length transmission lines with wave impedances characteristic of the associated optical materials [86,95,107]. The short-circuit termination represents the reflective groundplane of the meanderline wave retarder structure, consistent with previous reflective designs [108–110].

The interaction between incident IR radiation and the meanderline can be visualized in the same way as before, with the incident field decomposed into TE and TM modes that correspond to equivalent capacitive and inductive impedances, respectively. However, as Figure 14 demonstrates, the transmission lines end in a short-circuit termination, which allows for multiple reflections inside the dielectric cavity. Therefore, the differential phase shift of the reflective meanderline FSS would accumulate over multiple successive transmissions through

the meanderline structure, both forwards and backwards, since the fields reflect off of the metallic groundplane and induce resonant-cavity modes inside the dielectric standoff layer [95,107].

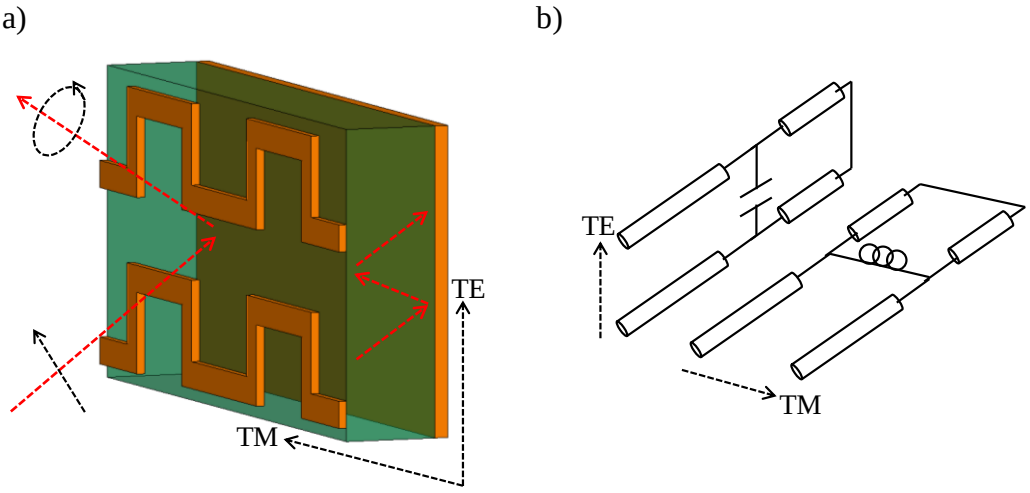

Figure 14: Depiction of a) meanderline geometry with incident linearly polarized wave, reflected CP field, and multiple reflections inside dielectric cavity. Part b) represents the equivalent circuit elements of the meanderline grid.

Regarding the equations of the TMM approach, there are only a few changes that need to be implemented in order to accurately model reflective meanderline FSS grids. First, it should be noted that the amplitude transmission coefficient of Equation 28 will yield an extremely small value due to the magnitude of the metallic groundplane's refractive index and extinction constant, so this parameter can be ignored. Secondly, the matrix that represents the planar interface between the dielectric and the groundplane should be the last one accounted for, such that the total system matrix of a single meanderline layer with a dielectric cavity above groundplane is set up exactly like Equation 25. In this instance, the admittance Y_0 should be replaced with Y_{GND}, the equivalent optical admittance of the metal that constitutes the

groundplane. The rest of the formulas, specifically Equations 31 through 34, can therefore substitute in for the appropriate reflection quantities, such that $\tau \rightarrow \Gamma$ and $T \rightarrow R$. Nothing else requires any further alterations, and the TMM method and admittance extraction procedure should work exactly as prescribed.

2.2 Electromagnetic Modeling and Design of Semi-Infinite Planar Periodic Structures Using the Finite Element Method with Floquet Ports

Periodic and multilayered structures have been frequently scrutinized for implementation in computational electromagnetics [111–114]. The actual problem itself represents an interesting dilemma that can be tackled in various ways, such as the periodic method of moments (PMM), finite-difference time-domain (FDTD) method, finite element method (FEM), spectral domain techniques, and so on [111]. In all cases, the fundamental goal is to replicate the results of scattering experiments by constructing a model that is as physically accurate as possible. Thus, we shall discuss in this section our use of ANSYS High-Frequency Structure Simulator (HFSS) software package, which uses the FEM to simulate the electromagnetic response from a variety of structures and systems [112–114].

2.2.1 Basic Principles of the Finite Element Method

Maxwell's equations for electromagnetic fields describe the field and current distributions of a given system as continuous variables, whether or not the equations themselves are written in differential or integral forms. Since modern computers do not have infinite storage capacities, electromagnetic computations must discretize the system and the equations under

consideration. This means that Maxwell's equations must be written in finite difference notation, or as a finite sum if dealing with the integral formalism [111]. The discretization of Maxwell's equations is actually a discretization of the three-dimensional solution space, so the structure under analysis can be segmented into finite elements that represent a volumetric mesh of the complete material system. For example, the mesh of a meanderline unit cell from HFSS is shown in Figure 15.

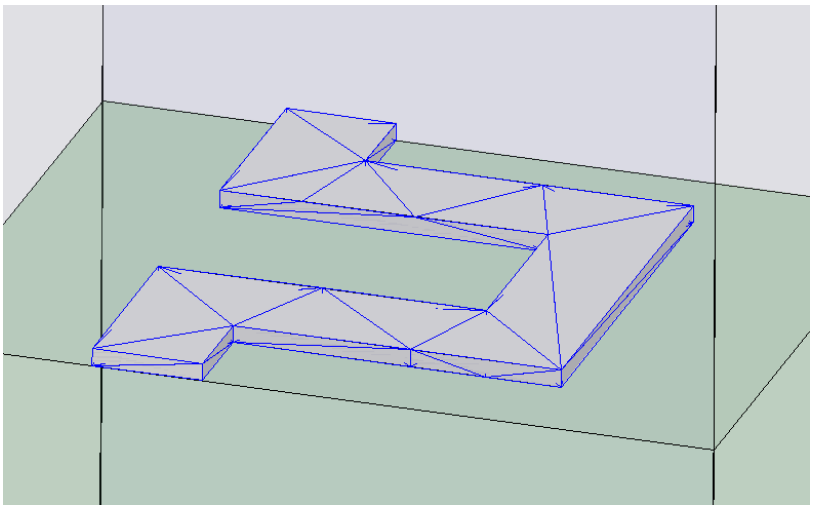

Figure 15: Three-dimensional tetrahedral mesh of a unit meanderline element.

In order to achieve suitable accuracy, the volume mesh elements must be small enough at the given simulation wavelength so that a near-homogeneous and continuous field solution is obtained. With HFSS, the accuracy can be adjusted to adhere to certain convergence criteria of the output scattering parameters. However, this can only be done at a single design frequency, since a) the volumetric mesh can only be made once for any given model, unless excess memory and hard disk space is available for each requested frequency in the simulation, and b) the mesh is frequency-dependent, since the discretized elements depend upon the design wavelength and

the material properties at that frequency. Thus, when sweeping over a given frequency spectrum, the highest frequency is usually selected as the corresponding mesh frequency, which results in the smallest volume mesh elements and the best accuracy available. This avoids many potential pitfalls, such as meshing at the wrong frequency or not accounting for material dispersion when creating the mesh.

The three-dimensional mesh in HFSS is formed by an adaptive process that segments each structure into discrete tetrahedral elements, as seen in Figure 15. After the mesh is constructed, it is only a matter of solving for the fields at each vertex or node of the tetrahedral element. The standard procedure that the FEM implements in its solution process is anything but straight-forward, since a complicated interpolation scheme is used to average the fields between nodal segments. Nonetheless, we can generalize the methodology by assuming that any field solution can be acquired by solving for the characteristic operator equation

$$L\Phi = g\,, \tag{37}$$

where Φ represents the desired field quantity, L is the spatial operator, and g is the source function [111]. In Equation 37, any field expression can be inserted for Φ depending upon what needs to be solved for and what methods are used to achieve the end result. For instance, Φ could be the scalar potential that is solved using Laplace's equation, where L would be the Laplacian operator. On the other hand, Φ could be interpreted as a direct field quantity, such as E_x, that would be obtained by evaluating Helmholtz's wave equation, where the spatial field operator would be written as

$$L = \nabla^2 + k^2. \tag{38}$$

In either case, the primary objective of the FEM is to solve the respective operator equation by minimizing the residue functional

$$I(\Phi) = \langle L, \Phi \rangle - 2\langle \Phi, g \rangle, \tag{39}$$

which, in the case of the Helmholtz wave equation, can be written as

$$I(\Phi) = \frac{1}{2} \iiint \{ |\nabla \Phi|^2 - k^2 \Phi^2 + 2\Phi g \} dV, \tag{40}$$

where the triple integral is taken over the volume of the discretized element [111]. From here onwards, the procedure would entail the discretization of the volume integral with the differential operator ∇, which allows for Equation 40 to be put into matrix notation. Therefore, the field quantity Φ would be solved as a three-dimensional matrix array subject to the appropriate boundary conditions of the system. Such boundary conditions are given by Maxwell's equations, and by the periodicity of the meanderline FSS grid array. The periodical nature of the meanderline elements allows us to simplify the analysis of the structure by reducing the computational volume to the smallest rectangular unit cell. This unit cell is depicted with corresponding dimensional parameters in Figure 16.

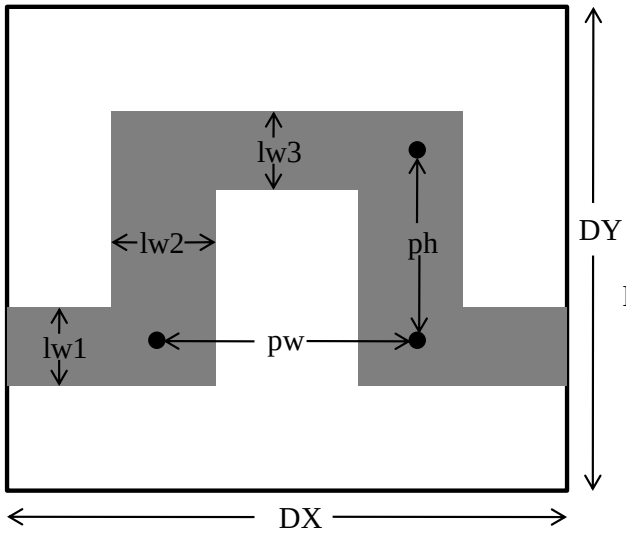

Figure 16: Unit cell and corresponding dimensional parameters of a meanderline FSS.

Although HFSS can effectively model the scattering of waves from a semi-infinite FSS array using a wide variety of technical approaches, the most accurate method is to utilize the periodic boundary conditions in concurrence with Floquet port excitations on a single rectangular unit cell. These two features go hand-in-hand for emulating the propagation and scattering of waves from a periodic structure.

2.2.2 Periodic Boundary Conditions, Mutual Impedance Coupling, and Grating Behavior of Semi-Infinite Planar Frequency Selective Surfaces

Periodic boundary conditions enforce a certain constraint on the phase of the electromagnetic fields that are solved within the finite unit cell volume. Since the FSS layer is periodic, we would expect the fields to be similar in amplitude across the surface, apart from a phase difference that is given by the cell-to-cell spacing, which is determined by the primitive lattice vectors associated with *DX* and *DY* on Figure 16

$$\vec{d} = \overrightarrow{DX} \cdot n + \overrightarrow{DY} \cdot m, \tag{41}$$

where *n* and *m* are real integers. Thus, we can apply the Floquet-Bloch theorem [refs] to the optical field of Equation 1 that is evaluated at a certain position on the two-dimensional unit cell

$$\vec{E}(\vec{r} + \vec{d}) = \vec{E}(\vec{r}) \cdot \exp(i\vec{k} \cdot \vec{d}). \tag{42}$$

Since the displacement vector $\vec{d}$ is in the plane of the cell, then the phase term can equate to unity when the wavevector $\vec{k}$ is normal to the surface. Therefore, the periodic condition depends upon the incident and scattered field orientations, which are specified by the Floquet modes that interact with the FSS grid array.

The problem of electromagnetic wave scattering from a planar two-dimensional grid array is highly reminiscent of similar diffraction phenomena from gratings and other periodical structures, such that the behavior is directionally dependent upon the electromagnetic field phasing between individual unit cells. Thus, the array periodicity is the main contributor of such diffraction effects, since the electromagnetic response achieves a generalized uniformity over the entire FSS array with regard to the spatially-varying electric field amplitude, as indicated by Equation 42. This uniform response is due to a) the uniformity of illumination, such that each unit cell of the array is excited by the same incoming beam of radiation at an arbitrary angle of incidence, and b) electromagnetic coupling between array elements, which can be described by mutual impedance coupling between the induced surface currents of each unit cell in the semi-infinite array. Figure 17 illustrates this coupling effect between two neighboring unit cell elements of a semi-infinite FSS grid.

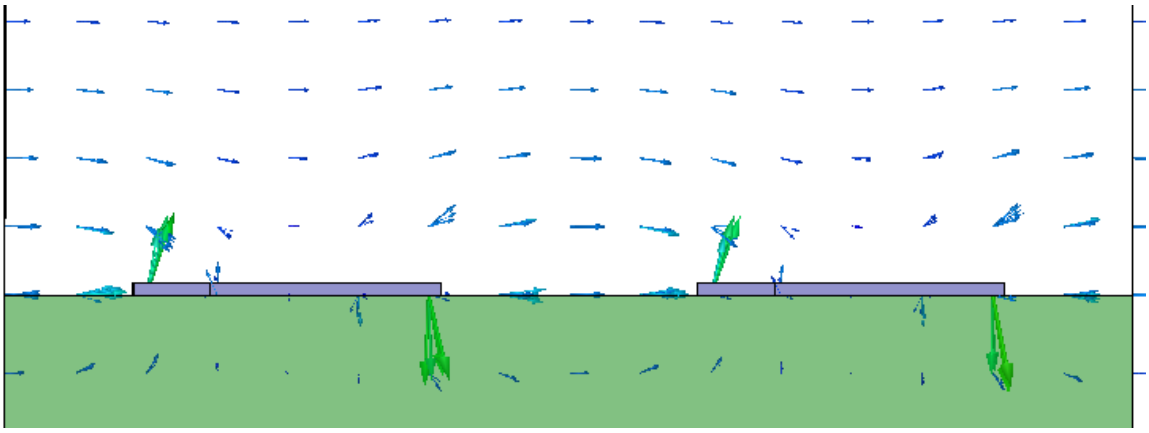

Figure 17: Electric field coupling between two adjacent meanderline elements modeled by HFSS

The mutual impedance approach can be implemented in MoM simulations to extract the values of the surface current density elements on a periodic array of scatterers [90–92]. Each element experiences mutual impedance effects from the other corresponding elements in the array, along with a self-impedance and load impedance that, with the induced current, can be equated to the total accumulated voltage between discrete positions along the length of the scattering elements. In matrix notation, this can be written as an extension of Ohm's circuit law

$$\begin{bmatrix} V_1 \\ \vdots \\ V_k \\ \vdots \\ V_N \end{bmatrix} = \begin{bmatrix} Z_{1,1}+Z_{L1} & \cdots & Z_{1,k} & \cdots & Z_{1,N} \\ \vdots & \ddots & \vdots & & \vdots \\ Z_{k,1} & \cdots & Z_{k,k}+Z_{Lk} & \cdots & Z_{k,N} \\ \vdots & & \vdots & \ddots & \vdots \\ Z_{N,1} & \cdots & Z_{N,k} & \cdots & Z_{N,N}+Z_{LN} \end{bmatrix} \cdot \begin{bmatrix} I_1 \\ \vdots \\ I_k \\ \vdots \\ I_N \end{bmatrix}, \tag{43}$$

where the subscripts $1 \cdots k \cdots N$ dictate the order of elements in an array that has N total elements (or N total unit cells), Z_{Lk} is the load impedance of the k^{th} element in the array, and $Z_{k,k}$ is the self-impedance of that same element [90]. The mutual impedances $Z_{n,k}$ are governed by the electrical coupling effects between the n^{th} and k^{th} elements, such that the total voltage acquired

over a single element is determined from the sum of all respective mutual impedances and associated currents on each unit cell, along with the self and load impedances of the original scatterer. The coefficient $Z_{n,k}$ can therefore be thought of as a measure of electrical coupling strength between the n^{th} and k^{th} cells. Ultimately, the current and field distributions can be solved for by inverting the impedance matrix, which results in a single column vector of current densities for each k^{th} unit cell. However, the condition defined by the Floquet-Bloch theorem of Equation 42 places a restriction on the electric field of each unit cell, which must maintain periodicity in order to satisfy the equivalent boundary condition. Thus, the solution for the current densities of Equation 43 must also abide by Equation 42, and hence achieve a uniform distribution over the surface of the FSS array with an additional phase factor that implicates dependence upon the directional scattering behavior with regard to the array periodicity. This is equivalent to saying that the amplitude of the current density on each unit cell, given as I_k, is the same across the entire array apart from the periodical phase term, which is dependent upon the unit cell spacing and the direction of the incident and scattered fields. Therefore, the quasi-homogeneous array response and the equivalent diffraction grating behavior are both due to the semi-infinite periodic nature of the FSS grid. The scattering orders, both evanescent and propagating, are determined from the array periodicity and the Floquet modes, which are described in the next section.

2.2.3 Floquet Modes and Polarization-Dependent Scattering Parameters

Floquet modes can be described as an arbitrary field distribution specified by an angular spectrum of plane waves, as in Equation 1. However, the fundamental difference in this case is that a) the Floquet fields obey Equation 42, which ensures periodicity, and b) there are two distinct polarization modes defined at the port terminations that correspond to the primitive lattice vectors of Equation 41. Therefore, the fundamental modes of the excited and scattered fields would be the TE and TM polarizations, which are virtually identical to the capacitive and inductive field modes of the equivalent meanderline FSS circuit. HFSS uses a mathematical construction that defines the Floquet modes for a given scan direction, which is specified by the specular reflection from the surface of the FSS array. The scan direction unit vector is given as

$$\hat{r}_s = (\sin\theta_s \cos\phi_s, \sin\theta_s \sin\phi_s, \cos\theta_s), \tag{44}$$

where θ_s and ϕ_s are the scanning angles defined under the generalized coordinate system. These angles are implemented in the phasing of the electromagnetic waves between periodic boundaries, which makes sense since $\hat{r}_s$ defines the direction of $\vec{k}$ with regard to the periodicity condition of Equation 42. Thus, given lattice vectors $\vec{a}$ and $\vec{b}$, the electric fields of the TE and TM modes can be defined by the following expressions

$$\vec{e}_{m,n}^{TE} = N_{m,n}^{TE} \cdot \Psi_{m,n}^{TE}, \tag{45}$$

$$\vec{e}_{m,n}^{TM} = N_{m,n}^{TM} \cdot \Psi_{m,n}^{TM}, \tag{46}$$

where $N_{m,n}^{TE,TM}$ are the normalization constants, and

$$\Psi_{m,n}^{TE} = \left(\frac{k_y \hat{x} - k_x \hat{y}}{\sqrt{k_x^2 + k_y^2}} \right) \cdot \sqrt{\frac{1}{ab \sin\alpha}} \cdot \exp(-i(k_x x + k_y y)), \tag{47}$$

$$\Psi_{m,n}^{TM} = \left(\frac{k_x \hat{x} + k_y \hat{y}}{\sqrt{k_x^2 + k_y^2}} \right) \cdot \sqrt{\frac{1}{ab \sin\alpha}} \cdot \exp(-i(k_x x + k_y y)). \tag{48}$$

In the above formulas, *a* and *b* are the magnitudes of the primitive lattice vectors, α is the angle that is formed between the lattice vectors, and the wavevector components are given by

$$k_x = \frac{2\pi \cdot m}{a} + \frac{\sqrt{\mu_r \varepsilon_r} \cdot k_0 \cdot \hat{r}_s \cdot \vec{a}}{a}, \tag{49}$$

$$k_y = \left(\frac{1}{\sin\alpha} \right) \cdot \left(\frac{2\pi \cdot n}{b} + \frac{\sqrt{\mu_r \varepsilon_r} \cdot k_0 \cdot \hat{r}_s \cdot \vec{b}}{b} \right) - k_x \cdot \cot\alpha, \tag{50}$$

where *m* and *n* are integers that indicate field scattering due to the grating periodicity of the FSS surface, and $k_0 = 2\pi/\lambda$. It should be noted that the $\exp(i(\omega t - k_z z))$ term is factored out of Equations 47 and 48 for simplicity. Furthermore, because of the rectangular nature of the unit cell, the unit vectors $\hat{x}$ and $\hat{y}$ correspond to the directions given by the primitive lattice vectors $\vec{a}$ and $\vec{b}$, respectively, which makes α equal to 90°. Finally, the wavevector component in the $\hat{z}$ direction is written as

$$k_z = \sqrt{\mu_r \varepsilon_r k_0^2 - (k_x^2 + k_y^2)}. \tag{51}$$

For each of the TE and TM modes in Equations 45 and 46, there is a subset of modes given by the coefficients *m* and *n* that define the direction of the scattered field, which is either specular or diffuse. The specular direction, which is obtained when both *m* and *n* are set to 0, is always

present as a propagating mode, unless planar boundary conditions dictate otherwise [90–92,115]. The other scattering directions, i.e. when m and n are non-zero integers, can be either propagating or evanescent depending on the value of k_z. The evanescent modes occur when the in-plane wavevector is larger than that of free-space, so the $\hat{z}$ component becomes imaginary, which attenuates the field in the direction of propagation. Figure 18 illustrates the regimes of propagating and evanescent fields within the framework of the scattering problem from a two-dimensional grid array.

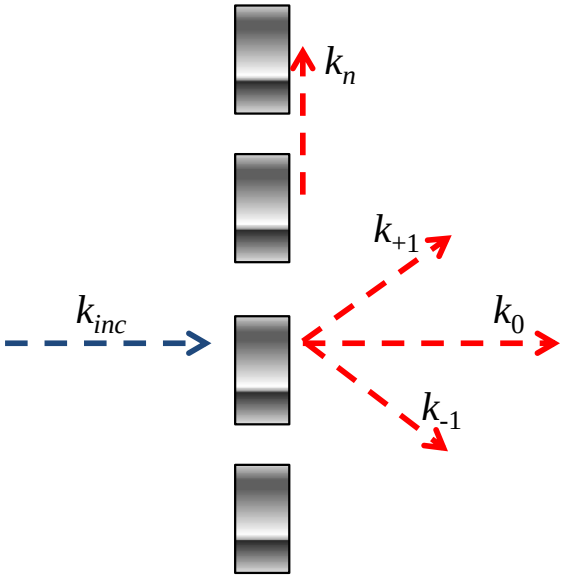

Figure 18: Representation of diffraction by an array of arbitrary scatterers. The subscripts for the scattered wavevector components indicate the respective diffraction order, such as 0^{th} (specular), $+1^{st}$, and so on. The wave component tangential to the interface k_n is a higher-order evanescent mode that travels along the interface of the scattering array.

As far as numerical simulations are concerned, we are only interested in the field modes that are not attenuated and actually contribute to the field distribution in the Fraunhofer zone. Thus, since the magnitudes of the primitive lattice vectors of a meanderline FSS array are, by definition,

subwavelength in dimension, the $\hat{z}$ component of the wavevector would be imaginary for any pair of *m*,*n* that is not equal to 0. Hence, the specular components are the only remaining modes that do not exhibit any discernable attenuation. Although there is the option to include additional modes that exhibit attenuation in HFSS, these are mostly truncated and do not contribute to the polarization signal in the far-field regime [92,115]. Figure 19 shows the unit volume cell in HFSS with the prescribed periodic boundary conditions, which are enforced via 'master' and 'slave' boundaries, and the Floquet port excitations that govern the directionality of the specular reflection from the FSS.

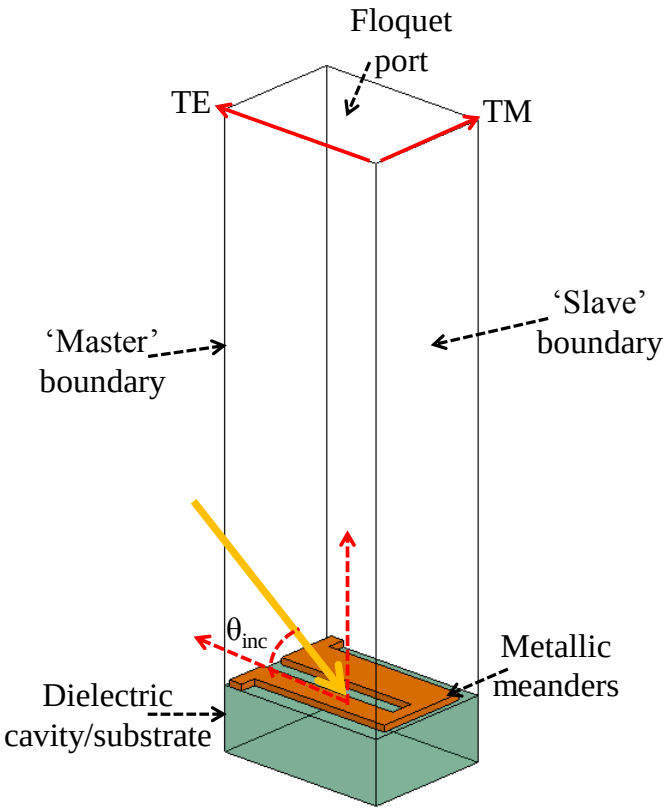

Figure 19: Unit volume cell constructed in HFSS for simulation of a planar periodic meanderline grid array. The angle of incidence θ_{inc} prescribes the phasing between boundaries and scattered orders of the Floquet modes.

Floquet ports can serve as both receivers and emitters; the fundamental Floquet TE and TM modes can be defined at the boundaries of the port termination, which can also read the scattered amplitude and phase information from the Floquet modes that originate from the same or opposite Floquet port. Thus, a list of generated scattering parameters can be acquired from each port and field mode, which correspond to the conventional S-parameters [107] but with additional polarization information. As long as the field modes are kept consistent, the modal scattering parameters can determine any desired spectral behavior, such as average transmission (Equation 34), differential phase shift (Equation 31), or even the Stokes parameters of the scattered field. This is a powerful tool that will be utilized throughout all numerical computations within HFSS. The following figure contains a snapshot of the S-parameter matrix that is the result from a two-port simulation of a meanderline FSS.

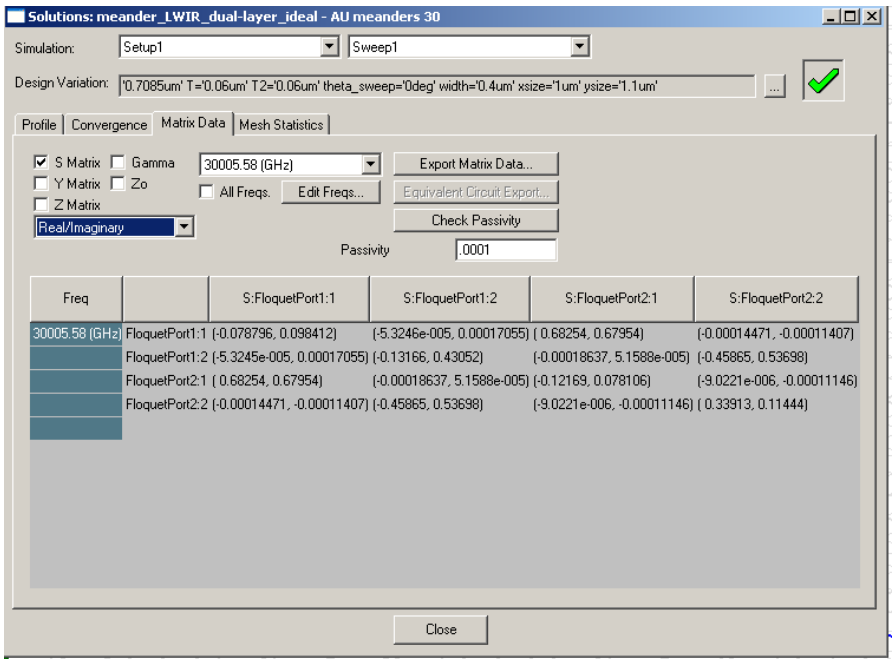

Figure 20: Output S-parameter data from an HFSS simulation of a transmissive meanderline structure.

2.2.4 Material Properties in Electromagnetic Simulations

Numerical models are only as good as the data and information that is inserted into the simulation. Therefore, in order to obtain valid numerical data for a broad range of wavelengths, the appropriate frequency-dependent material constants should be entered so that dispersion is accounted for. In the IR spectrum, we measure the optical properties using a technique called variable-angle spectroscopic ellipsometry (IR-VASE). This is a non-destructive automated broadband measurement that obtains the complex index of refraction for a variety of thin film materials, including metals, dielectrics, and semiconductors to name a few [8,9,116]. In HFSS, the material properties have to be converted into the complex permittivity function, which is given as

$$\varepsilon_r = \varepsilon_r' + i \cdot \varepsilon_r'' = n^2 - k^2 + i \cdot 2nk \,. \tag{52}$$

For dielectrics, the permittivity can be simply defined as the real part ε_r' along with the loss tangent ratio, which indicates the attenuation strength upon propagation through the thin film

$$\tan \partial_{loss} = \frac{\varepsilon_r''}{\varepsilon_r'} = \frac{2nk}{n^2 - k^2} \,. \tag{53}$$

Conductors are normally written in terms of the material's DC conductivity, which is another indication of absorption loss since

$$\varepsilon_r = \varepsilon_r' + i \cdot \varepsilon_r'' = \varepsilon_r' + i \cdot \frac{\sigma_{DC}}{\omega \varepsilon_0} \,, \tag{54}$$

where ω is the angular frequency, and ε_0 is the permittivity of free space [2,3,14]. Thus, we can express the dynamic conductivity in terms of the retrieved optical constants:

$$\sigma_{DC} = 2nk\omega\varepsilon_0 . \tag{55}$$

With the measured material parameters inserted into HFSS, we can tailor the design of the periodic structure so that the desired yet realistic spectral behavior is achieved. Note that the magnetic permeability μ_r is not mentioned here, since most dielectric and metal films are non-magnetic, and thus retain a value of unity for μ_r.

2.2.5 Example of Design Procedure of Multilayer Meanderline QWPs Using the Finite Element Method in ANSYS HFSS

The remaining details of the current section shall attempt to describe the process of designing and optimizing a transmissive multilayer meanderline wave retarder so that achromatic QWP behavior and a high degree of throughput are obtained. Initially, we constrain the unit cell dimensions in Figure 16 to subwavelength values, so that grating lobes do not appear for oblique incident angles up to the specified F/# of the impinging focused beam. Therefore, the largest cellular dimensions given by *DX* and *DY* should result in an undefined value when plugged into the grating equation

$$m\lambda_{eff} / a = \sin\theta_{in} \pm \sin\theta_m , \tag{56}$$

where *a* is the largest dimension of the unit cell [7]. Additionally, the cell-to-cell spacing must also avoid the occurrence of grating-coupled plasmon modes, which assist in the attenuation of the optical signal at pre-defined excitation wavelengths

$$\lambda = \frac{a}{m}\left(\sqrt{\frac{\varepsilon_m \varepsilon_d}{\varepsilon_m + \varepsilon_d}} - \sqrt{\varepsilon_d}\,\sin\theta_{in} \right), \tag{57}$$

where ε_m and ε_d are electrical permittivities of the metal FSS and dielectric surroundings, and m is the grating order of the periodic FSS array [26,117]. As long as the largest periodicity dimension corresponding to a is kept small enough, the plasmonic excitations should be relegated to wavelengths far below the domain of interest. Given these constraints, the dimensional parameters of the meanderline structure can then be modified so that the transmitted scattering coefficients of HFSS result in a $\pi/2$ differential phase shift as required by Equation 31. The linewidths, metal thickness, and array spacings can be iteratively adjusted for each meanderline layer until this criterion is satisfied. For the multilayer structures, the thickness of each dielectric standoff layer is initially defined as $\lambda_0/4n$, where n is the refractive index of the interstitial polymer layer. After refinement of the array dimensions, the effective meanderline admittances are extracted using the retrieval process outlined in the previous section. The complex amplitude reflection coefficients for both TE and TM polarizations are then calculated with Equation 27 over a wide range of thicknesses for the dielectric standoff layers. This procedure has to be performed once for each standoff layer in the model. Ultimately, the desired thicknesses of the standoff layers can be found when the absolute value of the complex reflection coefficient reaches an average minimum between the TE and TM polarizations. This can be seen in Figure 21, which displays the optimization of the mean reflection coefficient by varying the thickness of the dielectric cavity between two meanderline layers.

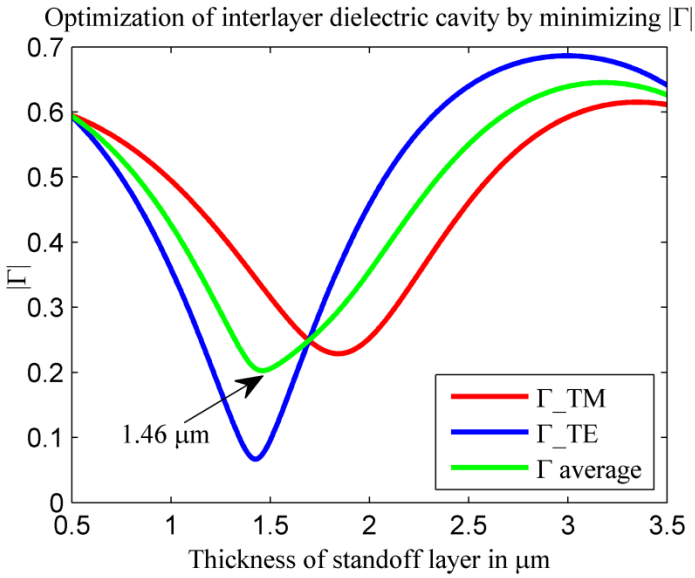

Figure 21: Optimization of a 2-layer meanderline structure by sweeping the interlayer dielectric thickness, which results in an averaged minimum for the reflection coefficient computed by the TMM approach.

The optimum thicknesses can then be inserted into the full-wave solver, which requires a slight adjustment to the meanderline array dimensions so that the optimal phase shift and power transmission response is acquired. Thus, the hybrid approach of using TMM to assist in calculations with ANSYS HFSS is a unique tool that is able to produce an admittance-matched multilayer meanderline FSS that replicates achromatic QWP behavior and retains a high degree of power transmittance throughput.

2.3 Fabrication, Testing, and Characterization of Phase Shifting Meanderline Arrays

Even though computational electromagnetics has progressed to the point of providing unparalleled accuracy, fabrication and testing are still required for experimental verification of the simulated response. Furthermore, one must account for realistic manufacturing effects in the

design of multilayer planar periodic FSSs, which makes fabrication and characterization indispensible assets for engineering and device optimization of such structures. The current section will discuss the details relating to testing and fabrication of multilayer planar periodic meanderline grid arrays for the thermal IR regime.

2.3.1 Electron-Beam Lithography Process and Materials

The manufacture of subwavelength materials for IR and visible applications has been enabled by the ability to pattern features and structures on a submicron scale. In the realm of micro and nanofabrication, there are several methods and techniques that can be utilized for the production of subwavelength features, such as optical lithography, wafer stepping, electron-beam (e-beam) lithography, nano-imprint lithography, focused ion beam (FIB) milling, and holographic laser exposure, to name a few [26,47,118]. Multilayer planar periodic structures can be fabricated by any of the aforementioned processes due to the simple planar construction of the FSS array. Ultimately, e-beam lithography was implemented as the method of choice due to the flexibility of being able to fabricate any prototype two-dimensional planar array design over the entire surface area of a substrate.

This section shall be dedicated to exploring the fundamentals of e-beam lithography process and materials that are used in the fabrication of meanderline retarders. Although each step will be explained in detail, an actual list of process notes for the respective materials can be found in the Appendix section of this dissertation. The unique nature of a few particular materials warrants the inclusion of an Appendix that is strictly devoted to listing the exact

fabrication steps that were employed, especially if such materials are to be used again in future multilayered planar periodic devices.

E-beam lithography consists of exposing an electron-sensitive resist to a focused beam of electrons that, when developed, forms a subwavelength pattern comprised of nanoscale features. The resist that is exposed can either be positive or negative-tone, depending upon the features and their relative size that is required by the original design of the planar FSS structure. Similar to positive and negative photographic exposure, a positive-tone resist forms trenches after development, whereas a negative resist cross-links polymer chains so that a free-standing dielectric is left behind. This difference between resist tonalities is depicted in Figure 22.

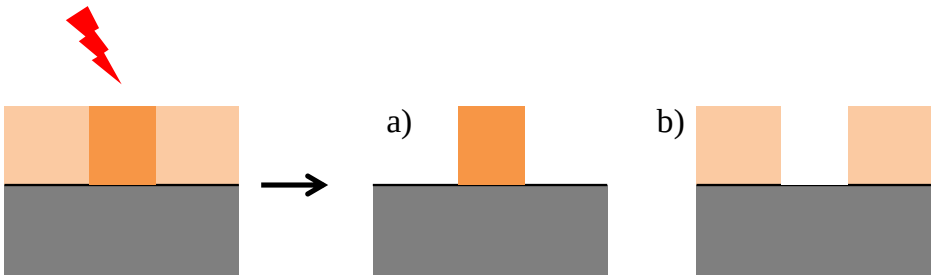

Figure 22: Electron beam exposure and resulting development of a) negative-tone resist, and b) positive-tone resist.

Although negative-tone resist is useful in certain circumstances that require free-standing dielectrics or large areas of unexposed resist, which can be metalized later on, positive-tone resist is more versatile in forming extremely narrow trenches that can be metalized into the thinnest possible linewidths, which is essential for specific FSS array designs and planar IR antennas [118–120]. Therefore, the rest of the fabrication processes described in this section and in the Appendix assumes the use of ZEP 520-A7 thinned positive-tone e-beam resist, which can be

exposed down to a lower resolution limit of 20 nm by the Leica EBPG 5000+ system [118]. A picture of this e-beam lithography system can be found in the following figure.

Figure 23: Leica EBPG 5000+ system at CREOL.

The generalized fabrication routine of a given multilayer planar periodic FSS structure can be summarized in a series of steps that encompasses the entire process from inception to finalized device. As depicted in Figure 24, this usually starts with the direct patterning of subwavelength structures on the material substrate of choice, which is selected for its optical properties and its compatibility with device fabrication procedures. After a thorough cleaning of the substrate, either by spin-cleaning with dispensed solvents or by plasma etch descum, the positive-tone ZEP e-beam resist is spun onto the substrate wafer so that a uniform coating is obtained. The resist is then baked at a high enough temperature for a prolonged period so that all remaining solvents are evaporated from the dielectric. This prevents potential outgassing of

harmful solvents and air-borne moisture that would otherwise contaminate the high-vacuum systems of the Leica e-beam tool. The wafer coated with ZEP is then exposed by the e-beam system with the correct electron energy dosage and beam current that is necessary for exposure of appropriately-sized features. After development in a suitable chemical solution, which either consists of ZEP developer or high-resolution Amyl Acetate, the developed resist is subjected to barrel etching, which removes the remaining particulates that may not have exposed sufficiently to be completely removed by the developer. The submicron pattern is then metalized by either e-beam or thermal evaporation of the required metals, which are directly deposited into the trenches of the developed resist. Finally, the undeveloped resist, along with the excess metal, is lifted off from the substrate under sonic agitation while immersed in a solution of N-Dimethylacetamide, which is an aggressive solvent that specifically targets undeveloped ZEP resist for complete dissolution. At this point, the first layer of a planar FSS device would be completed, although a multilayer structure would require additional steps to complete fabrication on the dielectric layers stratified above the substrate. The initial dielectric layer, deposited either by spin-coating or thermal evaporation methods, usually requires the application of a precursor adhesion layer, such that the dielectric does not peel off from the substrate under subsequent processing. From here onwards, the fabrication routine becomes iterative, as the steps relating to e-beam lithographic exposure, development, metallization, and lift-off follow exactly as before. Additional dielectric films may be deposited and fabricated upon once processing is completed on the initial layer(s).

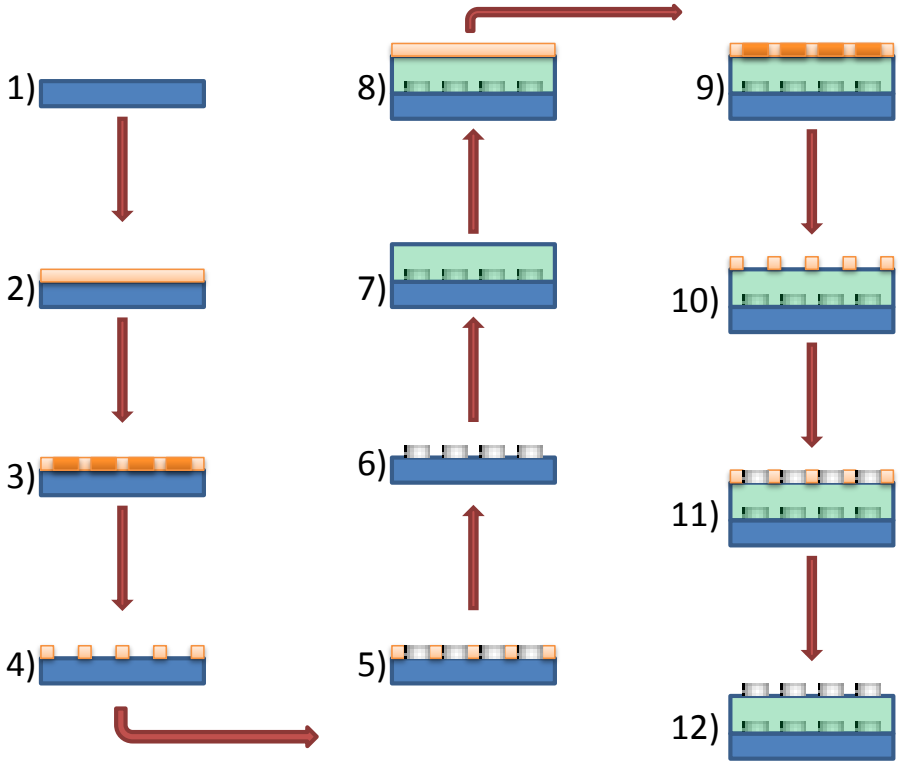

Figure 24: Process steps for fabrication of a 2-layer structure. Steps 1) through 6) detail the e-beam exposure, development, metallization, and liftoff of positive-tone ZEP resist. In step 7), a dielectric cavity with adhesion layer is deposited. Steps 2) though 6) are repeated for the 2nd layer. If more layers are required, repeat steps 7) through 12) iteratively.

Although the above process is sufficient for most materials, some alterations need to be introduced for particular substrates that do not naturally allow for high-resolution e-beam lithography. Such substrates would be classified under dielectric insulators, which build up excess charge when bombarded with a steady beam of impinging electrons [14,118]. The excess charging can over-expose resist, which leads to the development of features that are either over-enlarged or completely washed out. To counter this, the e-beam resist can be coated with a thin conducting layer of metal, such as nickel (Ni), or thin layer of conductive polymer, which is

labeled as AquaSave by Mitsubishi Corporation. Such materials enable the precise exposure of the correct structural linewidths while conducting the excess electrons away from the e-beam resist. The deposition of the thin metal layer or conductive polymer is usually applied directly after the spin-coating and solvent baking of ZEP resist, as shown in the following figure. Other fabrication procedures are not affected by the introduction of e-beam lithography assistive materials, which can be simply peeled off in the case of the thin metal layer, or be washed away by deionized water in the case of the conductive polymer.

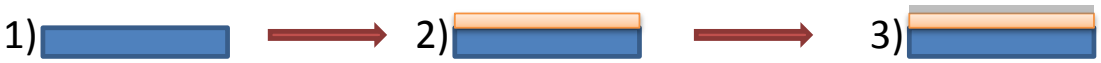

Figure 25: Covering ZEP resist with conductive thin film of metal or polymer (step 3) immediately after deposition and curing of resist (step 2).

The aforementioned methods can also be conveniently applied to stratified dielectric films that are susceptible to excess electron charging and exposure. Additional fabrication steps, such as the deposition of a continuous metallic groundplane, may be a necessary inclusion for devices that operate in reflection. Otherwise, the finished structure can be tested and characterized for evaluation of its power throughput and polarization spectrum.

2.3.2 Infrared Spectroscopic Ellipsometry

Spectroscopic ellipsometry refers to a unique measurement technique and associated apparatus that is able to quantify the change in polarization upon reflection or transmission from a multilayered dielectric structure [8,9,116]. Ellipsometry measurement is most often performed

with an assembly of polarization optics, detectors, and sources, which are collectively described as an ellipsometer. As an example, the aforementioned IR-VASE ellipsometer, shown on Figure 26, can extract polarization and power throughput metrics from 2 μm to 30 μm due to its broadband glow-bar IR source and HgCdTe detector array.

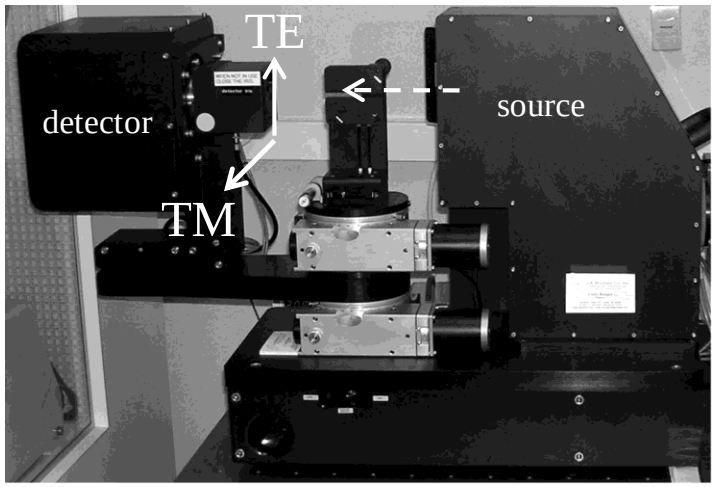

Figure 26: IR-VASE apparatus with preset coordinate system.

The change in polarization is interpreted from a measured deviation in reflected or transmitted intensity. Directly after the source, a polarization state generator (PSG) orients specific optical polarization components to produce a known and calibrated state of polarization, which is fed into the computer control system. The state of polarization that exits the material system can be acquired by evaluating the ratio of power throughput coefficients in the TE and TM coordinate directions, which are shown on the above figure. For example, the polarimetric constants δ and ψ that define the polarization ellipse can be deduced from the ratio of reflected TE and TM power coefficients

$$\rho = \tan(\psi) \cdot \exp(i \cdot \delta) = R_{TE} / R_{TM} \ . \tag{58}$$

Similar measurements can also be obtained in transmission. With the output state of polarization readily available by the aforesaid methods, the change in polarization can be detected by the polarization state analyzer (PSA) that is situated in front of the broadband IR detector array. This provides a unique capability that, when implemented at certain angles of incidence in reflection, can supply sufficient data to retrieve the optical constants and thickness of dielectric films and substrates over the operational band of the IR-VASE [116]. Such a method is made possible by internal calculations that determine the necessary material properties and layer thickness that would result in the measured Fresnel reflection coefficients and polarimetric quantities. This defines the fundamental principle of spectroscopic ellipsometry, which is able to deduce the refractive index and thickness of a whole host of materials over the IR spectrum, from dielectrics and metals to semiconductors and birefringent films [8,9].

The IR-VASE system is not only useful for determining optical constant and thickness data; it can also directly acquire the state of polarization that is transformed by a subwavelength meanderline retarder. The retrieved polarization metrics δ and ψ exactly correspond to the differential phase shift and auxiliary angle of Equations 31 and 33, which can be directly inserted into Equation 32 for accurate assessment of the axial ratio. Thus, the polarimetric performance of a multilayer meanderline structure can be attained from direct measurements of quantities that exactly prescribe the polarization ellipse, as was observed in Section 1.1.

The same IR-VASE system can also be used to perform a power transmission or reflection scan for each multilayer meanderline retarder under test. This measurement collects the power transmission or reflection coefficients listed in Equations 29 and 30 for both TE and TM polarization states. The pre-set coordinate system on the IR ellipsometer, which is shown on

Figure 26, facilitates alignment and subsequent measurements so that each orthogonal state of polarization directly corresponds to the TE and TM modes of the meanderline polarizer under test. Since the power transmission/reflection and spectroscopic ellipsometry measurements are completely automated, the meanderline polarizer has to be aligned to this coordinate system so that accurate readings can be acquired for the polarimetric quantities ψ, δ and the power throughput coefficients. It should be noted that, because of the bulky size of the detector assembly, the minimum angle for reflection measurements is affixed at 25° to avoid a potentially hazardous collision between the source and detector housings.

2.3.3 Single-Wavelength Testing at 10.6 μm

Single-wavelength characterization of device performance can often serve as a decent validation of measurements that were acquired by other methods, such as spectroscopic ellipsometry. In order to compare and contrast polarimetric and power throughput metrics, a simple system setup was constructed to verify the results from a set of transmissive meanderline retarders at the CO_2 lasing wavelength of 10.6 μm. Figure 27 shows a picture of the laser that was used in optical bench-top testing of the transmissive multilayer structures.

Figure 27: Picture of CO_2 laser system from Access Laser Co.

The polarization characteristics of the transmitted beam were acquired by intensity-based measurements of the Stokes vector coefficients. Recall that Figure 2 and Equations 8 through 11 detail the setup and process of obtaining the Stokes parameters of a randomly polarized beam that impinges upon the polarization analysis optics of the system. The only difference in the setup that was implemented is that the meanderline QWP device under test (DUT) was inserted just before the analyzing QWP, and was preceded by a linear polarizer so that CP could be obtained upon transmission. This modified setup is depicted by the following figure.

Figure 28: Single-wavelength measurement of Stokes parameters with a 10.6 μm CO_2 laser. Note that S_0 through S_2 are measured with only the detector (DET) and linear polarizer (LP) in front of the device under test (DUT). Acquisition of S_3 requires a single-λ crystalline QWP to be inserted.

For comparison purposes, the Stokes parameters of Equation 6 can be re-written in terms of the output polarimetric quantities of the polarization ellipse, which are directly measured by the IR-VASE system [3,8]

$$S = \begin{bmatrix} S_0 \\ S_1 \\ S_2 \\ S_3 \end{bmatrix} = S_0 \cdot \begin{bmatrix} 1 \\ \cos 2\psi \\ \sin 2\psi \cos\delta \\ \sin 2\psi \sin\delta \end{bmatrix}. \tag{59}$$

Once the Stokes coefficients are obtained via the six required measurements detailed in Equations 8 through 11, the polarization ellipse parameters immediately follow suit, since the differential phase shift and axial ratio are directly defined by the measured values of δ and ψ. Thus, the Stokes vector measurement with a 10.6 μm laser results in the same polarimetry information as the ellipsometer, only that the IR-VASE collects the signal from a broad spectrum of thermal IR radiation that passes through the DUT.

CHAPTER 3: MEASURED AND SIMULATED RESULTS FROM MULTILAYER INFRARED MEANDERLINE RETARDERS

3.1 Transmissive Achromatic Meanderline Waveplates

In this section, we shall present the numerical and experimental findings concerning transmissive multilayer meanderline retarders in a semi-chronological order, such that the evolution and advancement of the design, modeling, and fabrication process is documented in sufficient detail. Additional measurements pertinent to real-world applications of multilayer meanderline QWPs will also be demonstrated. The first batch of results, presented in Sections 3.1.1 and 3.1.2, demonstrate the capability of HFSS to accurately replicate the experimental data obtained from spectroscopic ellipsometry of achromatic multilayer meanderline retarders over a given IR waveband. Following these preliminary assessments, a comparative study between 1-layer, 2-layer, and 3-layer meanderline QWPs at 10.6 μm shall be presented in Section 3.1.3 in order to gauge which multilayer design exhibits the best transmission throughput, and if any improvement in the design yields optimum power throughput values similar to that of form-birefringent retarders. Regarding the aforementioned multilayer study, Section 3.1.4 contains numerical and experimental data of a 2-layer meanderline QWP that was specifically designed to achieve greater than 70% power throughput. Finally, Section 3.1.5 will present angle-dependent polarization and power transmission data over the LWIR spectrum from a 2-layer meanderline QWP, from a crystalline QWP designed for 9.55 μm, and from a form-birefringent retarder that was designed and simulated in HFSS. The acquisition of data over a half-angle of an F/1 cone represents a realistic imaging scenario that is typically encountered in a thermal polarimetry

system. This provides a suitable comparison benchmark between application performance of multilayer meanderline QWPs, crystalline QWPs, and numerical data associated with form-birefringent retarders.

3.1.1 Single-Layer Test Structure for the Mid-Wave Infrared

The first line of inquiry begins with comparing the spectral transmission and polarimetric quantities between results obtained from HFSS computations and IR-VASE measurements. Initially, a single meanderline layer was fabricated upon an insulating fused silica substrate with gold elements as the conducting circuit material. A listing of dimensions, corresponding to Figure 16, and particular fabrication materials are included on Table 2 below. The following figure depicts the layer stack configuration and relevant materials, as well as an appended SEM image of the structure.

Table 2: Materials and dimensions (in μm) for single-layer retarder designed for MWIR operation.

Dimensions	lw1	lw2	lw3	DX	DY	pw	ph
	0.26	0.26	0.26	0.8	1.35	0.4	0.5
Materials	substrate	metals					
	SiO_2	Ti/Au					

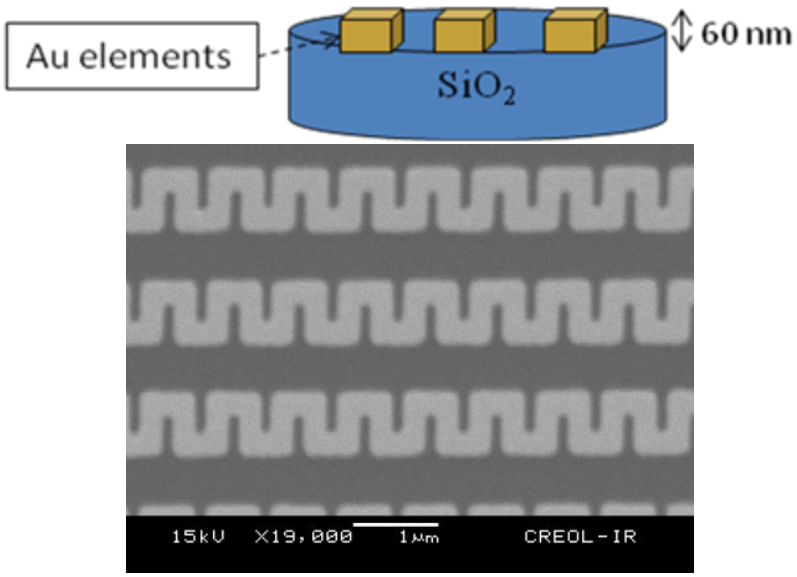

Figure 29: Schematic of single-layer meanderline retarder for MWIR and corresponding SEM micrograph.

The particular design goal was for the single layer to achieve around 45° phase shift in the MWIR band, such that a dual-layer combination would yield approximately 90° (or $\pi/2$) retardance with the correct interstitial dielectric layer thickness. Figure 30 shows the experimental phase shift δ from the IR-VASE apparatus and the computational results from HFSS for the single-layer MWIR retarder on fused silica. Note the astonishing level of agreement between simulated and measured parameters.

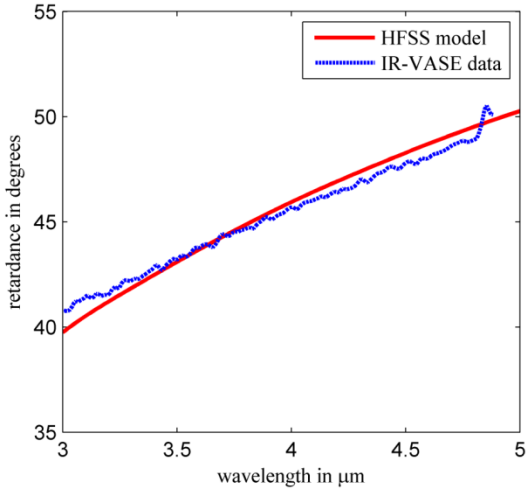

Figure 30: Simulated and measured data for the phase shift from the single-layer meanderline retarder in the MWIR.

3.1.2 Dual-Layer Meanderline QWP for the Long-Wave Infrared

Having achieved a suitable correspondence between numerical and experimental data in the MWIR, a dual-layer meanderline retarder was then designed and fabricated for QWP operation in the LWIR. The structural dimensions and material parameters are given in Table 3, with the subsequent figure depicting the multilayer configuration along with a corresponding SEM image from one of the layers.

Table 3: Materials and dimensions (in μm) for dual-layer retarder designed for LWIR operation.

Dimensions	lw1	lw2	lw3	DX	DY	pw	ph	t_1
	0.52	0.52	0.52	2	2.8	1	0.9	0.64
Materials	substrate	dielectric	metals					
	BaF_2	BCB	Al					

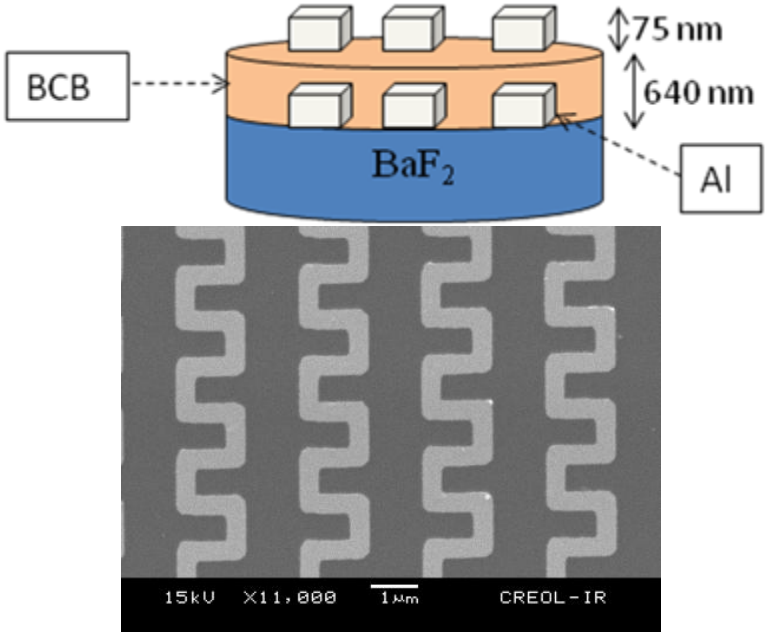

Figure 31: Schematic of dual-layer meanderline retarder for the LWIR and corresponding SEM micrograph of one of the layers.

The choice of dielectric substrate for the LWIR spectrum merits consideration, since barium fluoride (BaF_2) exhibits a high degree of broadband transmittance throughout the MWIR and LWIR bands [14,15]. However, it is somewhat difficult to work with, seeing as the BaF_2 substrate surface can easily scratch, and especially since the material is susceptible to thermal shock [15,118]. For these reasons, fused silica was employed in the MWIR, although it does exhibit strong attenuation beyond 5 μm wavelength [15], so it cannot be used as a transmissive substrate in the LWIR regime. Therefore, because of the relatively low optical density of BaF_2, it is the best choice for obtaining over 90% spectral power transmission in the LWIR without having to resort to multilayer anti-reflection (AR) coatings. Likewise, the interlayer dielectric polymer benzocyclobutene (BCB) is highly transmissive and exhibits a low refractive index

[116,118,121] much like BaF_2, which allows for multilayer admittance matching via the TMM algorithm. Still, there are some absorption peaks in the LWIR that correspond to phonon modes of the BCB polymer [116], which can actually be deciphered from both the spectral transmission and retardance data.

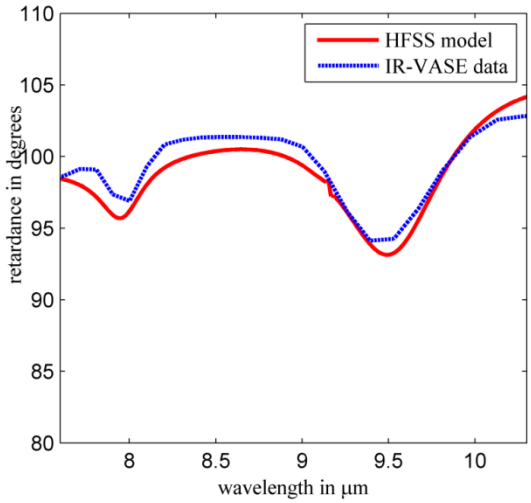

Figure 32: Simulated and measured data for the phase shift from the dual-layer meanderline retarder in the LWIR.

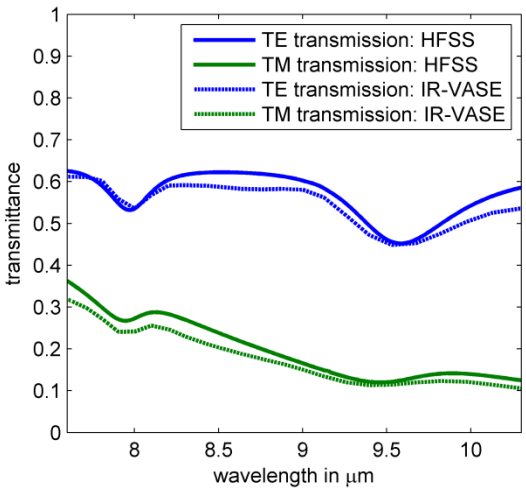

Figure 33: Simulated and measured data for the transmittance from the dual-layer meanderline retarder in the LWIR.

From the two preceding figures, we can deduce the importance of including realistic dispersive optical constants of materials in numerical full-wave simulations. Not only does the spectral power transmission correspond to the BCB absorption resonances, but the differential phase shift dips slightly at these locations, most likely due to the separate absorption magnitudes of the anisotropic surface current densities and field distributions at the material interface. Thus, the computational scattering parameters from HFSS crucially depend upon the validity of the material parameters that are inserted into the model, especially if real-world behavior is desired. Hence, while optimizing the structure, one could compensate for such characteristics even before the device is fabricated and tested. This capability is indispensible for meeting particular design criteria for multilayer meanderline QWPs.

3.1.3 Comparative Study Between 1-Layer, 2-Layer, and 3-Layer Meanderline QWPs at 10.6 μm

With regard to Figure 32, we have already obtained suitable achromatic QWP performance, but the average transmittance throughput leaves much to be desired. Therefore, we seek to compensate for the power transmission by adjusting meanderline array parameters and the interlayer dielectric cavity thickness so that a reasonable balance between 90° phase retardance and maximum power throughput is achieved. To this end, three separate multilayer meanderline structures were fabricated on BaF_2 substrates to test not only the capabilities of the TMM approach for optimizing and computing transmittance, but to also gauge the performance between 1-layer, 2-layer, and 3-layer structures so that the best admittance-matched device could be elected based upon the initial criteria. The wavelength of operation was chosen at 10.6 μm,

which is a common lasing wavelength in the thermal IR spectrum [122]. The resulting designs and material selections for the multilayer meanderline polarizers are indicated on the following table. Note that all of these parameters are designed with the intention of achieving QWP operation from each respective multilayer retarder.

Table 4: Materials and dimensions (in μm) for multilayered retarders designed for QWP behavior at 10.6 μm wavelength.

Dimensions	lw1	lw2	lw3	DX	DY	pw	ph	t_1	t_2
1-layer	0.45	0.8	0.45	2	1.7	1	1.1		
2-layer	0.4	0.4	0.4	2	2.7	1	1.1	1.5	
3-layer	0.2	0.2	0.2	2	2.75	1	1.1	1.13	1.3
Materials	substrate	dielectric	metals						
	BaF_2	BCB	Al						

The following figure depicts the layer stackup information for each multilayer meanderline polarizer, along with an SEM image from one of the layers on the corresponding structure.

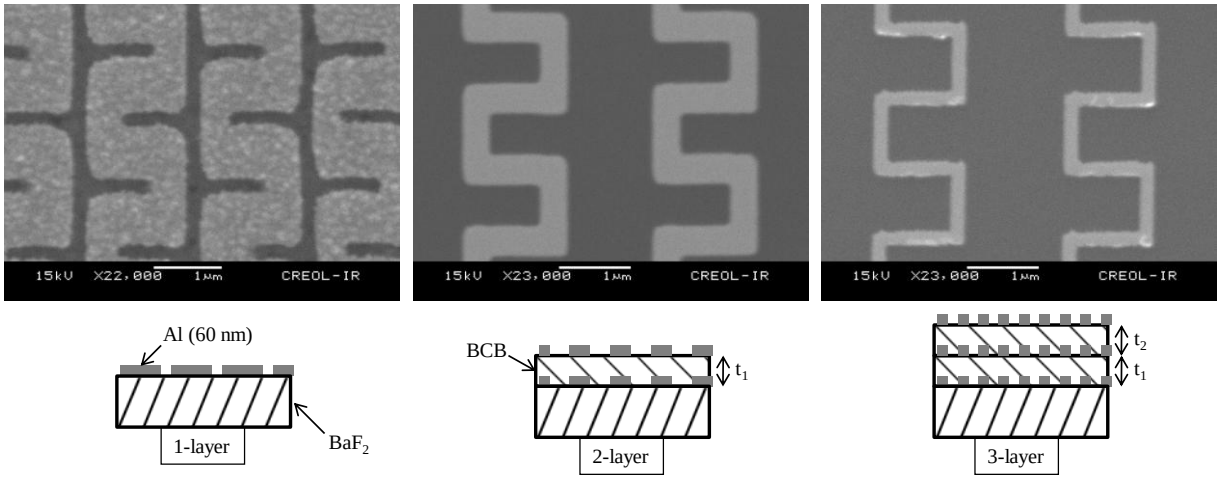

Figure 34: Multilayer configuration and SEM images for the three QWPs designed for 10.6 μm.

In order to benchmark the performance between each of the multilayered meanderline retarders, the axial ratio (Equation 32), the differential phase shift (Equation 31), and the total power transmission (Equation 34) will be presented. Table 5 summarizes these results for both the numerical and experimental data at 10.6 μm under normal incident illumination. It should be mentioned that the measured results consists of data collected from the IR-VASE system, and also from readings taken from manual Stokes parameter measurements with a 10.6 μm CO_2 laser (refer to Figures 27 and 28). Since the design criteria calls for QWP behavior at 10.6 μm, the values of the phase shift and axial ratio should be optimized for 90° and 1, respectively.

Table 5: Numerical and experimental results for the multilayer meanderline QWP study at 10.6 μm.

	δ	AR	T_{total}
1-layer QWP			
IR-VASE	77.79°±.678°	1.972±.0103	36.84% ±.37%
10.6 μm laser	73.72°±7.02°	1.975±.12	34.37%±3.26%
Ansoft HFSS	81.02°	1.604	39.43%
TMM	96.95°	1.998	39.41%
2-layer QWP			
IR-VASE	86.51°±.909°	1.206±.006	65.81%±.652%
10.6 μm laser	86.67°±2.38°	1.288±.125	65.14%±1.78%
Ansoft HFSS	89.37°	1.226	67.89%
TMM	92.65°	1.375	68.50%
3-layer QWP			
IR-VASE	83.38°±.753°	1.253±.008	58.09%±.783%
10.6 μm laser	82.19°±.684°	1.209±.024	59.72%±.059%
Ansoft HFSS	82.18°	1.259	59.41%
TMM	82.25°	1.372	60.53%

Most of the numerical results, from the HFSS model and from the wave TMM approach, agree very well with the corresponding experimental data. However, the axial ratio of the single-layer

meanderline polarizer predicted by HFSS shows some discrepancy, as compared to the measured value. This could be attributed to structural non-idealities that occurred during fabrication, such as over-exposure of the critical linewidths, or surface roughness upon the metallic Al meanderline elements. Additionally, the predicted phase shift given by the TMM model deviates by about 15% from the expected measured value for the single-layer meanderline retarder. Recall that the TMM algorithm uses the complex amplitude reflection coefficient to solve for the equivalent surface admittance of a given meanderline surface discontinuity. When calculating the equivalent parameters for a meanderline layer with a high proportion of metal, the reflection coefficient only registers the properties of a highly-reflective surface. Thus, certain information from a highly-reflective meanderline surface does not get imparted to the reflection coefficient, such as the absorption loss that occurs upon transmission through the meanderline layer. Therefore, the predicted phase shift from the TMM model for a single layer meanderline QWP does not account for the ohmic losses [104] from within the metallic elements, which duly affect the polarimetric quantities that are predicted by full-wave HFSS simulations. However, for meanderline structures with more than a single layer, the TMM model increases in accuracy, since the magnitude of absorption loss decreases along with the metal fill factor for a single layer embedded in a multilayer stack.

With regard to the fill factor of the meanderline layers, it is interesting to note that, in order to obtain QWP behavior for all three multilayered devices, there are certain constraints on the circuit-element dimensions that were set during the design phase, which not only affect the polarimetric behavior, but also the transmission response. One can see that, for an *N*-layered meanderline QWP, the accumulated phase shift can be distributed between each successive layer,

such that each layer contributes $\pi/2N$ phase shift. Accordingly, the dimensions of the meanderline elements required to produce such distributed phase shifts can be subsequently relaxed as the number of layers N increases. By this, we mean that the circuit linewidths are able to be reduced in dimension, which likewise reduces the magnitude of the inductive and capacitive admittance phase offsets [86,92,94–97]. Referring to the SEM images of each multilayer structure on Figure 34, we see that this is exactly the case, as the increase in layer count allows for the respective circuit linewidths on each layer to decrease in order to maintain QWP behavior. However, with the increase in number of layers, one would initially presume that the accumulative absorption loss would also increase. From a pure fill-factor standpoint, we find that this is not true, since the total percentage of metal in a multilayered QWP stack actually decreases with increasing number of meanderline layers. Figure 35 shows the fill-factor-based power transmission for a single layer and the corresponding multilayer structure, where the transmittance is simply given by

$$T = (1 - FF)^N , \tag{60}$$

where N is the number of layers, and FF is the metallic fill-factor percentage for a given unit cell design of a multilayer meanderline polarizer, whose dimensions are given on Table 4.

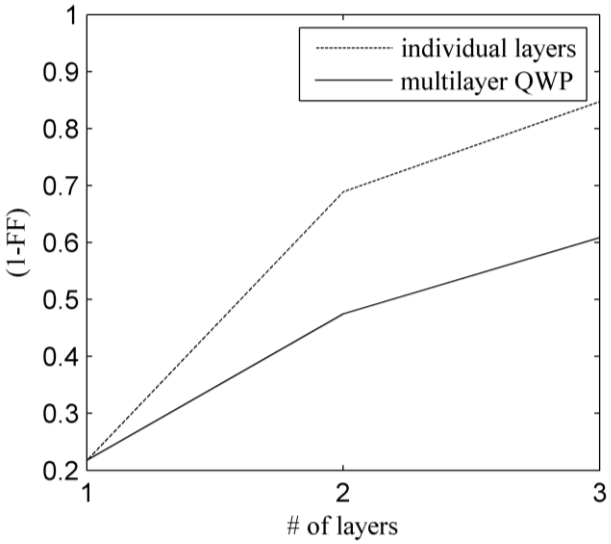

Figure 35: Fill-factor based transmission through a single layer and a multilayer structure designed to give QWP behavior.

Not only do we observe greater transmittance for more layers of a meanderline QWP, but we also see that the above formula, simple as it may be, is not a valid criterion for predicting the upper limit of power transmission throughput for a multilayered device. Besides not accounting for full-wave phenomenon, such as edge diffraction and surface wave scattering, the phase information that accumulates between the layers is not accounted for. In our previous treatment of the multilayer problem by means of TMM, the spacing, and thus, the phase separation between the meanderline layers plays an important role in determining the magnitude of the transmission coefficient. Therefore, the neglect of multilayer interference inhibits Equation 60 from making an accurate prediction for the power transmission throughput, since spatial coherence is preserved at length scales that are shorter than the operating wavelength [3,7]. However, if we were to separate each individual meanderline layer by hundreds of waves, then

with the decrease in coherence, we might see more agreement with the predictions from this simple approximation.

Selecting the best multilayer polarizer from those listed on Table 5, it is seen that the 2-layer structure exhibits both the best transmission and polarimetric characteristics of the three devices that were fabricated. This result might come as a surprise, since the 3-layer QWP has an additional meanderline layer which can match the admittance of the other layers at 10.6 μm, thereby resulting in increased potential power transmission. The limitation in this instance is the spin-on dielectric BCB that was used for the standoff layers. BCB has significant absorption effects in the LWIR band, which are seen in Figure 36. Thus, even though we would expect an increase in transmission throughput for the 3-layer structure, propagation through more than 2 μm of BCB mitigates any gains because of the accumulated absorption loss.

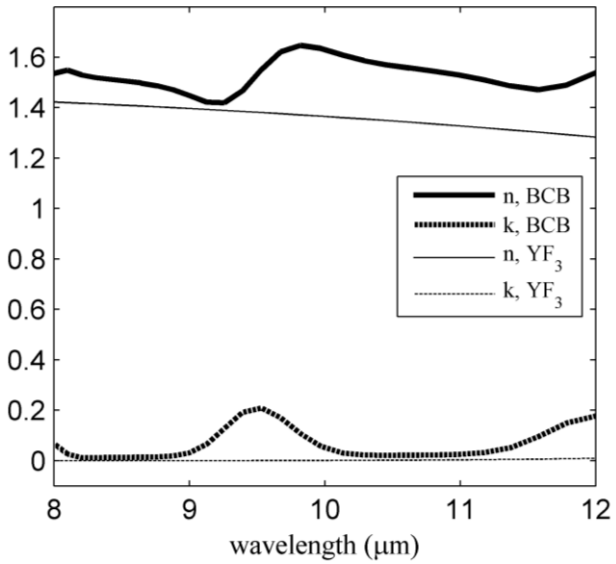

Figure 36: Optical constants of BCB and YF_3 thin films in the LWIR.

Since the 2-layer structure has 1.5 μm of deposited BCB, it wins outright simply because of decreased attenuation of optical transmittance. Alternate solutions for a suitable standoff layer have been considered, one possible choice being Yttrium Fluoride (YF_3). YF_3 is a ceramic material and fluoride compound, and is usually deposited via sputtering or evaporation [15,123,124]. Its optical properties were measured via IR ellipsometry and are seen in Figure 36. This particular material was not included in the current study due to the fact that it is difficult to deposit and process, and especially since it is known to contaminate evaporation chambers that would otherwise be used for multiple materials and processes. However, it exhibits very low loss in the LWIR band, so it would constitute the ideal material candidate for multilayer polarizers, or general highly-transmissive metamaterials for the infrared. Figure 37 shows the simulated power transmission and differential phase shift response for 2-layer and 3-layer meanderline QWP's that were designed for a center wavelength of 10.6 μm. The YF_3 dielectric material was included in the standoff layers.

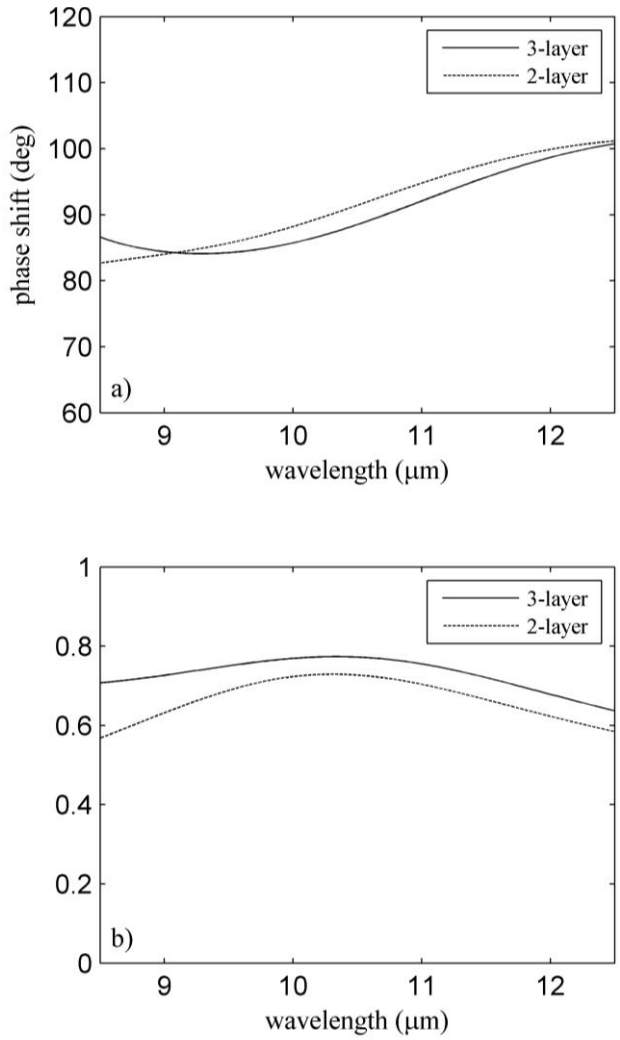

Figure 37: Simulated a) phase shift and b) power transmission response for 2-layer and 3-layer meanderline QWP's with YF_3 standoff layers.

Note that the 3-layer polarizer exhibits an increase in peak power transmission over multiple wavelengths, since each meanderline layer can match the effective admittance of the other layers at more frequency points, similar to a multilayer optical coating [105,106]. Similar gains in the power transmission response would also be expected for structures with even more meanderline layers. Even so, there may be a practical limit to this extrapolation, since the reduction of circuit

linewidths for additional layers might conflict with fabrication tolerances, or might even introduce non-ideal skin depth or quantum related effects for extremely thin metal wires [125]. Nonetheless, the inclusion of additional meanderline layers provides a design utility that assists in increasing the broadband spectral transmission throughput of a multilayer meanderline quarter-wave retarder.

3.1.4 Broadband Achromatic Meanderline QWP with Low-Loss Dielectric Standoff Layer

We shall now convey the results from a prototype 2-layer meanderline QWP that was fabricated on BaF_2 with a standoff layer of YF_3 dielectric material. Seeing as how the absorption loss of BCB severely restricted any further improvement in the spectral power transmission at LWIR frequencies, an attempt at using YF_3 was initiated to assess the possibility of reaching or breaking 70% power throughput. The completed 2-layer structure utilized the same design parameters of the corresponding dual-layer device listed on Table 4, only that the thickness of the interlayer YF_3 cavity was 1.46 μm, which was optimized via the TMM admittance extraction process. The following figure illustrates the retrieved phase shift and power throughput quantities from HFSS and IR-VASE methods.

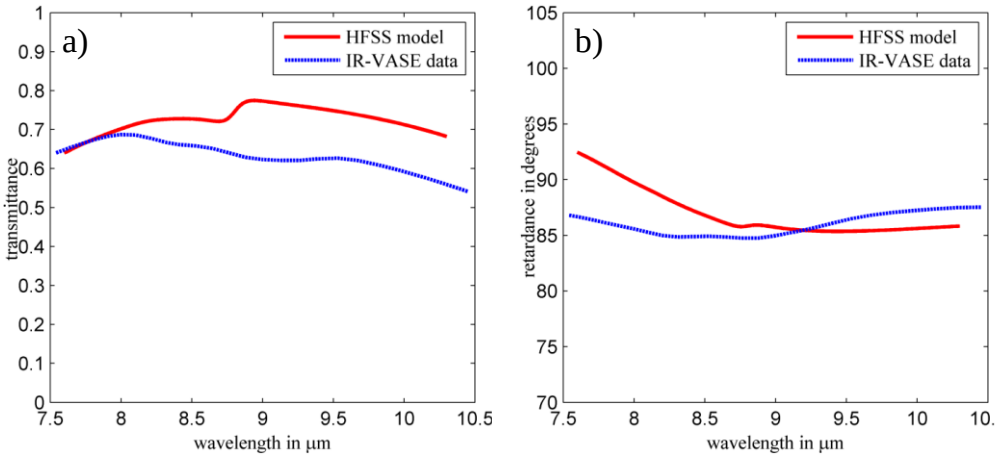

Figure 38: Comparison between simulated and experimental results for the a) transmittance and b) phase shift from a 2-layer QWP with YF_3 dielectric cavity material.

Although the measured phase shift is relatively close to the numerically-optimized value, the total average power transmission still does not exceed 70%, which somewhat contradicts the results from HFSS. This is most likely attributed to the ceramic quality of the YF_3 dielectric layer, which does not smooth out the features of the underlying meanderline layer. Figure 39 demonstrates this concept in a comparison between BCB and YF_3 depositions. Since BCB is a spin-on polymer, the material does not conform to any pre-fabricated shape, thus leveling out any features of pre-deposited elements on the preceding interface.

Figure 39: Differences in surface uniformity upon deposition of BCB and YF_3.

YF_3 on the other hand is a rigid ceramic fluoride compound that retains some of the topology of the previous layer. Thus, the elements that were patterned and deposited over the YF_3 cavity did not lie on a perfectly-flat surface, which could have introduced additional loss mechanisms, such as increased metal resistivity due to enhanced surface roughness of the meanderline conductors [104,126]. Nonetheless, this principle demonstration indicates that fabrication on YF_3 is possible, and that additional improvements can be had if the YF_3 layer is smoothened out, e.g. with mechanical polishing or deposition of a thin dielectric layer that removes the topographical features [14,121]. In any case, the previous and present sections have demonstrated that the power transmission of multilayer meanderline achromatic QWPs can be augmented to compete even with the best of the currently available state-of-the art technology [27–35].

3.1.5 Angular Sensitivity Analysis of Polarization and Transmission Metrics from Crystalline, Form-Birefringent, and Meanderline Quarter-Wave Retarders in the LWIR Spectrum

In this section, we present a comparative analysis between cadmium sulfide (CdS) crystalline, silicon (Si) form-birefringent, and multilayer meanderline QWP technologies in the LWIR spectrum. The goal of the study is to verify which QWP component would be most appropriate for imaging scenarios, such as in a thermal polarimetry system. To this end, we evaluate the polarization and power transmittance metrics over the half-cone angle of an impinging F/1 focused beam, which resembles a realistic imaging criterion. Analysis of angle-dependent metrics will be carried out with dramatic emphasis upon cost-effective performance, which limits the technological alternatives to those that can effectively provide broadband

achromatic QWP characteristics and sufficient power transmission throughput without having to resort to prohibitively expensive broad-band anti-reflection (BBAR) coatings.

The three aforementioned QWP technologies, which consist of the crystalline CdS retarder, the multilayer meanderline waveplate, and the Si form-birefringent retarder, are shown on Figure 40 with their respective TE and TM axes, which prescribe the coordinate directions corresponding to the orthogonal birefringence axes of the anisotropic material systems [8,9,27,92]. The CdS QWP component was manufactured by II-VI Incorporated (model # 010201-7) for single-wavelength operation at 9.55 μm. The multilayer meanderline retarder selected for this study is the same 2-layer device that was presented in Section 3.1.3 [86] with BCB as the interlayer dielectric cavity material. In contrast to the previous QWP components that were readily available for measurement, the Si form-birefringent retarder was modeled in HFSS, specifically because no other angle-dependent polarization and transmission metrics could be found in the current literature. Most form-birefringent gratings are characterized in collimated space at normal incidence [27,34,35], so it is imperative to perform independent analysis of form-birefringent retarders, such that angle-dependent behavior and conditions resembling illumination by an F/1 focusing system are accounted for.

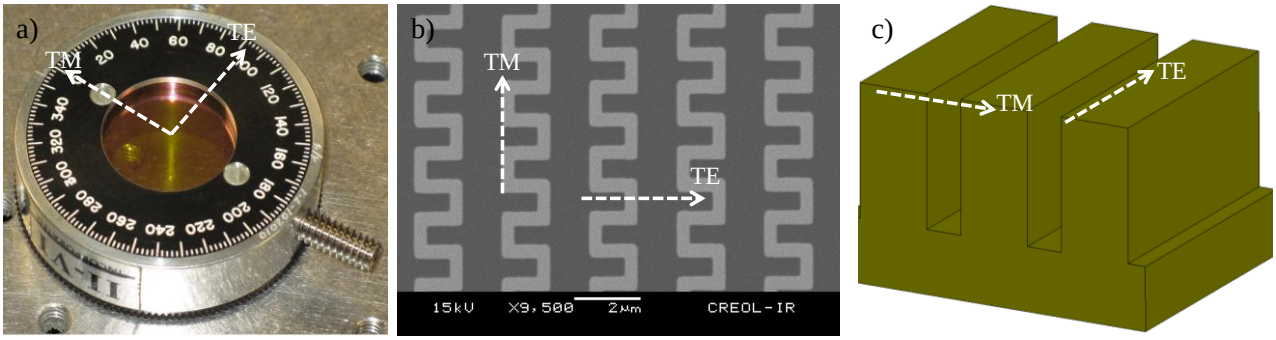

Figure 40: TE and TM coordinate directions associated with the respective birefringence axes of a) the CdS crystal, b) the meanderline metamaterial, and c) the form-birefringent grating QWPs.

Each QWP element was characterized by spectroscopic ellipsometry scans on the IR-VASE system of Figure 26. The measurement configuration on the IR-VASE apparatus allows for angular variation along one plane at a time, so for complete characterization, the device under test was rotated 90° to gauge the angular sensitivity along both planes of incidence that would be subjected to illumination from an F/1 system. The angle of incidence was swept from 0° in increments of 5.313° to the full half-angle of an F/1 cone, which is given as 26.565°. With regard to the equivalent birefringence axes of each QWP system, as shown on Figure 40, a full angular scan therefore involves rotating each QWP component along both planes of incidence associated with the respective TE and TM coordinate axes. As demonstrated in Figure 41, all QWP devices engage in TE and TM-planar scans so that the entire half-angle of the F/1 objective is registered. It should be mentioned that the simulations of the form-birefringent Si grating replicated these exact measurement conditions, thereby enabling a direct comparison between simulation output and measured performance metrics.

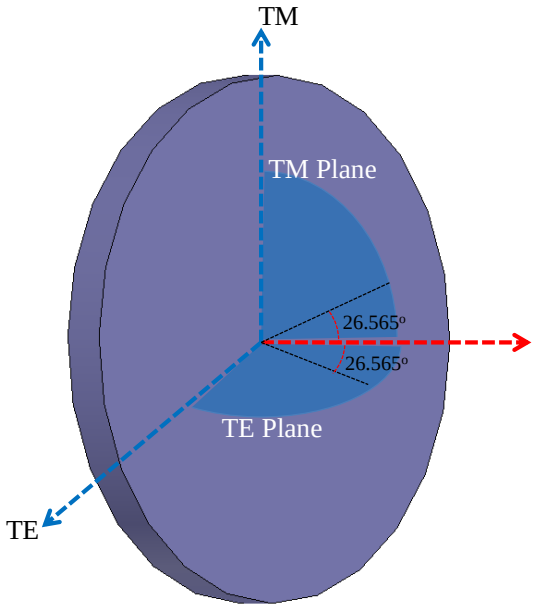

Figure 41: Conceptualization of TE and TM planar scans with indicated F/1 cone half-angle of 26.565°. The dashed red arrow is normal to the component surface.

Measured results from the CdS QWP element are shown below in Figures 42 and 43, which separately depict both TE and TM planar scans.

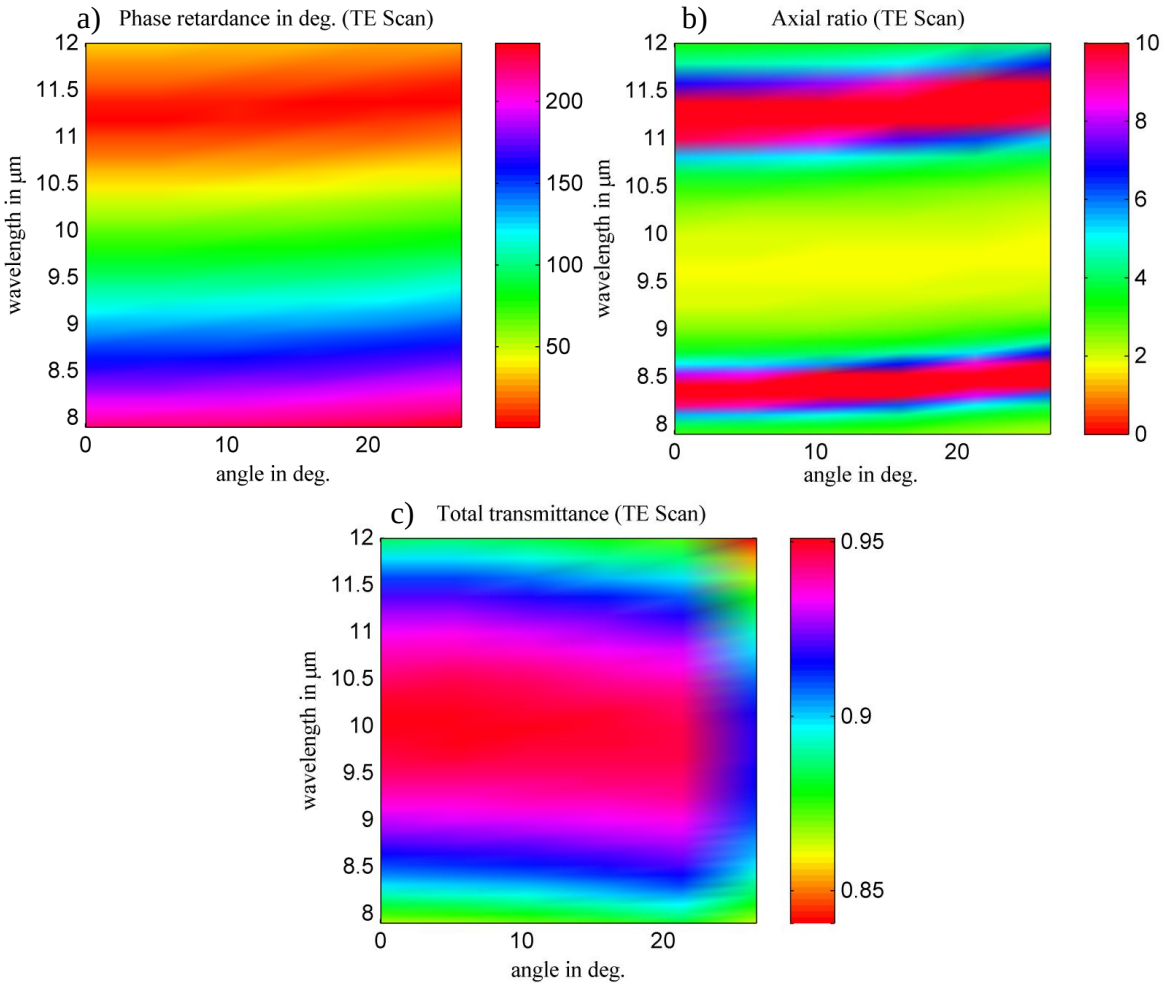

Figure 42: Angular variation of CdS QWP across TE plane of incidence for the a) phase retardance, b) axial ratio, and c) total transmittance in the LWIR spectrum.

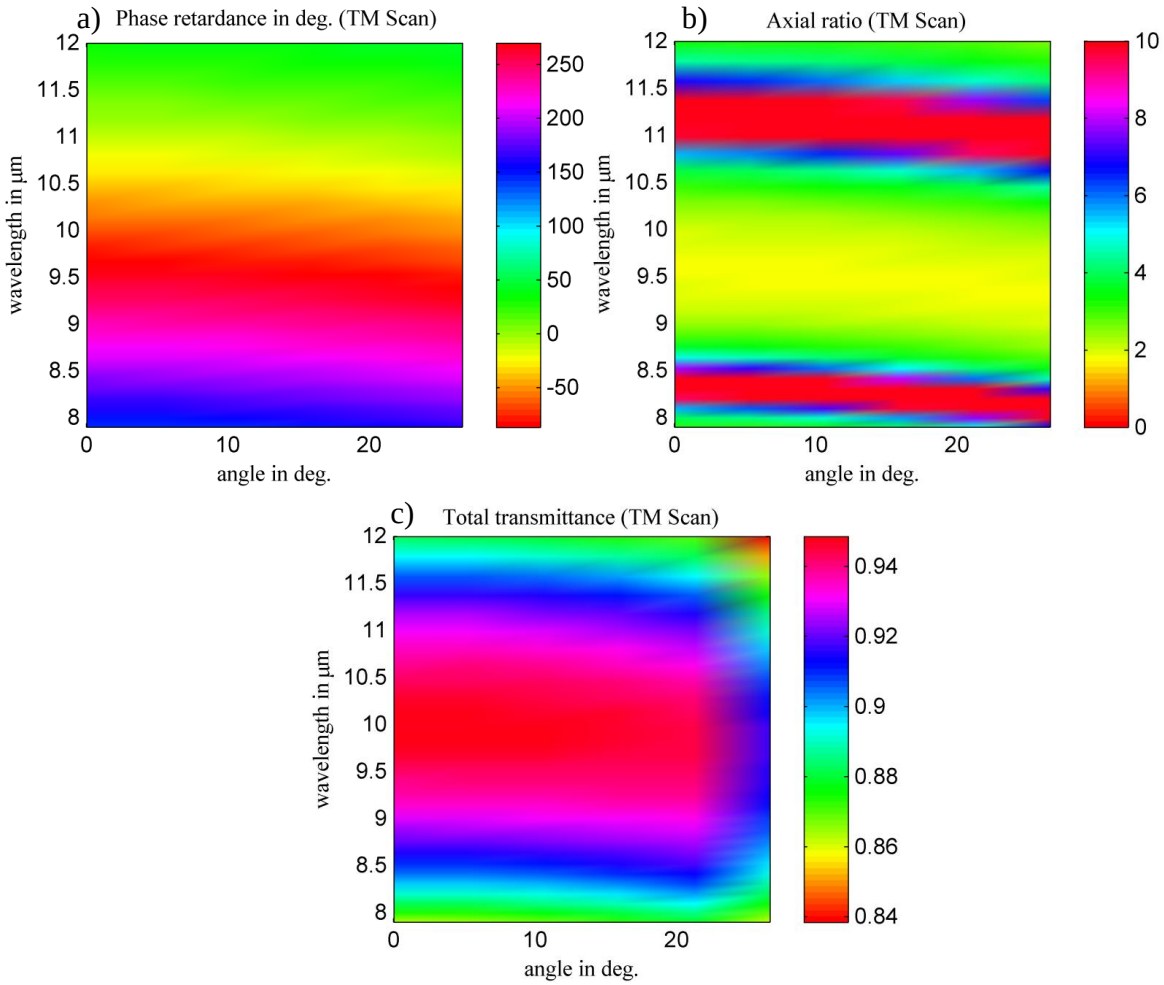

Figure 43: Angular variation of CdS QWP across TM plane of incidence for the a) phase retardance, b) axial ratio, and c) total transmittance in the LWIR spectrum.

Although the CdS retarder is highly transmissive and rather angle-insensitive throughout both scan configurations, the phase retardance exhibits severe chromatic dispersion, as was mentioned before of typical single-wavelength crystalline QWPs [12,13]. This dispersion is mirrored in the measured axial ratio of the CdS retarder, which only settles around the optimum value of 1 near the design wavelength of 9.55 µm. Thus, CdS QWPs are not the ideal component for broadband polarimetric imaging systems in the LWIR.

The ensuing results from the 2-layer meanderline QWP are presented. It should be noted that the interlayer dielectric of BCB exhibits a phonon mode near 9.5 μm, and again near 12 μm, which is why dips appear in the transmission and phase retardance spectrum for all scan angles under consideration.

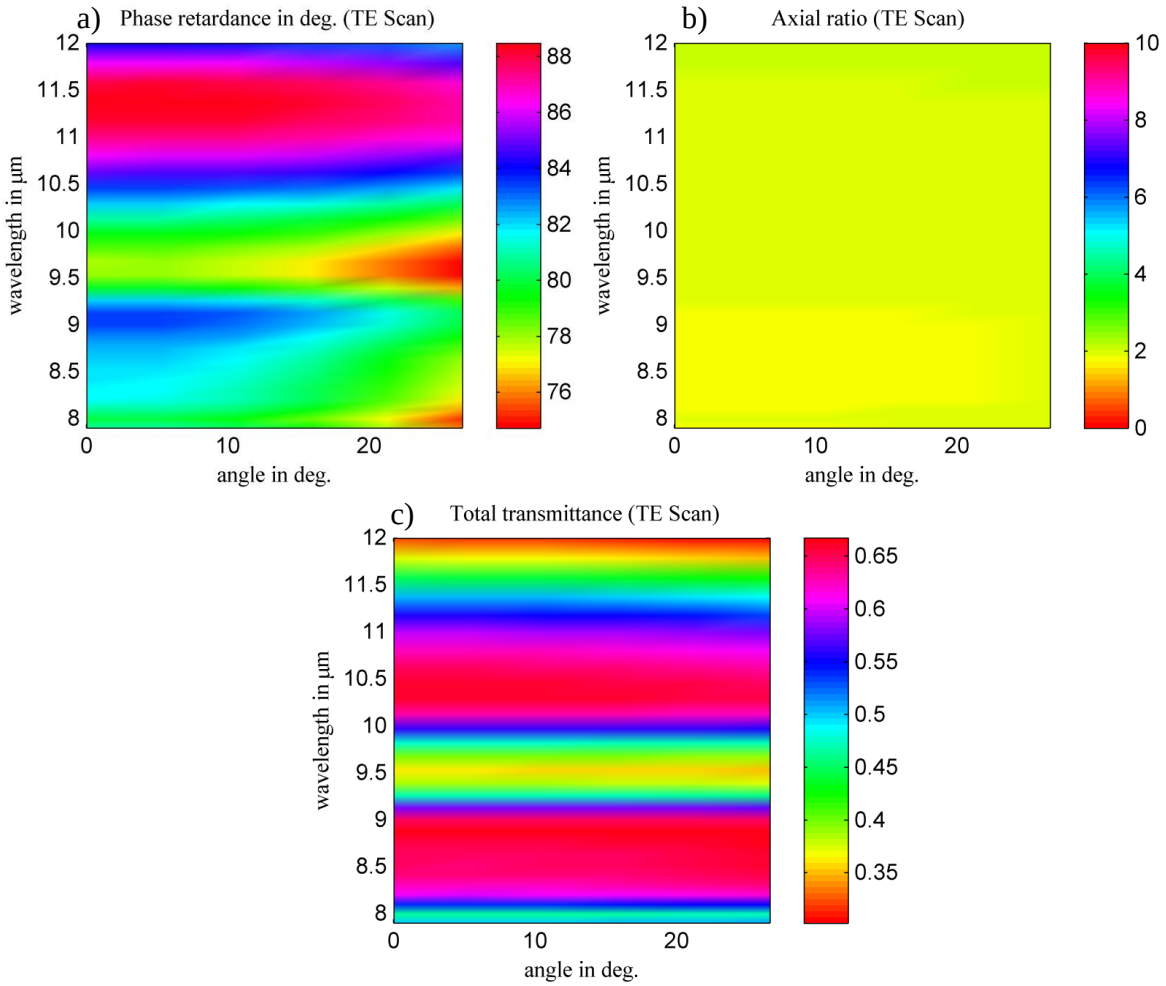

Figure 44: Angular variation of 2-layer meanderline QWP across TE plane of incidence for the a) phase retardance, b) axial ratio, and c) total transmittance in the LWIR spectrum.

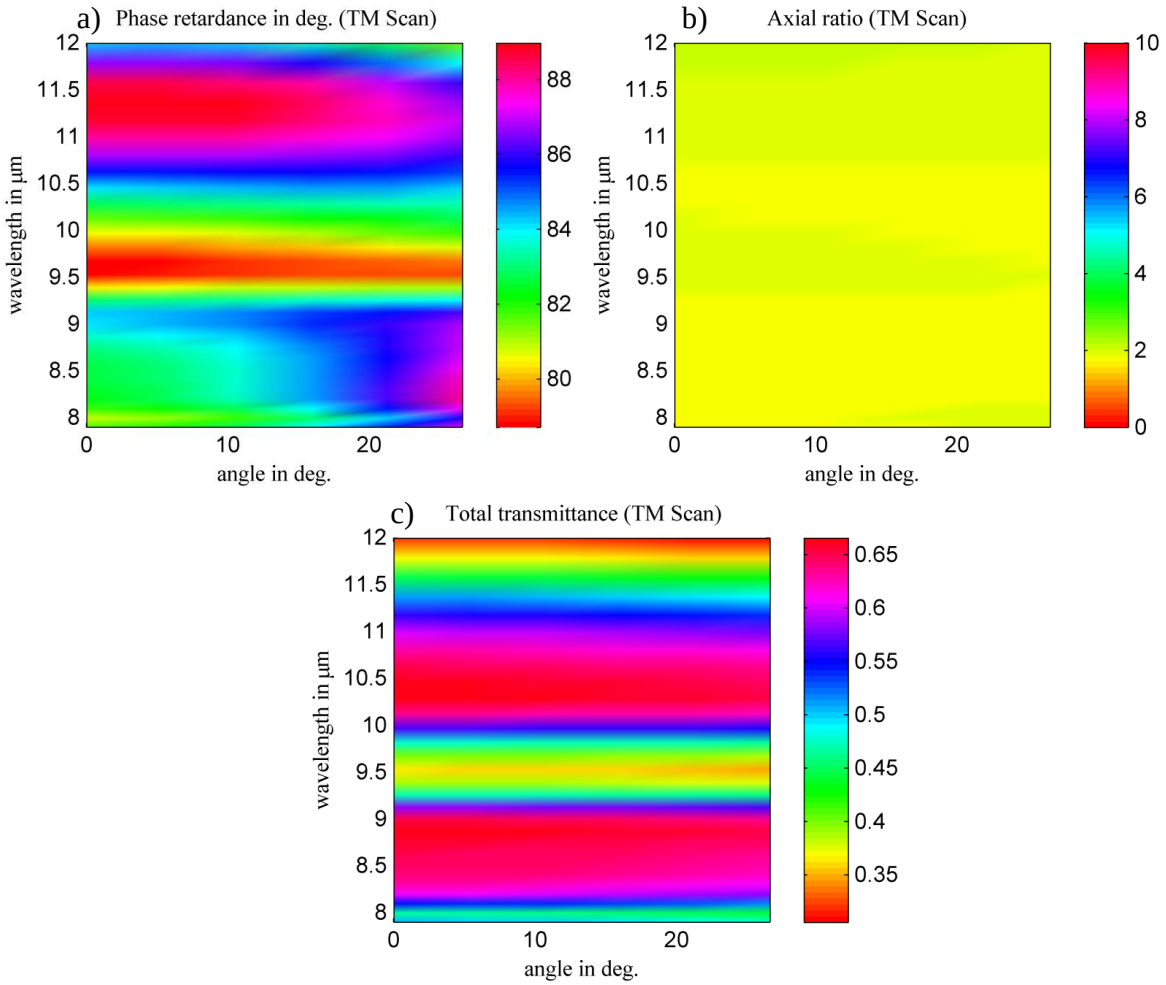

Figure 45: Angular variation of 2-layer meanderline QWP across TM plane of incidence for the a) phase retardance, b) axial ratio, and c) total transmittance in the LWIR spectrum.

In contrast with the CdS QWP, the 2-layer meanderline component is extremely achromatic with regard to its differential phase retardance and axial ratio, both of which are close to their optimum values of 90° and 1 throughout the LWIR band. Furthermore, it appears that all measured polarimetric and transmittance metrics do not exhibit any severe dependence upon the incident angle of illumination, which bodes well for potential F/1 imaging scenarios. The averaged power transmittance achieves a maximum of approximately 65%, which is decent

enough considering the scattering and ohmic losses encountered from the metallic meanderline elements [104], not to mention the optical attenuation through the BCB cavity dielectric layer. Although better transmission performance has been suggested with alternative dielectric materials [86,123,124], these series of measurements represent a solid foundation for achieving achromatic QWP characteristics that are equally insensitive to oblique incident angles from an F/1 objective.

We now consider the numerical results from the full-wave finite element simulations of the Si form-birefringent retarder, which was scaled from a design presented in [27]. Figures 46 and 47 subsequently depict the TE and TM scans of the polarimetric and power throughput coefficients.

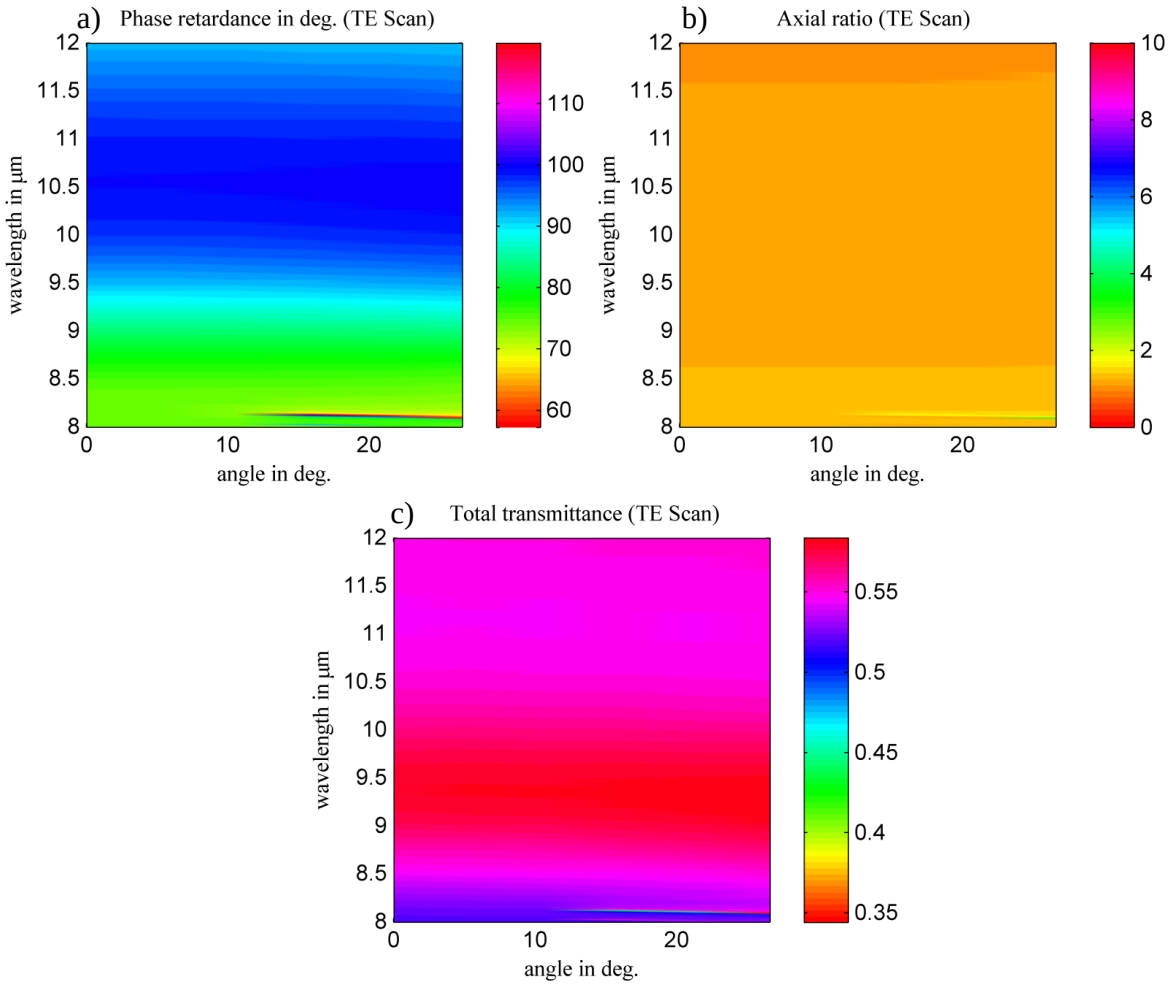

Figure 46: Angular variation of Si form-birefringent QWP across TE plane of incidence for the a) phase retardance, b) axial ratio, and c) total transmittance in the LWIR spectrum.

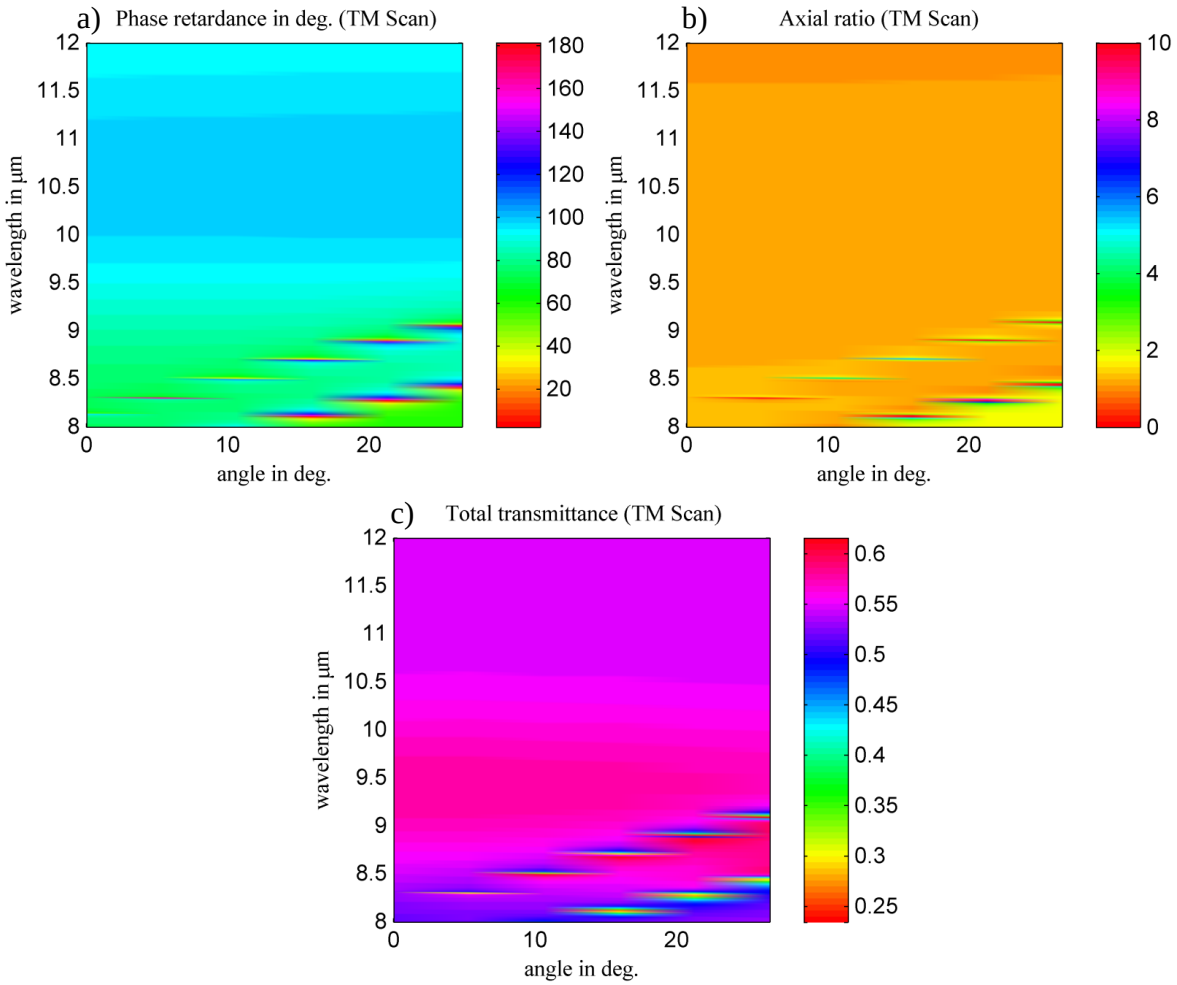

Figure 47: Angular variation of Si form-birefringent QWP across TM plane of incidence for the a) phase retardance, b) axial ratio, and c) total transmittance in the LWIR spectrum.

It should be mentioned here that the FEM analysis of the Si form-birefringent grating took into account losses incurred from the Fresnel reflections at the posterior interface of the substrate. This accurately resembles typical data taken from form-birefringent retarders presented in the literature [27,34,35], especially since BBAR coatings are extremely difficult and expensive to manufacture for high-index Si substrates.

With regard to the TM scan configuration on Figure 47, the incident angles beyond 0° exhibit grating lobes adjacent to the higher-energy wavelengths of the LWIR spectrum. Because the power transmission of the TM scan yields local minima for each instance of a grating lobe, such behavior can be associated with the occurrence of Rayleigh anomalies, which satisfy the following equation

$$\sin\theta_{in} = n_s \cdot \left(1 - \frac{m \cdot \lambda}{n_s \cdot P}\right), \tag{61}$$

where n_s is the refractive index of the substrate, m is the grating order, P is the grating periodicity, λ is the free-space wavelength, and θ_{in} is the incidence angle [127]. Each manifestation of Rayleigh phenomena redirects energy from the principle specular modes into higher diffraction orders, consequently diminishing the transmittance and depolarizing the signal that reaches the FPA detector [127,128]. In special circumstances, the higher-order modes may be completely evanescent, thereby restricted to surface waves that travel along the plane of the grating interface. This can be seen in Figure 48, which depicts a resonant surface wave of the grating that almost completely absorbs the energy of the incident field.

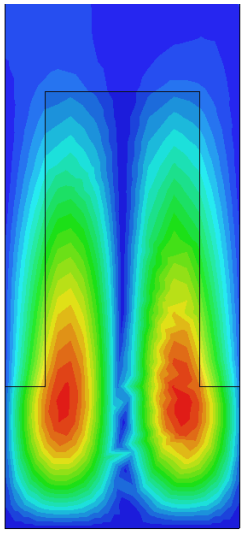

Figure 48: Rayleigh anomaly at approximately 8.2 μm with incident angle of 15.939°. Incident energy is redistributed to a high-order diffraction mode, which happens to be an evanescent surface wave.

The TE scan does not portray such scattering phenomena, since the plane of incidence is orthogonal to the grating wavevector of the subwavelength form-birefringent structure. Therefore, even though the overall phase retardance and axial ratio exhibit achromatic QWP and near angle-insensitive qualities, the grating lobes stick out like proverbial sore thumbs, which cannot be rectified by any post-processing algorithms of broadband imaging polarimeters. Lastly, the average power transmission is capped near 60%, which is slightly inferior to the maximum threshold transmittance of the 2-layer meanderline retarder. The decreased throughput is indicative of Fresnel losses that originate from the back side of the uncoated Si substrate. If we were to consider application of a BBAR coating, the form-birefringent retarder would definitely win out solely due to the increased transmittance over the 2-layer meanderline QWP. However, we are also considering cost into the performance criteria, which precludes us from assuming a BBAR-coated Si grating, if we are to justly compare form-birefringent with multilayer

meanderline technology. Therefore, as it stands, multilayer meanderlines are the better alternative, especially since the polarization spectrum does not witness any extraneous diffraction grating phenomena, and the transmittance can be improved by simple substitution of BCB for other low-loss dielectrics, such as YF_3 [123,124], without having to rely upon BBAR coatings. This grants multilayer meanderlines more flexibility in terms of device integration and cost-performance value in broadband thermal polarimetry systems.

3.2 Reflective Achromatic Meanderline Waveplates

As outlined in the introductory chapter of this dissertation, reflective QWPs for the IR spectrum have utilized several different technologies to achieve CP light upon reflection [16–20,44–46]. For instance, reflective prisms [16,17] with or without thin-film interference layers [18–20], and microstructured surface-relief gratings [44–46] have demonstrated ideal $\pi/2$ phase retardance between orthogonal field components in the IR. Although the aforementioned devices are well-suited for their intended applications, they do have a few drawbacks. In particular, the reflective QWP prisms are quite bulky and expensive, and the reflective microstructured phase retarders are typically optimized only for a narrow spectrum around the design wavelength [44,45]. Ideally, a component would combine a low-cost compact planar structure with broadband performance. Subwavelength elements as broadband reflective phase retarders have been previously demonstrated in the microwave regime as a polarization twister, which rotates the plane of polarization by 90° upon imparting a π phase shift between orthogonal field amplitudes [129–131]. One such design of a twist reflector incorporated the versatile

meanderline FSS unit cell element [130], which has been established in the previous sections (3.1.2–3.1.5) as a promising candidate for achromatic transmissive QWPs in the LWIR [86,98–100]. We therefore adapt this LWIR meanderline concept for use as a broadband reflective QWP.

3.2.1 Single-Layer Meanderline Stratified Above a Reflective Groundplane for LWIR Applications

The design of a broadband reflective meanderline QWP was carried out within the ANSYS HFSS program, which employed a built-in Newtonian search algorithm to refine the geometrical parameters. The resulting meanderline geometry from the structural optimizations is shown in Figure 49, along with a depiction of the layer stackup utilized in the HFSS simulations.

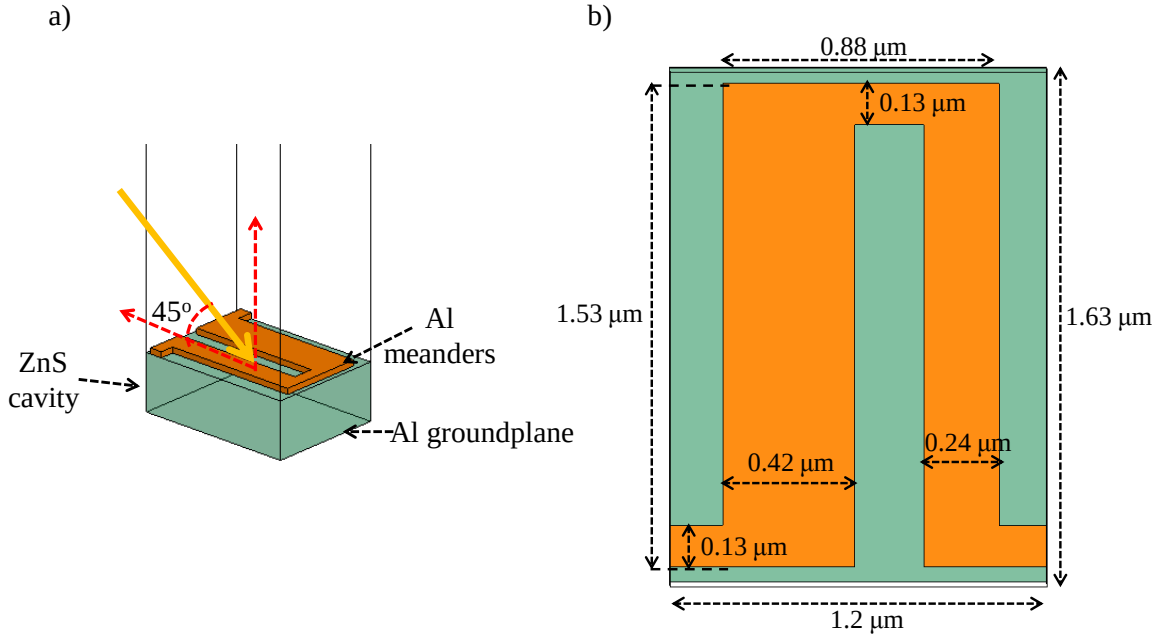

Figure 49: Illustration of a) unit cell configuration in HFSS, where the yellow arrow represents the incident beam, and b) the optimized design parameters of the meanderline geometry.

The design was originally simulated with a 45° angle of incidence, in a plane parallel to the plane of periodicity associated with the equivalent TE mode of the meanderline grid (Figure 19). The optical properties of each material used in the model were measured by spectroscopic ellipsometry [9,116]. The meanderline elements and the groundplane were aluminum (Al), and the dielectric layer was zinc sulfide (ZnS), whose measured optical constants are shown on the following figure.

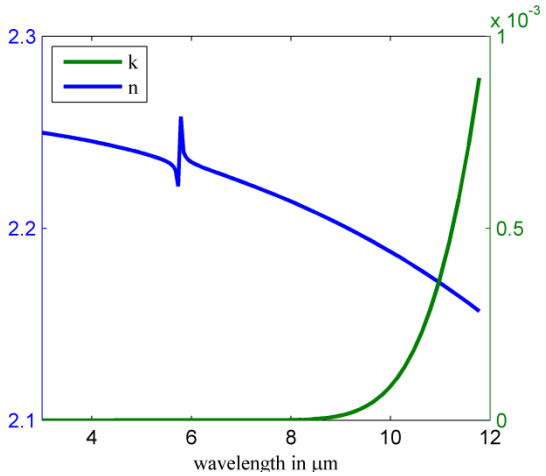

Figure 50: Optical constants for ZnS measured by IR spectroscopic ellipsometry.

Simulations were performed over the full LWIR band, and results from the optimized design are shown in Figure 51.

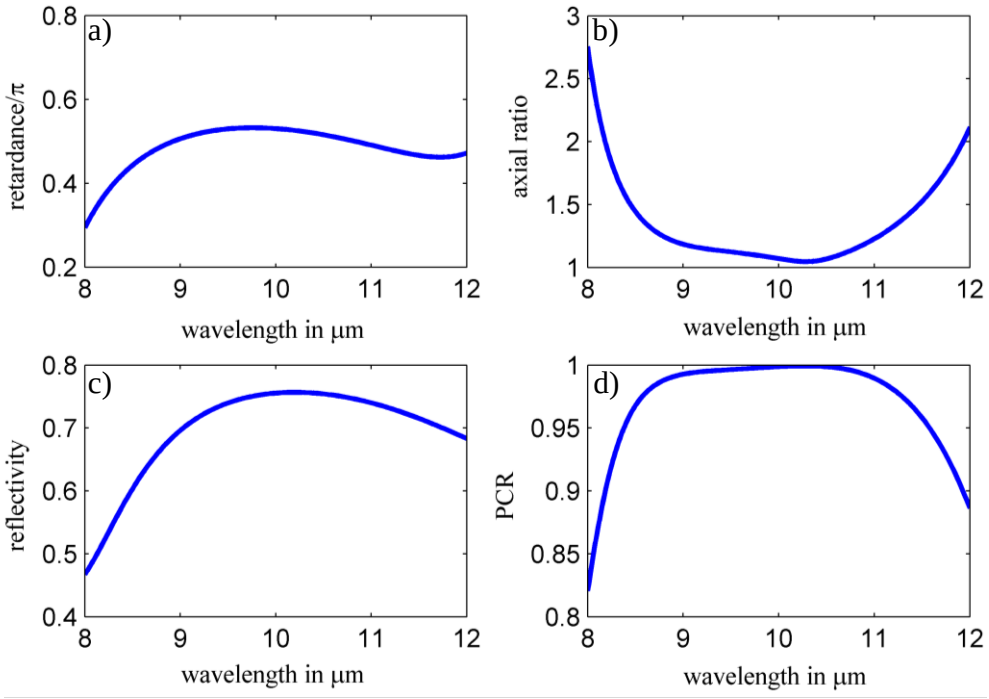

Figure 51: Simulated polarimetric and power reflection parameters from HFSS, where a) is the spectral phase retardance, b) is the axial ratio, c) is the polarization-averaged power reflection coefficient, and d) is the polarization conversion ratio.

As one may recall, in order to obtain perfect conversion from a 45° linearly-polarized (LP) incident field into CP output, a differential phase shift of π/2 and AR of 1 are desired. Figure 51 shows that the simulated differential phase shift is very close to π/2 across the LWIR, and the AR is less than 2 over most of the band, which are good indicators of efficient conversion of LP into CP [8,95]. We also computed the percentage of circular polarization that is obtained upon reflection from the meanderline QWP. This polarization conversion ratio (PCR) can be written the ratio between the reflected state of polarization and the total field intensity [130]

$$PCR = \frac{(\sqrt{R_{TE}} - i \cdot \sqrt{R_{TM}} \cdot \exp(i \cdot \delta))^2}{2 \cdot (R_{TE} + R_{TM})}, \tag{62}$$

where R_{TE} and R_{TM} are the power-reflection coefficients for the TE and TM modes. Since the reflected orthogonal components are expected to be $\pi/2$ out of phase, the above formula results in a value of 1 when the TM component is phase-shifted by $\pi/2$ and the amplitudes are equal in magnitude, which signifies complete conversion of an incident 45° LP beam into CP. The simulated PCR plotted in Figure 51 never dips below 85%, which suggests that the majority of the reflected beam will be CP. The polarization-averaged power reflection coefficient, also shown in Figure 51, is approximately 75%, which is adequate for some broadband imaging applications, although a higher efficiency would be required for use with high-powered laser systems. The materials that were selected for the design are representative of the best materials in the LWIR as far as ohmic loss and absorption are concerned. However, as Figure 51 shows, there is still a significant power absorption caused by multiple reflections between the meanderline elements and the groundplane [104]. The tradeoff inherent in reflective meanderline QWPs, as compared to other design types, is that a lower power efficiency is the cost for achieving broadband performance. The numerical results presented are representative of a structure optimized for power reflection that would give a broadband LP-to-CP conversion in reflection.

The submicron dimensions shown in Figure 49 were fabricated by standard e-beam lithography techniques [118], which were covered in Section 2.3.1. An SEM image of the final reflective meanderline QWP element is shown below in Figure 52.

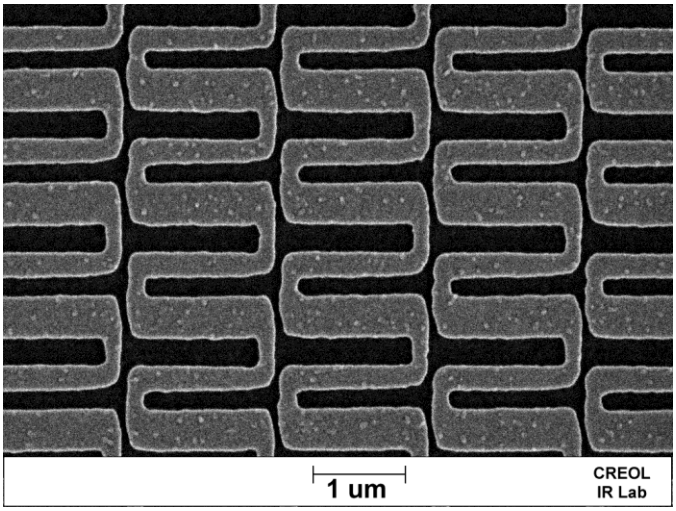

Figure 52: SEM image of fabricated reflective meanderline FSS array.

After fabrication was completed, the structure was measured via reflective spectroscopic ellipsometry with the IR-VASE system (Figure 26) set for 45° angle of incidence. The resulting experimental polarimetric, power reflection, and PCR data for the reflective meanderline QWP are subsequently displayed on Figure 53.

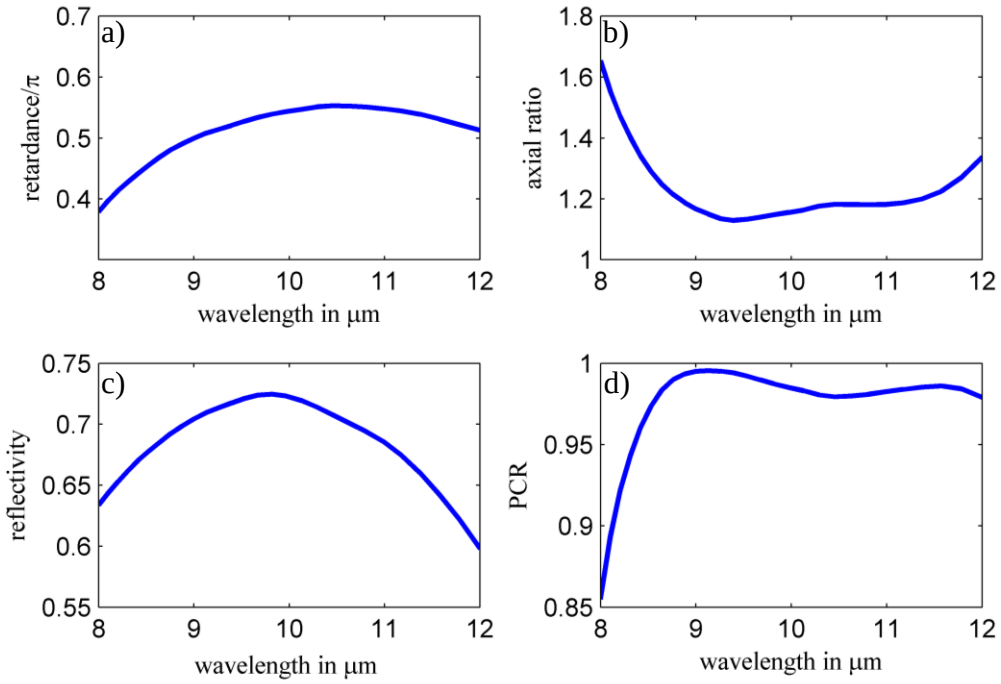

Figure 53: Measured quantities from the IR-VASE, consisting of a) the phase retardance, b) axial ratio, c) average power reflection, and d) polarization conversion ratio.

Comparing the plots of Figures 51 and 53, most of the differences between the model predictions and the experimental data can be attributed to slight differences between the modeled structure and the array elements that were actually fabricated. The SEM image of the meanderline array in Figure 52 shows rounded edges of the element geometry instead of flat rectangular shapes, and the measured linewidths of the corresponding structure indicate that the pattern was slightly over exposed, resulting in enlarged linewidths than designed for by approximately 30%. In addition, it was found that after evaporation, the thickness of the ZnS layer was about 580 nm rather than the design thickness of 650 nm. The measured data seen in Figure 53 demonstrates a reflective meanderline array above a groundplane that produces broadband CP upon reflection of a 45° LP field. The AR is below 2 over the entire LWIR band, and the phase shift is quite achromatic near

the desired π/2 value. Furthermore, the PCR is always above 85%, even at the edges of the band, showing a high-efficiency conversion of LP into CP. Finally, the polarization-averaged reflectivity has a maximum of approximately 72%, which is very close to the outcome of the FEM model. The overall spectral dispersion in the experimental data agrees quite well with the values obtained from the FEM simulations.

In addition to the measurements that were performed at a 45° angle of incidence, the spectral phase shift and AR were also measured over a 20° angular range centered on the 45°-incidence configuration (Figure 54), to gauge the angular sensitivity of the device performance.

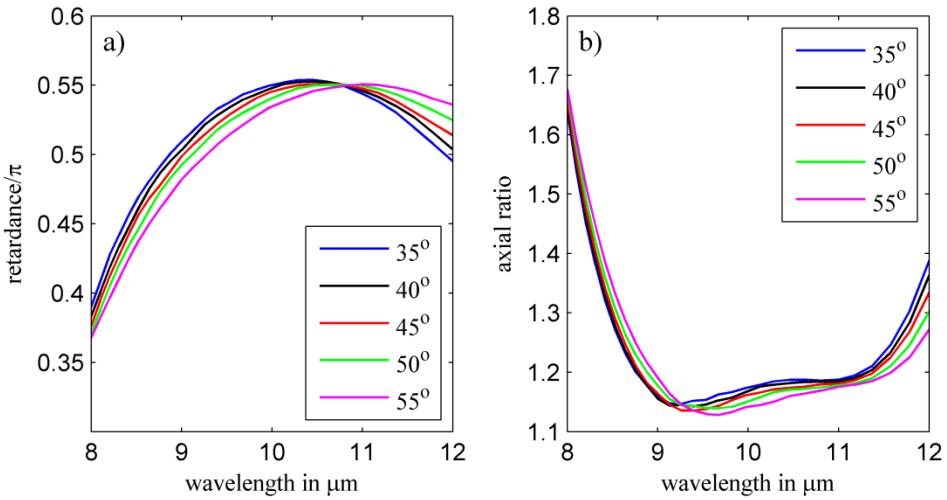

Figure 54: Angular dependence of a) the phase retardance and b) the axial ratio over a 20° span around the optimum 45° angle of incidence.

The reflected state of polarization from the meanderline QWP is very stable with regard to incident angle. This is a beneficial characteristic that would allow the reflective meanderline technology to be incorporated in situations where the radiation is incident over a broad angular range. The device can therefore be inserted into an optical system in non-collimated space, such as in the focusing beam of a polarization-resolved thermal imager. Such applications warrant the

particular design, optimization, and characterization methodologies that were employed for these types of devices in the IR band.

3.3 Applications for Multilayer Meanderline QWPs

The few remaining sections of the current chapter shall detail the work that was performed regarding the design, fabrication, and characterization of multilayer FSS devices that incorporate subwavelength meanderline grid arrays for various polarization-related applications. In particular, we shall demonstrate two specific components that were exclusively fabricated for detection of intensity-based polarization signatures (Stokes parameters), and generation of broadband CP light. The latter device was constructed for MWIR operation, whereas the former was designed for broadband LWIR performance. Both structures were utilized in realistic data acquisition and measurement scenarios, which suitably demonstrate the utilitarian nature and versatility of multilayered meanderline technology for thermal imaging and spectroscopy applications.

3.3.1 Achromatic QWP for Broadband Imaging Polarimetry in the LWIR

Complete reconstruction of the Stokes polarization parameters requires the use of a QWP element in the optical train, as was demonstrated by Equations 8 through 11 in Chapter 1. Moreover, accurate determination of the intensity-based polarization metrics over the LWIR spectrum depends upon the achromaticity and the angle-insensitive behavior of the QWP component used for retrieval of the corresponding Stokes parameters. For these reasons, the 2-

layer design presented in Section 3.1.3 was fabricated over a large square area of a BaF_2 wafer, as shown in part b) of Figure 55.

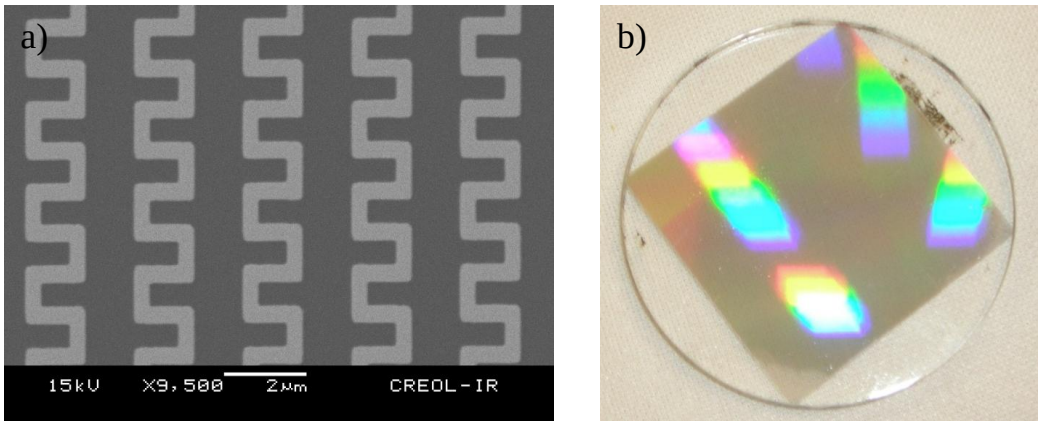

Figure 55: Pictures of a) SEM image of single meanderline layer, and b) macroscopic view of the large-area format 2-layer meanderline QWP device.

The enlarged effective area of the 2-layer meanderline QWP allows for the collection of irradiance over a wide numerical aperture that would be imaged onto a thermal camera's FPA detector. More importantly, the size of the meanderline QWP area does not truncate the signal if placed immediately in front of a wire-grid polarizing element, which is subsequently positioned directly ahead of the focusing optics of a LWIR thermal imager, as Figure 56 demonstrates.

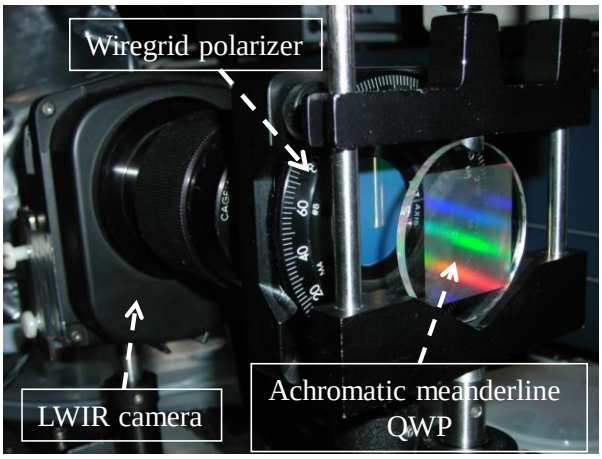

Figure 56: Depiction of polarimetry system with large-aperture 2-layer meanderline QWP in front of a wiregrid polarizer, which is placed directly ahead of the focusing optics of the LWIR thermal camera.

This system configuration constitutes the basic elements for detection of the Stokes vector coefficients [3,8,9], and replicates the setup schematic illustrated in Figure 2 of Chapter 1. The 2-layer meanderline QWP is therefore incorporated into a LWIR thermal polarization-resolved imaging system, its large-area format instrumental for evaluating the retrieved intensity-based polarization signal from a wide angular range of incident radiation that corresponds to a planar two-dimensional scene imaged by the FPA of the thermal camera. The collected irradiance can thus be partitioned into discrete polarization states, and subsequently visualized over the captured image of the planar vista [35,36]. This has significant importance for evaluation of polarized thermal light from ambient scenes and man-made subwavelength structures, and will find particular use in the following section and remaining chapters of this dissertation. The exact methodology for Stokes vector assessment was detailed briefly in the paragraphs adjacent to Equations 8 through 11 of Chapter 1, and will be further expanded upon in the subsequent

chapter, which will present a more comprehensive data acquisition procedure and analysis of intensity-based images and area-averaged polarization metrics from the LWIR polarimetry system shown in Figure 56.

The differential phase retardance, axial ratio, and polarization-averaged transmittance of the 2-layer meanderline QWP were acquired by the IR-VASE system and simulated with HFSS over the LWIR band under normal incidence conditions. Both the experimental and numerical results can be found on the following figures.

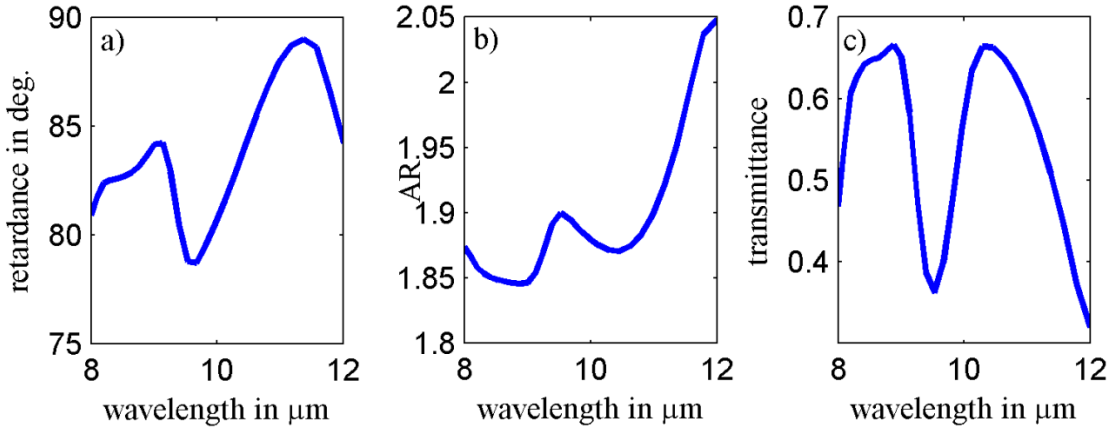

Figure 57: Measured a) phase retardance, b) AR, and c) polarization-averaged transmittance of the large-area format 2-layer meanderline QWP.

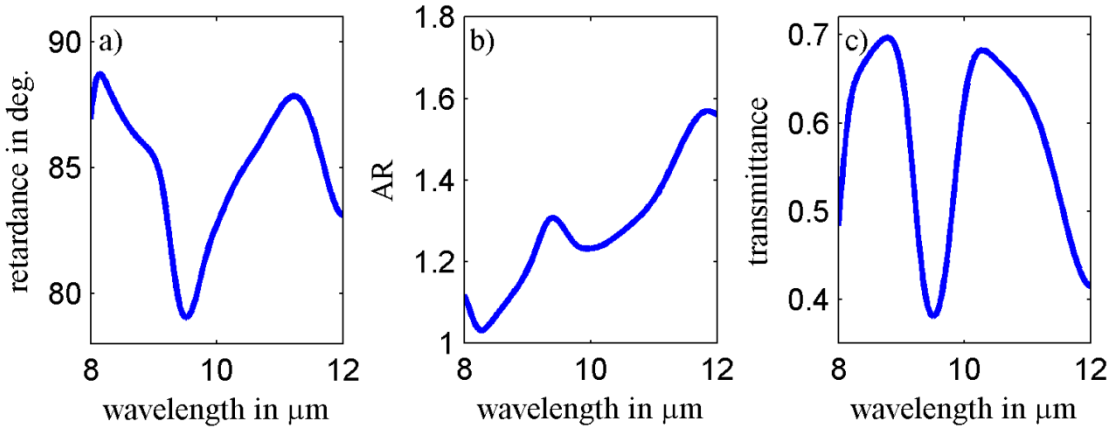

Figure 58: Simulated a) phase retardance, b) AR, and c) transmittance of 2-layer QWP.

Once again, the simulated behavior is extensively validated by the measured parameters, which portray achromatic characteristics for both the differential phase shift and AR. Although the presence of phonon modes in the spectrum of the BCB interlayer dielectric cavity prevents the device from achieving ideal polarimetric QWP values, the conversion from linear to CP is good enough for high-percentage accuracy of the resolved polarization state from an ambient thermal scene. These qualities, along with the angle-insensitive behavior detailed in Section 3.1.5, constitute the necessary requirements for achromatic QWP components that find use in imaging polarimeters, spectrometers, and other systems that operate over a broad spectral range of IR wavelengths.

3.3.2 Circularly-Polarizing Tag in the MWIR

In this section, we present the concept, the design, fabrication, and evaluation of a CP tag that provides a discrete source of broadband CP light throughout the MWIR spectrum. This is inherently useful for testing the multilayered meanderline QWP elements that are incorporated into thermal polarimetry systems, such that the S_3 component of the Stokes vector should be resolved with sufficient clarity given a broadband source of CP. Thus, the CP tag acts as an artificial source of CP light, since CP radiation is seldom occurring in natural ambient scenes [3,8,9]. Therefore, we should theoretically observe a large distinction in contrast between RHCP and LHCP fields, since the background polarization signature mostly consists of unpolarized waves, which can be duly subtracted from the cumulative intensity detected at the FPA. This

forms the basis of the CP tag concept, which employs multilayer meanderline retarders for generation of a spectrally broad CP signature that can be readily discerned via the aforementioned imaging polarimetry methods.

In order to generate CP fields in the IR, a multilayer meanderline QWP can be used in conjunction with a linear wiregrid polarizer, as was demonstrated by Equation 12 of Chapter 1. Rather than have each component as separate entities, the wiregrid polarizer can be directly integrated onto a layer that precedes the meanderline polarizer layers. Thus, CP light is produced from a singular integrated wiregrid polarizer-QWP device, which is schematically shown on Figure 59. Note that the wire orientation is permanently affixed at the 45° angle relative to the fast axis of the meanderline layers.

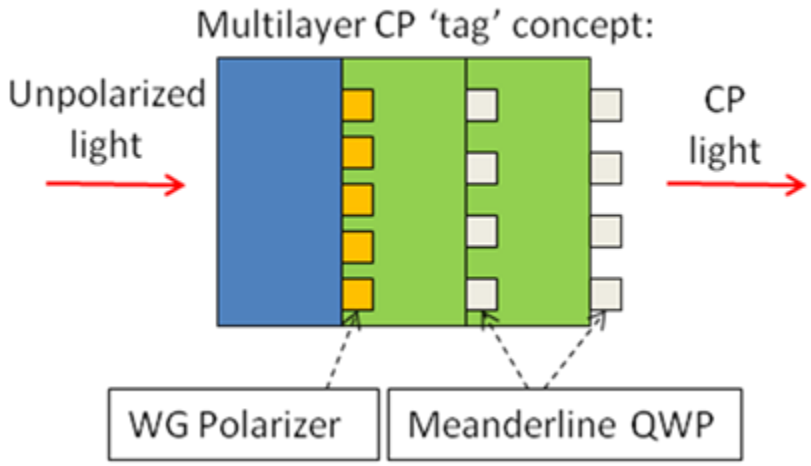

Figure 59: Concept of multilayer filter for generating circular polarization in the IR.

The wiregrid polarizer-meanderline QWP component shall from here onwards be referred to as a CP 'tag', since the compact nature of the layers allows the generation of CP light from any source of randomly polarized IR radiation. Thus, for simultaneous production of both RHCP and LHCP states, one can fabricate the QWP layers in alternating patterns corresponding to the 0°

and 90° orientation of the meanderline fast axis. This concept is displayed on Figure 60, which is only valid for a single orientation of the backing wiregrid polarizer layer.

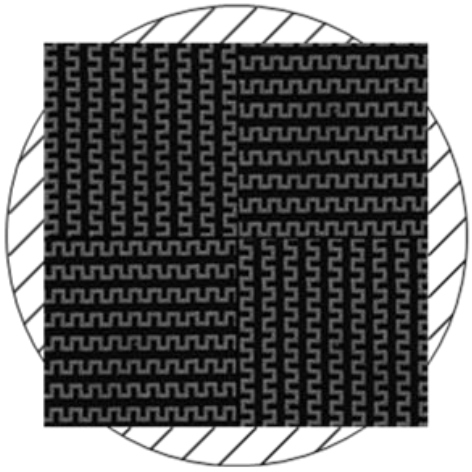

Figure 60: Checkerboard configuration of CP tag. Note that wiregrid polarizer layer is fixed at a 45° angle relative to the entire pattern.

The meanderline checkerboard pattern of Figure 60 was eventually fabricated over a wiregrid polarizer layer, which was patterned on a 4 inch diameter fused silica substrate for MWIR operation. Table 6 lists the materials and dimensions of the meanderline unit cell and the wiregrid array parameters that were applied to the CP tag component. A picture of the finished tag can be seen in Figure 61.

Table 6: Materials and dimensions (in μm) for multilayered CP tag in the MWIR.

Dimensions	lw1	lw2	lw3	DX	DY	pw	ph	t_1	t_2
meanders	0.26	0.26	0.26	0.8	1.35	0.4	0.5		0.64
wiregrid	0.3			0.6				1.3	
Materials	substrate	dielectric	metals						
	SiO_2	BCB	Ti/Au						

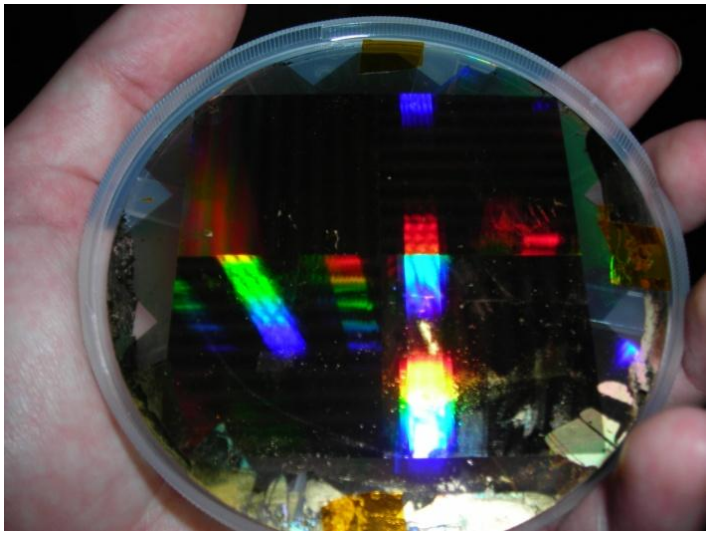

Figure 61: Picture of finalized CP tag for the MWIR.

On the receiving end of the polarimetry imaging system, a multilayer meanderline QWP with the same dimensions listed in Table 6 was inserted before the linear wiregrid polarizer, which was placed in front of the MWIR imaging camera (Mitsubishi IR-5120A). The CP tag component was positioned at a distance down the optical train in front of an active hotplate, which supplies a broad spectrum of unpolarized IR fields. The system schematic and its corresponding image can be located on the following figure.

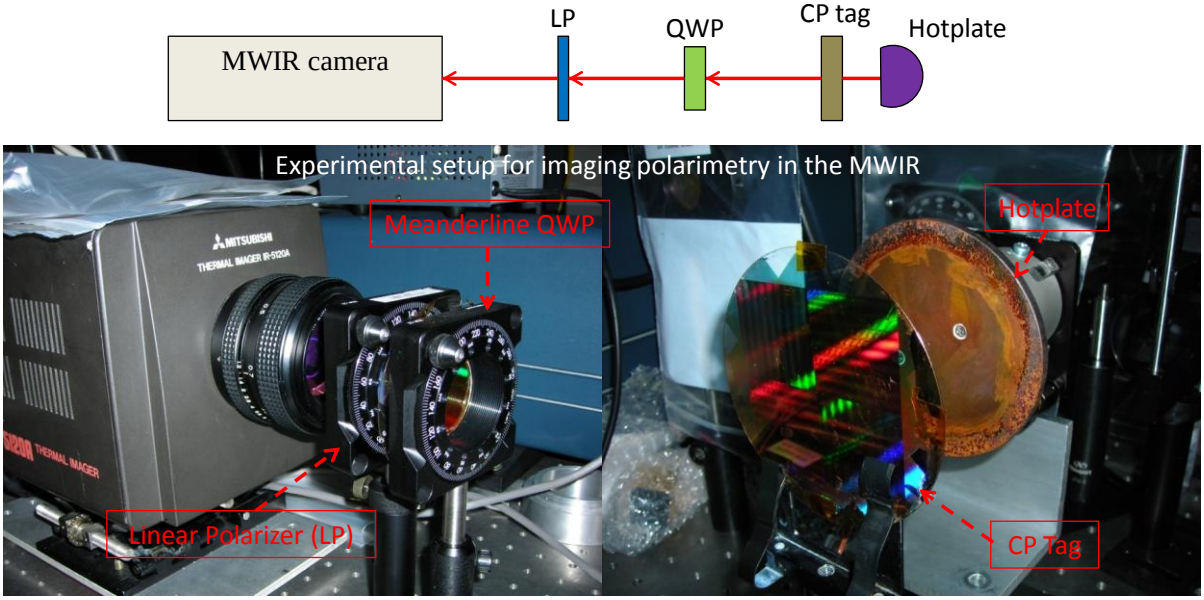

Figure 62: System schematic and experimental setup for polarization imaging in the MWIR.

The subsequent series of images were taken from the MWIR camera while implementing specific arrangements of the imaging polarimetry system. Initially, an image was taken of the CP tag without the analyzing meanderline QWP and linear polarizer in the optical system. Notice that the associated picture in Figure 63 exhibits absolutely no discernable contrast between the patterned regions of the CP tag. This is because the CP radiation that is produced upon transmission through the tag has a uniform intensity distribution across the patterned surface, regardless of the orientation of the meanderline elements. Thus, in order to 'decode' the polarization-based intensity information, analyzing optical components are required.

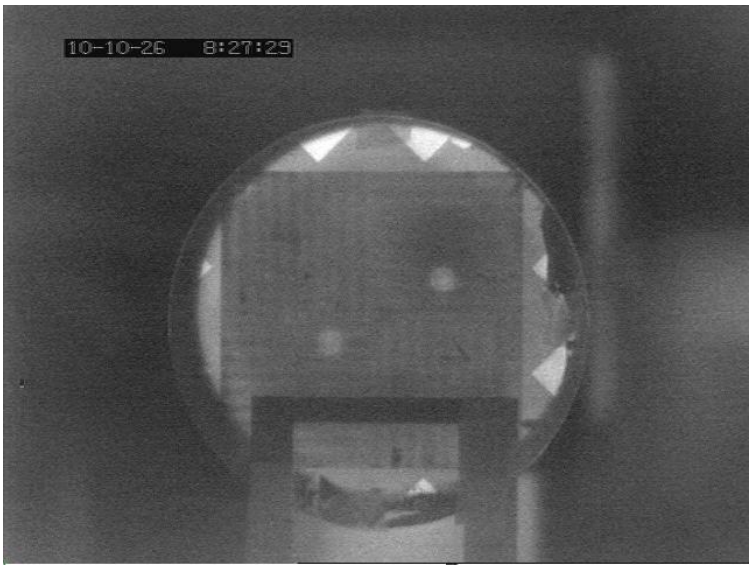

Figure 63: Raw image of CP tag taken without any polarization optics.

The next image shows the same tag as before, but with a linear polarizer in front of the MWIR camera. Although the polarizer was oriented at the ±45° angles, there is still little contrast that is attained from the CP tag structure. However, since the multilayer meanderline QWP checkerboard pattern only takes up a certain region of the 4 inch diameter wafer, the wiregrid polarizer that lies beneath the QWP layers is actually producing a notable modulation in contrast, but only in the places where the QWP elements do not overlap the wiregrid structure. On Figure 64, these would be near the edges of the circular substrate, since the checkerboard pattern produces only RHCP or LHCP light that cannot be solely deciphered by a single linear polarizer. Thus, the lack of intensity distinction from the QWP checkerboard structure is highly indicative of an efficient conversion process that results in transmission of CP light.

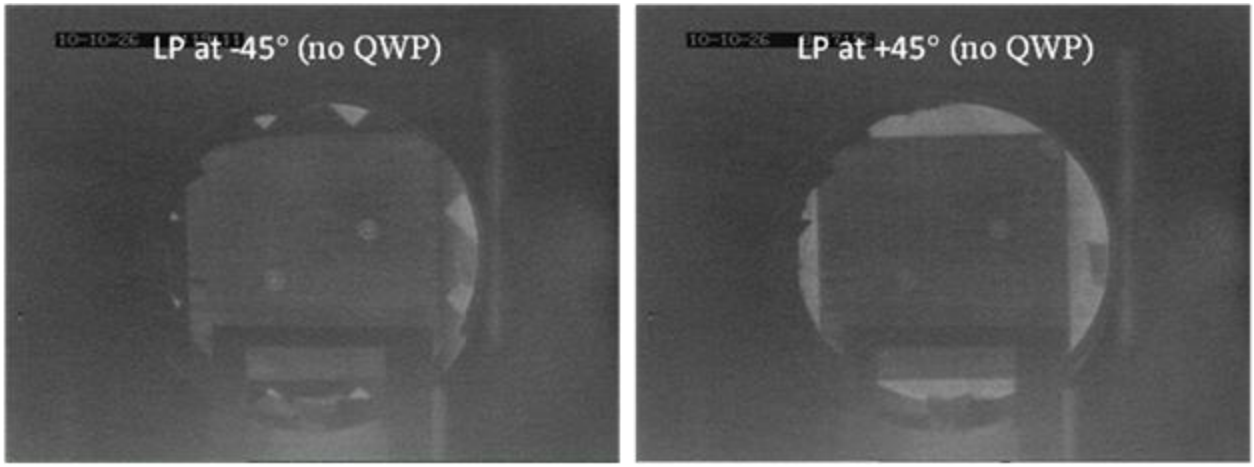

Figure 64: Images of CP tag with only linear polarizer in analysis train.

The final series of images show the CP tag and imaging polarimetry system as it was meant to function. With the meanderline QWP included before the analyzing linear polarizer, as in Figure 62, the rotation of the linear polarizer through the ±45° orientations yields a noticeable change in contrast between the areas of the checkerboard pattern. The bright regions are indicative of a specific handedness of CP radiation that is allowed to pass through the entire system to the FPA detector, while the dark areas imply that the opposite handedness of CP light is being suppressed. This behavior follows directly from the acquisition of polarimetric information indicated by Equations 6 and 11 of Chapter 1, such that orthogonal states of CP are admitted into the polarimetry system only when the transmittance axis of the wire-grid polarizer is rotated to the ±45° positions, which correspond to transmission of either RHCP or LHCP, respectively [3,8]. Hence, the modulation of intensity contrast between the discrete sectors of the checkerboard verifies the 'switching' of the CP handedness that is transmitted through the system. Thus, upon continual rotation of the analyzing polarizer, one would observe a 'blinking' effect such that the

tag were to appear active, but this behavior is merely a symptom of the CP filtering methodology as previously described.

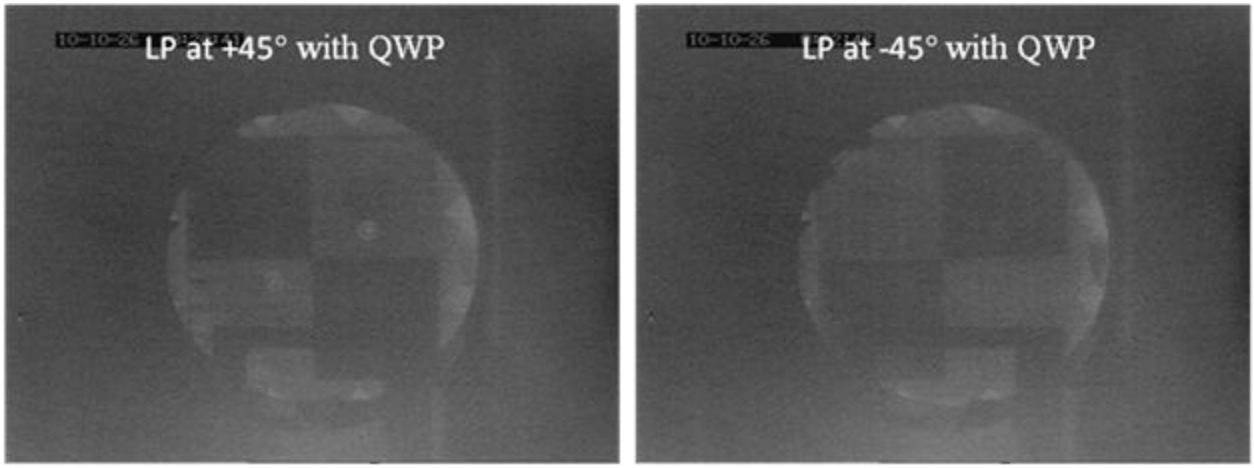

Figure 65: Images of CP tag with meanderline QWP in analysis train, wiregrid polarizer oriented at ±45°. Notice the significant modulation in contrast that indicates switching between RHCP and LHCP transmission.

Additionally, the rotation invariance of CP thermal IR radiation was investigated by simply rotating the CP tag structure while leaving the rotary polarizer fixed at +45°. The subsequent images portray the preservation of contrast on distinct areas of the checkerboard pattern, which signifies that the state of CP light remains unchanged upon physical rotation of the CP-generating elements. This is a fundamental characteristic of all CP fields regardless of source orientation or method of excitation [8,9].

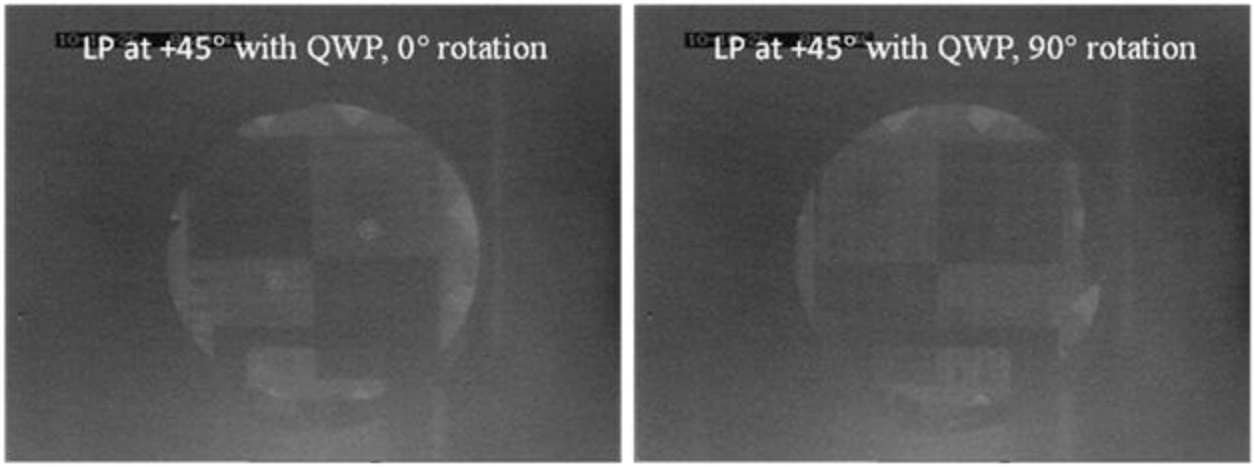

Figure 66: Images of CP tag with wiregrid polarizer held stationary, tag itself rotated by 90°. Contrast rotates with the corresponding areas on the polarizing structure.

Finally, a test was conducted at Northrop Grumman integrated systems in Melbourne, FL for imaging the CP tag at various distances. The following sets of pictures were taken with a HD-VIS-IR camera in the MWIR spectrum, which was mounted on a gimbal platform for potential installation on surveillance aircraft.

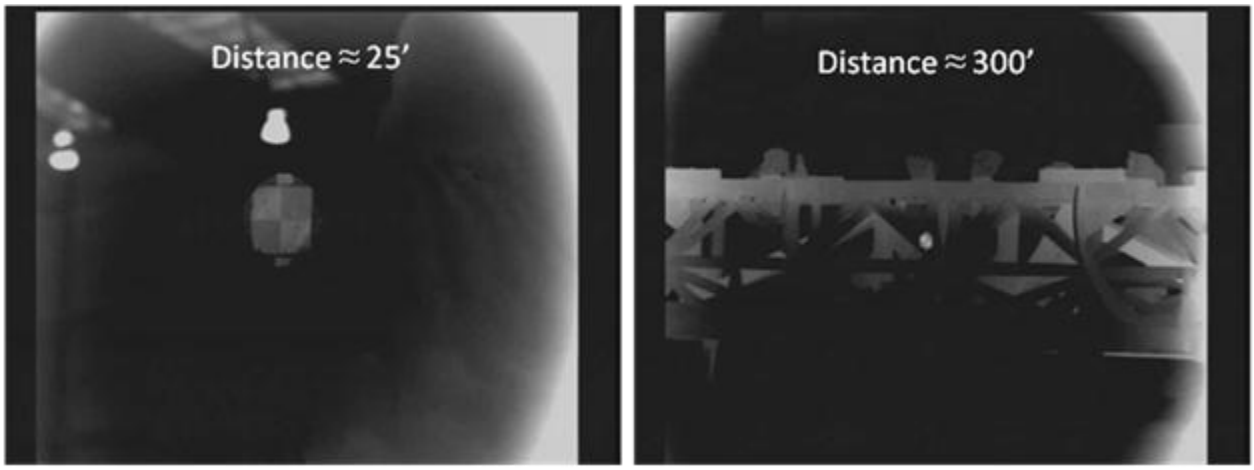

Figure 67: Field testing of CP tag at Northrop Grumman integrated systems.

We can conclude from this salvo of tests that the ability to distinguish the contrast of the tag depends upon the actual size of the pattern, the pixel pitch of the imaging FPA, the displacement from the image sensor to the tag, and the F/# or focal length of the focusing optics.

The operational functionality of meanderline QWPs for broadband imaging polarimetry analysis and tagging has been thoroughly demonstrated. We have shown that efficient conversion of unpolarized light into CP radiation is made possible by the application of multilayer meanderline QWP layers on CP tags. Thus, by physically realizing a CP filtration system, we are able to evaluate the performance of CP tags and analyzing meanderline QWPs over a broad IR spectrum. The results in this section and chapter entire indicate that each corresponding subwavelength structure exhibits broadband achromaticity, which is a suitable confirmation of the effort that went into the design, optimization, and fabrication of all such meanderline wave retarders and related components.

CHAPTER 4: THERMAL EMISSION OF CIRCULAR POLARIZED RADIATION FROM PLANAR PERIODIC MICROSTRUCTURES

4.1 Overview of State-of-the-Art Technology for Polarized Coherent Thermal Emission

In the last few decades or so, there have been an increased number of studies related to the thermal emission properties of microstructured surfaces and multilayered photonic structures [80–84,132–148]. By tailoring the local optical density of states via excitation of coherent surface waves [80,81,132–138], microstructured surfaces are able to possess thermal properties not encountered in nature, such as coherent narrow-band thermal emission and coupling to highly-directional far-field radiation by grating momentum transfer with a coherent surface phonon polariton [80,81,132–136]. The surface wave phonon modes are induced in a polar material, such as silicon carbide (SiC), which supports surface phonons at discrete IR frequencies (11.6 μm for SiC) [81,136,138]. Structured subwavelength gratings and cavities etched into the polar material enable generation of surface wave phonons at normal and oblique incidence [81,136], and allow for thermally-excited surface waves to couple into directional far-field radiation via Kirchhoff's reciprocity principle [149–152]. The directional nature of the radiation is facilitated by the narrow-band characteristics of the grating, which is able to achieve extremely narrow frequency linewidths by coherent interference of surface phonons in the near field [81,133,137,138], and by coupling to resonant cavity modes of the grating structure [136]. An example of a cavity-coupled phonon mode in an emissive grating device is shown below in Figure 68.

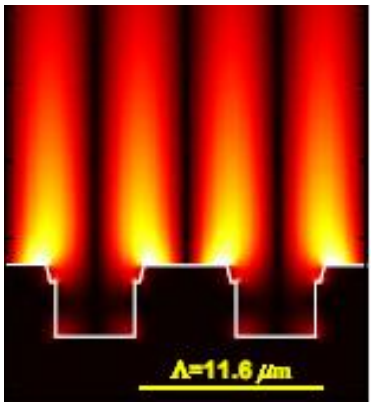

Figure 68: Surface waves coupled to resonant cavity modes of a periodic SiC grating (from [136])

Likewise, multilayered photonic crystal (PhC) structures have also been demonstrated to exhibit control over its thermal emissive properties, when multiple Bragg scattering yields highly-directional, narrow-band thermal radiation [139–142] with significant control over the spectral emissivity [143–145].

With regard to the polarization spectrum of thermally-emitted fields, the aforementioned grating structures have been shown to be highly polarized both in the near and far-field regimes [132,137]. The high degree of linear polarization that is transferred to the far-field zone is indicative of *p* – polarized phonon modes, which are the only coherent surface waves allowed upon thermal excitation of a subwavelength polar grating [80,81,134–136]. Therefore, states of linear polarization can be controlled by the orientation of the grating, and can be applied as a polarization-encoded grating surface for polarimetric imaging scenarios [146]. Multilayer PhCs have also been investigated as discrete polarization-state emitters [82–84], with one such study implicating broadband CP emission via a complete polarization band-gap [82]. In the literature, it is demonstrated that a broadband polarization band-gap requires multiple Bragg scattering of

orthogonal polarization states, such as RHCP and LHCP, which must occur over a specified finite thickness of PhC material in order to generate a high extinction ratio between emitted orthogonal polarized fields [82,147]. Figure 69 depicts a three-dimensional PhC design that exhibits polarization-selective emission behavior, which is controlled by preferential Bragg reflection of CP waves over a designated thickness of material.

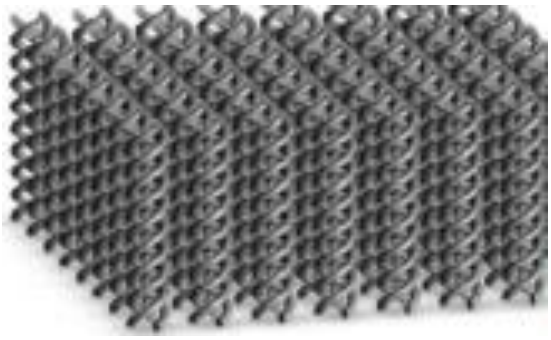

Figure 69: Sample picture of a twisted metallic helical PhC for preferential CP emission (from [147])

Although this technology seems promising, most of the preceding work has been limited to analytical and numerical conjectures, as fabrication of the structures has proven to be exceptionally difficult, especially in the IR regime. Therefore, experimental generation of broadband CP thermal emission has been solely obtained via thermal excitation of a uniaxial anisotropic material, which actually gains its anisotropy from being placed in a magnetic field [85]. Thus, the experimental study of broadband CP emission of thermal radiation is limited to only a few cases, which is somewhat disheartening since circular polarization is rather exotic and cannot be found in a natural IR environment.

4.1.1 Statement of Purpose

Because of the rarity of circular polarization in a thermal ambience, it would be desirable to control the state of polarization of thermally emitted waves and alter the polarization signature such that broadband CP is achieved. Achromatic CP characteristics have already been obtained through electromagnetic scattering from planar periodic meanderline structures in the IR, so it is only natural to extend such efforts to broadband thermal emission of CP radiation. Although this would be useful for many applications, we shall concentrate our efforts on broadband imaging polarimetry, specifically because a broadband thermal source of CP light would allow for objects and targets to be discriminated based upon the emitted state of polarization [8,34–36]. Owing to the fact that circular polarization is seldom found in nature [8,77,79], a CP thermal emission signature would stand out from the background spectrum and be instantly recognizable once imaging polarimetry analysis is applied. This has already been established in the previous chapter with polarimetric imaging of the MWIR CP tag (Figure 61). Thus, with regard to broadband polarimetry, a source of polarized thermal radiation that has a low profile and is easy to fabricate over a broad area constitutes an ideal structure that could modify the polarized emissivity of a planar surface [90,148] and be easily visible by a thermal imaging polarimetry system. A structured surface in the form of a planar periodic FSS represents such a component that could potentially provide polarization-shaping capability for thermally emitted fields. It has already been demonstrated that a planar FSS array of lossy dipole elements, shown on Figure 70, provides a uniform linear-polarized field when thermally excited [148]. In the current chapter,

our aim is similar, such that thermal excitation of a homogeneous CP field shall be attempted from a planar FSS structure that is placed in direct contact with an active blackbody source.

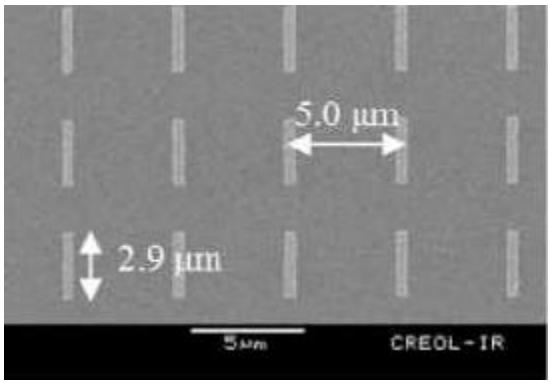

Figure 70: Periodic lossy dipole elements for LP emission (from [148])

4.2 Polarization and Coherence of Thermal Emission from Microstructured Surfaces

The physical process of thermal excitation involves the random motion of electrons within the volume of the microstructure, which in turn radiate electromagnetic fields in the thermal IR spectrum. This is caused by active heating of the structure when placed in direct contact with a blackbody source, which is brought up to an elevated temperature above that of the ambient scene. Thus, thermal conduction is the principle mechanism by which thermally-emitted fields are generated [26,152]. However, it is not so trivial to elicit control upon the polarization state of the emitted radiation, since the random fluctuating motion of electrons and surface current densities are often uncorrelated, thereby resulting in incoherent and unpolarized fields. In fact, most thermal radiation consists of unpolarized waves [77,79], so the nature of thermal field coherence and surface current density correlation must be investigated in order to determine if broadband CP radiation is possible from planar subwavelength microstructures. To

do this, we turn our attention to the statistical description of time-varying electromagnetic wave polarization and coherence of a propagating planar wavefront (Equation 1, Chapter 1).

4.2.1 Equal-Time Coherence Matrix and Mutual Coherence Function of Thermal Electromagnetic Fields

While LP radiation can be produced by the dipole FSS arrangement of [148], configuration of a structure with preferential radiation for CP is much more difficult because transverse coherence between two components of the electromagnetic field is required. To illustrate the coherence characteristics of thermally emitted fields in the IR spectrum, we use the Wolf coherence matrix of a time-dependent electromagnetic field signal

$$W(x,y,t)=\begin{bmatrix}\left\langle E_s(x,y,t)^*\cdot E_s(x,y,t)\right\rangle & \left\langle E_s(x,y,t)^*\cdot E_p(x,y,t)\right\rangle\\ \left\langle E_p(x,y,t)^*\cdot E_s(x,y,t)\right\rangle & \left\langle E_p(x,y,t)^*\cdot E_p(x,y,t)\right\rangle\end{bmatrix}, \tag{63}$$

where the field terms $E_{s,p}$ denote the *s* and *p* – polarized components of the electric-field vector in the plane of the polarization ellipse, '*' denotes complex conjugation, and the brackets $\langle\ \rangle$ denote the ensemble average of the analytic signal taken over a successive series of measurements or time intervals [3,78,133,137,138]. Equation 63 is representative of the time-dependent irradiance that would be detected by broadband imaging methods, since the wavelength dependence is averaged for a broadband imager. Thus, Equation 63 accounts for the information that would be available from images: spatial dependence of the time-averaged irradiance.

Evaluation of the coherence matrix involves the co-polarized and cross-polarized irradiance, since each matrix element is an inner product between amplitudes of the same or orthogonal polarization component. With respect to polarized emissivity, the field amplitude can be taken as proportional the square root of the emissivity corresponding to either the *s*- or *p*-polarized state. Since the field amplitudes are inherently complex, the square root of the polarized emissivity would also be complex in value as well, so that Equation 67 would be written as

$$W(x,y,t)=\begin{bmatrix}\left\langle\sqrt{\varepsilon_s(x,y,t)}^{*}\cdot\sqrt{\varepsilon_s(x,y,t)}\right\rangle & \left\langle\sqrt{\varepsilon_s(x,y,t)}^{*}\cdot\sqrt{\varepsilon_p(x,y,t)}\right\rangle \\ \left\langle\sqrt{\varepsilon_p(x,y,t)}^{*}\cdot\sqrt{\varepsilon_s(x,y,t)}\right\rangle & \left\langle\sqrt{\varepsilon_p(x,y,t)}^{*}\cdot\sqrt{\varepsilon_p(x,y,t)}\right\rangle\end{bmatrix}. \tag{64}$$

Now that we have defined the coherence matrix in terms of polarized emissivities, the Stokes vector of the polarization signal can be formulated from the individual elements of the coherence matrix of Equation 64 [3,8,132].

$$\bar{S}(x,y,t)=\begin{bmatrix}S_0\\S_1\\S_2\\S_3\end{bmatrix}=\begin{bmatrix}\left\langle\sqrt{\varepsilon_s(x,y,t)}^{*}\cdot\sqrt{\varepsilon_s(x,y,t)}\right\rangle+\left\langle\sqrt{\varepsilon_p(x,y,t)}^{*}\cdot\sqrt{\varepsilon_p(x,y,t)}\right\rangle\\ \left\langle\sqrt{\varepsilon_s(x,y,t)}^{*}\cdot\sqrt{\varepsilon_s(x,y,t)}\right\rangle-\left\langle\sqrt{\varepsilon_p(x,y,t)}^{*}\cdot\sqrt{\varepsilon_p(x,y,t)}\right\rangle\\ \left\langle\sqrt{\varepsilon_s(x,y,t)}^{*}\cdot\sqrt{\varepsilon_p(x,y,t)}\right\rangle+\left\langle\sqrt{\varepsilon_p(x,y,t)}^{*}\cdot\sqrt{\varepsilon_s(x,y,t)}\right\rangle\\ i\cdot\left(\left\langle\sqrt{\varepsilon_p(x,y,t)}^{*}\cdot\sqrt{\varepsilon_s(x,y,t)}\right\rangle-\left\langle\sqrt{\varepsilon_s(x,y,t)}^{*}\cdot\sqrt{\varepsilon_p(x,y,t)}\right\rangle\right)\end{bmatrix}, \tag{65}$$

where the above formula can be re-written as (the dependence upon (*x*,*y*,*t*) is assumed)

$$\bar{S} = \begin{bmatrix} S_0 \\ S_1 \\ S_2 \\ S_3 \end{bmatrix} = \begin{bmatrix} \langle \varepsilon_s \rangle + \langle \varepsilon_p \rangle \\ \langle \varepsilon_s \rangle - \langle \varepsilon_p \rangle \\ 2 \cdot \left\langle \sqrt{\varepsilon_s \cdot \varepsilon_p} \cdot \cos(\delta) \right\rangle \\ 2 \cdot \left\langle \sqrt{\varepsilon_s \cdot \varepsilon_p} \cdot \sin(\delta) \right\rangle \end{bmatrix} = \begin{bmatrix} \langle \varepsilon_s \rangle + \langle \varepsilon_p \rangle \\ \langle \varepsilon_s \rangle - \langle \varepsilon_p \rangle \\ \langle \varepsilon_{+45^\circ} \rangle - \langle \varepsilon_{-45^\circ} \rangle \\ \langle \varepsilon_{RHCP} \rangle - \langle \varepsilon_{LHCP} \rangle \end{bmatrix}, \tag{66}$$

with the variable δ as the phase shift between the two orthogonal components of the polarized emissivity. The Stokes vector gives a direct physical interpretation of the state of polarization of a given electromagnetic field. In each element of the Stokes vector, the irradiance associated with a particular state of polarization is quantified by the measured difference between orthogonal polarization states [3,8,9]. Since we are working with polarized emissivity, we can express the Stokes vector components in terms of the emissivity corresponding to each measured polarization state, as shown in Equation 66.

We have so far conveyed the state of polarization of thermally emitted fields in terms of the coherence matrix and Stokes vector elements, but without any mention of the degree of coherence that must exist for manifestation of cross-polarization. Cross-polarization refers to cross-polarized states of the electromagnetic field vector that require non-zero correlation between cross-polarized components [3,78]. Thus, with reference to Equations 64 through 66, the cross-polarized states would be defined as ±45° linear and/or right-handed/left-handed circularly polarized (RHCP/LHCP) radiation, which are given as S_2 and S_3, respectively. Both off-diagonal components of the coherence tensor (Equation 64) are utilized in the expressions for S_2 and S_3, so there must be some degree of correlation between orthogonal components in order for ±45° LP and RHCP/LHCP waves to exist [3,8,78]. This necessity for correlation between

cross-polarized components can be summarized by the normalized coherence function between cross-polarized states:

$$j_{sp} = \frac{\left\langle \sqrt{\varepsilon_s(x,y,t)}^{*} \cdot \sqrt{\varepsilon_p(x,y,t)} \right\rangle}{\left\langle \sqrt{\varepsilon_s(x,y,t)}^{*} \cdot \sqrt{\varepsilon_s(x,y,t)} \right\rangle^{1/2} \cdot \left\langle \sqrt{\varepsilon_p(x,y,t)}^{*} \cdot \sqrt{\varepsilon_p(x,y,t)} \right\rangle^{1/2}}. \tag{67}$$

If the value given by Equation 67 is non-zero and imaginary, then there will be some finite CP component in the resultant Stokes vector of the thermally emitted field. Thus, the correlation of cross-polarized field components is absolutely necessary for achieving CP emission.

4.2.2 The Fluctuation Dissipation Theorem and Spectral Properties of Thermal Fields

Radiative emission from a structure that is thermally excited can be thought of as a stochastic process by which the current density on the surface of the structure takes on random magnitudes, phases, and directions at each instance of excitation [2,26,151,152]. Thus, to portray the electromagnetic fields that arise from thermal excitation, one has to consider the fluctuational electrodynamics of the problem. In the case of polarized thermal emission from a planar periodic FSS, the elements of the coherence matrix of Equation 64 can be fully determined from the Fluctuation-Dissipation Theorem (FDT) [2,26,133,137,138,152–154]. The FDT was used to analytically verify the extreme narrowband coherent emission behavior of surface-relief gratings that support *p*-polarized surface-wave modes [80,81,132,133,137,138,154]. This was done by computing the correlation moment of the current density components,

$$\left\langle j_m^{*}(\vec{r}_1,\omega) \cdot j_n(\vec{r}_2,\omega') \right\rangle = \frac{\omega}{\pi}\varepsilon_0\varepsilon_r''(\omega)\Theta(\omega,\mathrm{T})\delta(\vec{r}_2-\vec{r}_1)\delta_{m,n}\delta(\omega-\omega'), \tag{68}$$

which is brought about by causality of the material response function, and by direct application of the FDT to the covariance of the system's electric dipole moment [26,133,137,138,154]. Ultimately, the FDT is the result of statistical mechanics that describes the correlation properties of fluctuating thermal currents and fields [2,26,152]. In the above expression, *m* and *n* refer to the spatial indices of current density vector (in other words, *m* and *n* could be *x*, *y*, or *z*), and the function $\Theta(\omega, \mathrm{T})$ is the average energy of the quantum harmonic oscillator at temperature T, which is given as

$$\Theta(\omega, \mathrm{T}) = \frac{\hbar\omega}{\exp(\hbar\omega / k_B \mathrm{T}) - 1} + \frac{\hbar\omega}{2}, \tag{69}$$

where the last term is the zero-point energy of vacuum [26,133,137,138,154]. By employing the integral equation method with Green's function [133,137,138,154], the spatial electric field correlations could be directly evaluated from Equation 68, with a simple Fourier transform resulting in the same exact elements as the time-domain coherence matrix of Equation 63 [3,26,133,154].

As indicated by the series of delta functions in Equation 68, the implications of the FDT are not favorable for broadband CP emission. First of all, the FDT negates any cross-correlation of field components, even over finite-dimension geometries [153] of the FSS unit cell. This is equivalent to saying that the normalized coherence function of Equation 67 will always result in a value of 0, since orthogonal current modes from random thermal excitations will be completely uncorrelated in phase [2,26,133,137,138,152–154]. The delta function $\delta_{m,n}$ of Equation 68 gives this exact result, since the spatial indices *m* and *n* directly correspond to orthogonal components of the current density elements and emitted field polarizations.

It should be mentioned that the FDT yields the delta function $\delta_{m,n}$ and the imaginary part of the dielectric function, $\varepsilon_r''(\omega)$, when applied to the correlation moments of an isotropic material system [2,26,152–154]. Therefore, there is no intrinsic anisotropy in the planar FSS structure that would allow for CP emission to occur. Since the dimensions associated with the thermal-excitation process are within the electron-scattering length, the associated anisotropy would be required to exist within that same length scale, which is approximately the Fermi electron wavelength of the radiating material [154]. Thus, the FDT results in zero correlation between orthogonal current and field modes, even for finite subwavelength structures.

For any structure that emits broadband radiation, the transverse coherence length becomes inherently smaller as the span of operational frequencies becomes larger [3,26,81,154]. This is a consequence of the Wiener-Khinchin theorem and Fourier transform laws of the mutual coherence function of a thermal electromagnetic field. As one expands the spectral domain considered, the respective correlation length must decrease [3,78]. Thus, from a theoretical standpoint it appears that CP thermal emission from a purely planar FSS is not allowed. However, in the following sections, we will consider a design of a multilayer FSS structure that is able to avoid these constraints and provide a significant amount of broadband CP radiation in the IR.

4.3 FSS Designs for Investigating Broadband CP Emission

Considering the fundamental limitations imposed by the FDT on the functionality of thermally emissive CP FSS arrays, our goal for the investigation of FSS designs is two-fold: 1)

experimentally demonstrate the implications of the FDT with regard to CP emission, and 2) design a multilayer FSS that avoids the constraints of the FDT, and emits significant broadband CP radiation. We choose the wavelength range of interest as the 8–12 μm LWIR band.

4.3.1 L-Shaped Wedge and Circular Spiral Element FSS Arrays

The first set of devices was designed in the ANSYS HFSS full-wave FEM solver that models FSS structures through the use of Floquet ports [112–114]. We investigated two planar FSS designs that were simulated and fabricated to test and demonstrate the implications of the FDT. Figure 71 a) and b) illustrate the unit cells for both FSS designs. Each FSS was comprised of Titanium (Ti) elements modeled on top of a 1.2-μm thick layer of BCB, on a reflective Al groundplane (Figure 71 c).

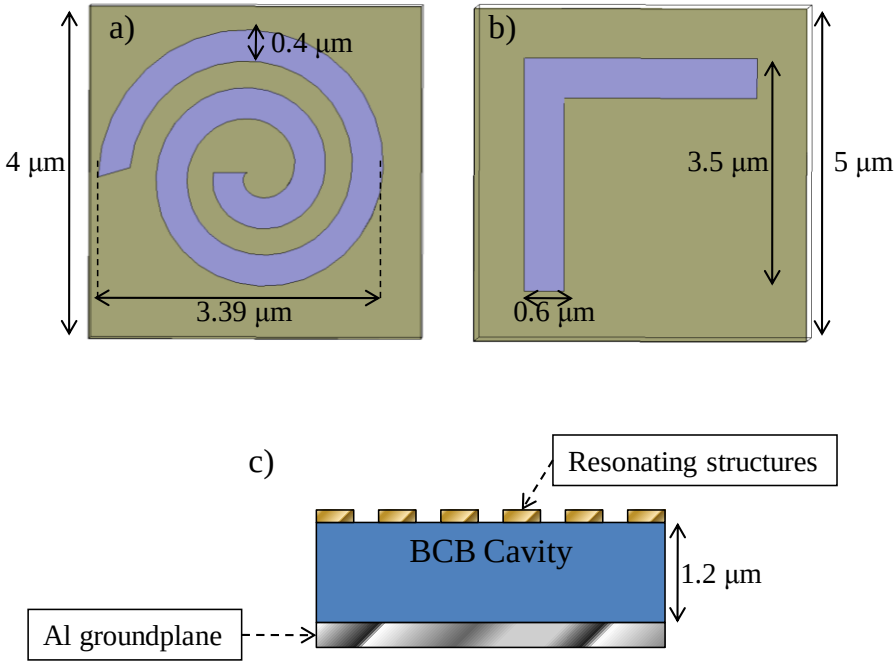

Figure 71: Unit cell profiles of a) circular spiral array, and b) L-shaped wedge array. Below c) is a cross-sectional profile of the emissive structures as simulated in HFSS.

The polarized emissivity from both designs was computed by calculating the power reflection coefficient at normal incidence, using Kirchhoff's law to determine the emissivity corresponding to each polarization state [149–152]. The spectral emissivity for a purely reflective structure is given as

$$\varepsilon(\lambda, \mathrm{T}) = A(\lambda, \mathrm{T}) = 1 - R(\lambda, \mathrm{T}), \tag{70}$$

where T is the temperature in Kelvin of the emissive material. To obtain the polarization components of the Stokes vector, given by Equation 66, the polarized emissivity coefficients are determined as

$$\varepsilon_{s,p} = 1 - R_{s,p}, \tag{71}$$

$$\varepsilon_{\pm 45^\circ} = 1 - R_{\pm 45^\circ}, \tag{72}$$

$$\varepsilon_{RHCP,LHCP} = 1 - R_{RHCP,LHCP}\,. \tag{73}$$

Once these are obtained, the Stokes vector components are readily available via direct insertion of the above expressions into Equation 66. Figure 72 illustrates the simulated Stokes parameters that were calculated by HFSS for the planar FSS designs shown in Figure 71.

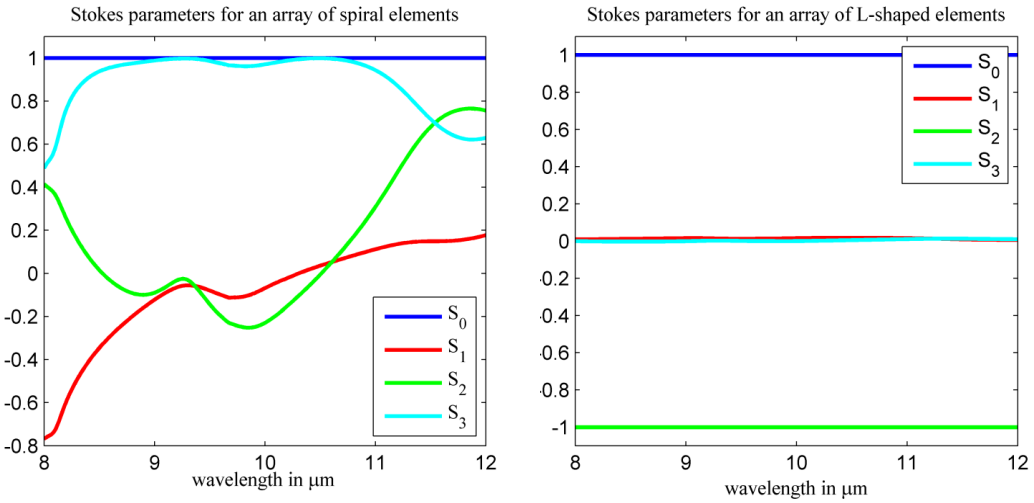

Figure 72: Simulated Stokes parameters of the thermally-emitted field for each design in Figure 71.

Simulation by HFSS does not account for fluctuational electrodynamics, and assumes absolute correlation between orthogonal field components of the thermally emitted radiation, which is contrary to the FDT even for the subwavelength geometries of the proposed designs in Figure 71. With this assumed coherence, Figure 72 shows that the spiral elements reveal a high degree of RHCP indicated by the near-unity value of S_3, whereas the L-shaped wedge elements emit a broad spectral signature of -45° linear-polarized radiation ($S_2 = -1$). We will see in the measurements of these structures that the assumptions of the FDT are verified, and this polarization behavior is not observed experimentally.

4.3.2 Multilayer Subwavelength Structure with Meanderline Array and Thermal Isolation Layer of Silica Aerogel

To design a structure that can emit CP radiation in spite of the constraints imposed by the FDT, we begin with a wire-grid polarizer in contact with the thermal source. We have previously demonstrated [148] that such a structure emits primarily LP radiation when thermally excited. This LP characteristic does not require any cross-polarized coherence, and thus does not contradict the FDT. As shown in Figure 73, there is a dielectric standoff layer between this grid and a meanderline layer [86,98–100], which is designed to give quarter-wave plate (QWP) behavior. The grid and the meanderline layer are oriented at 45°. The meanderline FSS generates CP radiation in transmission by splitting equal components of 45° LP radiation, and imposing a 90° phase shift between the two orthogonal field components.

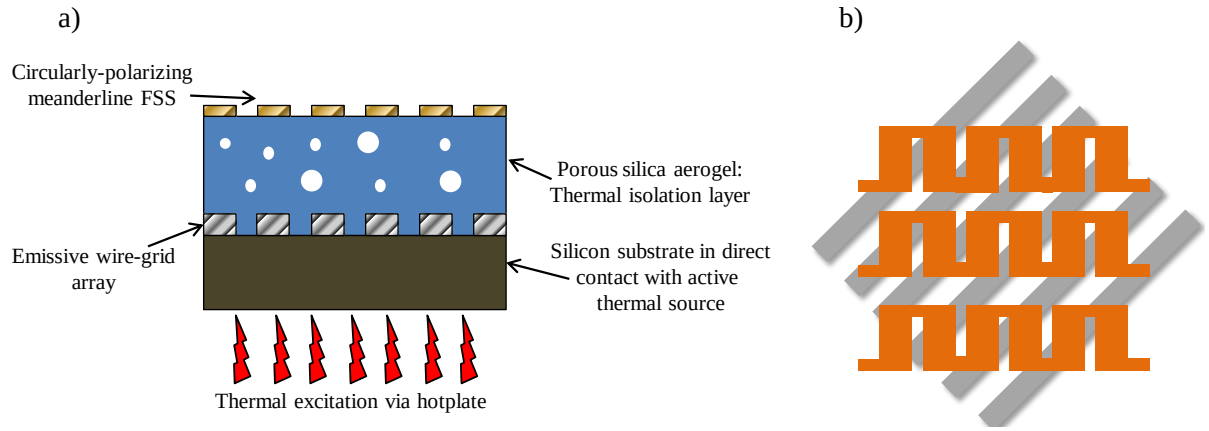

Figure 73: Depiction of a) cross-sectional profile of multilayer structure for generating CP thermal light. The silicon substrate is heated by an active thermal source (hotplate), which generates a linear-polarized signature upon thermal excitation of the wire-grid array. The wire-grid array (in grey) is rotated by 45°, as shown in b), so that the CP meanderline FSS structure (in orange) is able to generate circular polarization upon transmission of the 45°-tilted linear polarized emission. The aerogel helps to thermally isolate the CP meanderline layers from the effects of thermal conduction, and subsequently the consequences of the FDT.

We use a silica aerogel as the dielectric layer. This is a porous material with extremely low thermal conductivity [155–157], which acts as a thermal barrier between the active thermal source and the top layer of metal comprising the meanderline. The reason for this is to maintain a steady-state temperature difference between the thermal source and the meanderline layer. We have observed that meanderline structures have a strong LP component of thermal emission, polarized along the long direction of the wires. Thus, measurements will show both CP and LP emission. To emphasize the CP emission that is transmitted by the meanderline, it is desirable to lower the temperature of the top layer compared to that of the wire grid.

4.4 Emissive FSS Element Fabrication

The FSS elements depicted in Figure 71 were fabricated on a dielectric standoff layer of BCB above a reflective metallic Al groundplane. Initially, the Al groundplane layer was deposited on the polished side of a single-sided-polished (SSP) Si wafer. Afterwards, a coating of BCB [121] totaling 1.2 μm in thickness was spun on and cured on top of the Al groundplane. The Ti-metal resonant elements seen in Figure 74 were written using the Leica EBPG 5000+ e-beam lithography system (Figure 23), and finished with a liftoff process.

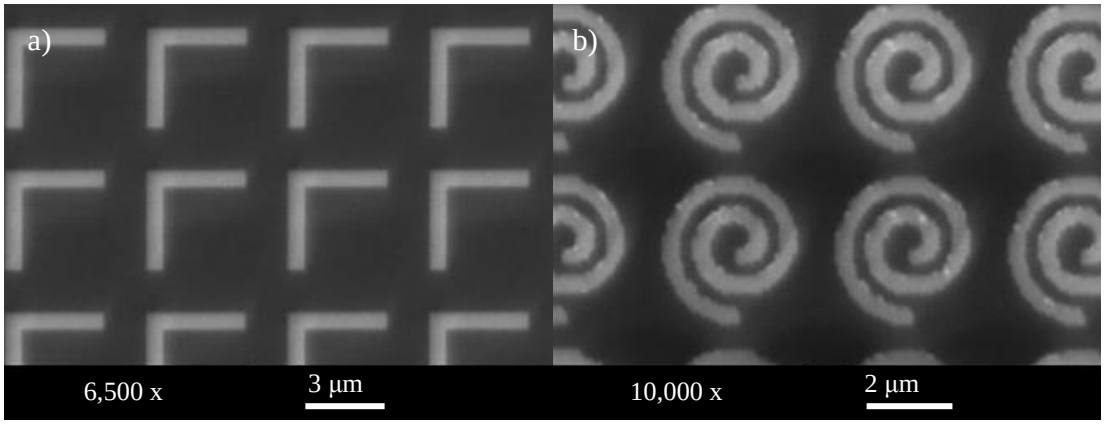

Figure 74: SEM images of fabricated planar periodic FSS structures corresponding to a) L-shaped wedge elements, and b) circular spiral elements.

The structure shown in Figure 73 was fabricated in a similar fashion. As before, a plasma-cleaned SSP Si wafer was utilized for the fabrication of the entire structure, with the linear-polarized emissive wire-grid array elements being directly patterned and metalized with Al on the polished side of the Si wafer. The wire elements were exposed with a 0.5 μm linewidth and an array pitch of 1 μm. Afterwards, the aerogel layer was deposited on to the patterned wire-grid surface by using a layer-by-layer spin-coating technique. The silica aerogel formula was of quite low viscosity, necessitating multiple 1500-rpm spin-coating steps to deposit the required thickness of aerogel, which was around 1 μm. The stack was subsequently baked at 120° C for 10 minutes to drive out the ethanol solvent, leaving the porous silica-aerogel film. To cap and planarize the resulting porous surface, a layer of BCB approximately 350 nm thick was spun on to the aerogel film, and cured. As shown schematically in Figure 75, the BCB penetrates into the surface of the silica aerogel, but then prohibits any further flow into the aerogel film. This procedure provided a surface suitable for the lithographic steps required to fabricate the meanderline elements on top of the BCB capping layer.

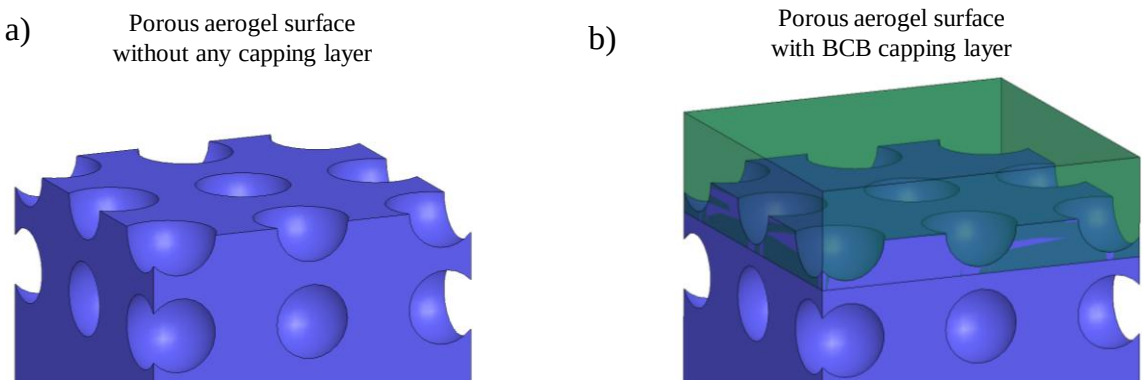

Figure 75: Schematic of a) porous silica aerogel surface without any capping layer, and b) aerogel surface with a layer of BCB that effectively caps the aerogel film and planarizes the surface.

The dimensions of the single-layer Al meanderline structure are given as annotations on the SEM micrograph, Figure 76. Although two or more meanderline layers could have been used to provide better CP transmission [86], we found it difficult to fabricate more than one layer on top of the aerogel film. This was caused by a tendency toward surface cracking upon deposition of any successive dielectric films or metalized layers.

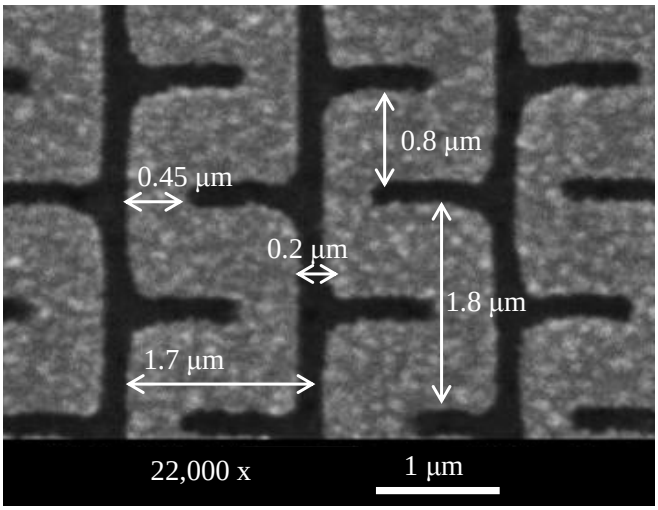

Figure 76: SEM micrograph of meanderline FSS QWP layer with corresponding array dimensions. The elements were fabricated via e-beam lithography and patterned with metallic Al.

4.5 Characterization and Analysis of Emissive FSS Structures

4.5.1 Broadband Polarimetric Characterization

The fabricated FSSs were then characterized using broadband imaging polarimetry. This technique serves to filter particular states of polarization through specific combinations and orientations of analyzing polarizers and quarter-wave plate optical components [8,34–36], as discussed in Sections 1.2.2 and 3.3 of Chapters 1 and 3, respectively. The main objective of such methods is to directly image the state of polarization on the FPA of an 8–12 μm camera (EMX uncooled LWIR imager, model # 01031), thus analyzing the detected irradiance into components associated with a given state of polarization. The setup for this polarization-based imaging (Figure 77) is similar to a configuration for measuring the Stokes parameters (Figure 2), with the proviso that the polarization components must be broadband, consistent with the spectral bandwidth of the camera. Notice that the large-area format multilayer meanderline QWP of Section 3.3.1 is included in this polarimetry analysis system.

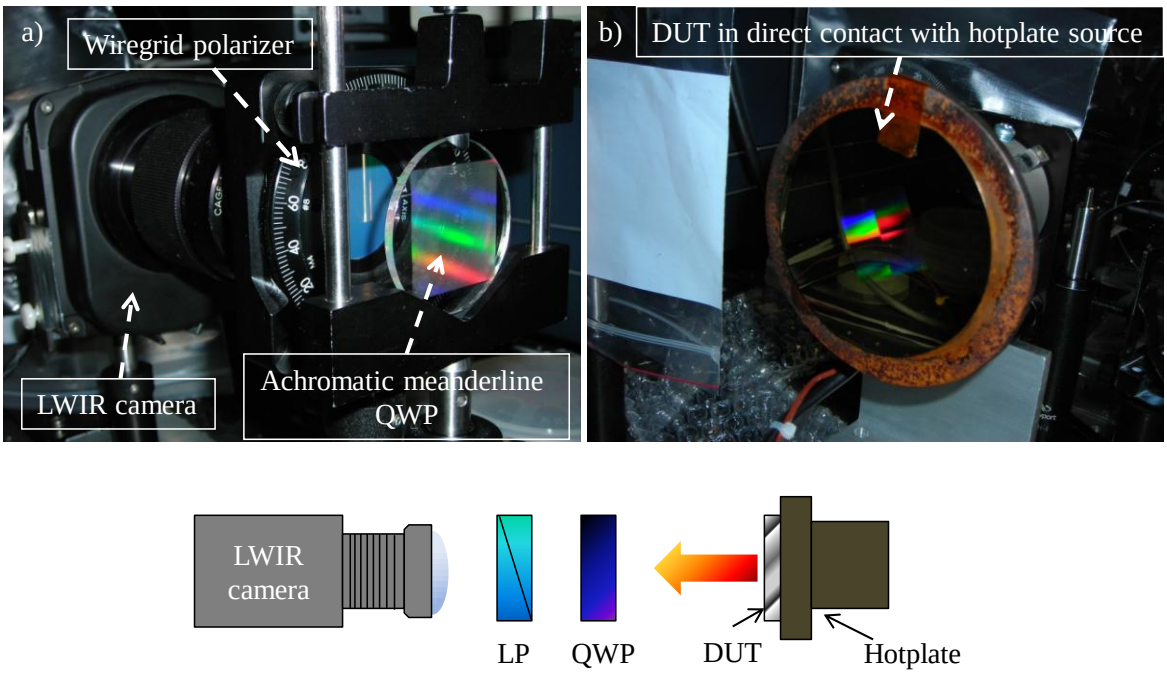

Figure 77: Broadband imaging polarimetry setup with a) LWIR camera and polarization optics, and b) device under test (DUT) in direct contact with hotplate. The schematic represents the polarimetric system with the wire-grid linear polarizer (LP) and achromatic meanderline quarter-wave plate (QWP) as the analyzing polarization components.

It should be mentioned that the device under test (DUT) in part b) of Figure 77 was placed in direct contact with the active hotplate source, thereby achieving the desired configuration of conductive thermal excitation. The hotplate was brought up to a temperature of 45° C, which was enough to thermally excite the planar periodic FSS arrays and image the emitted fields with the LWIR camera. The heated DUT was imaged through the polarization optics of part a), including the achromatic multilayer meanderline QWP [86], such that the polarization-specific components were detected by the camera's FPA. Discrete states of polarization were isolated by rotating the wire grid linear polarizer through specific angles, while the meanderline QWP was inserted and removed from the system for switching between S_3 and

S_2-based polarization imaging, respectively. A series of images was taken for each combination of linear polarizer angle and insertion of the broadband achromatic QWP, with the total combined image information being translated into each component of the Stokes vector [3,8]:

$$S_0 = I(\theta = 0^\circ, \varphi = 0) + I(\theta = 90^\circ, \varphi = 0) \tag{74}$$

$$S_1 = I(\theta = 0^\circ, \varphi = 0) - I(\theta = 90^\circ, \varphi = 0) \tag{75}$$

$$S_2 = I(\theta = 45^\circ, \varphi = 0) - I(\theta = 135^\circ, \varphi = 0) \tag{76}$$

$$S_3 = (I(\theta = 45^\circ, \varphi = \pi/2) - I(\theta = 135^\circ, \varphi = \pi/2))/a^2 \tag{77}$$

In the previous formulas, θ is the angle of the analyzing linear polarizer, $\varphi = \pi/2$ is indicative of the insertion of the achromatic QWP that provides a $\pi/2$ phase shift upon transmission, and a^2 is the attenuation of the beam as it passes through the meanderline QWP component. The QWP device was inserted into the polarimetric system for imaging of S_3 only, so an appropriate attenuation constant needed to be introduced to account for the absorption of IR radiation as it passed through the lossy meanderline QWP. These preceding formulas, which are almost exact replicas of Equations 8 through 11, were used to analyze the image information and ultimately produce an area-averaged Stokes vector component of the thermally emitted electromagnetic fields from the subwavelength FSS structures. The following section will detail this intensity-based polarization analysis procedure, along with the results that were acquired from evaluation of the images taken from the broadband polarimetry system.

4.5.2 Image Analysis

The image-analysis methodology employed for measurement of the Stokes vector components is illustrated in Figure 78. The outlined box with the corresponding title of ‘noise’ represents the area of the image that was averaged based upon the numerical equivalent of the gray-scale intensity, with 0 being the lowest value, and 255 as the maximum. This baseline noise value was averaged over all successive images corresponding to each irradiance-based measurement of the Stokes parameters given by Equations 74 through 77. There were a total of 6 images taken for a series of Stokes vector coefficients, with each image having its average noise value subtracted from the entire matrix of numerical gray-scale irradiance information.

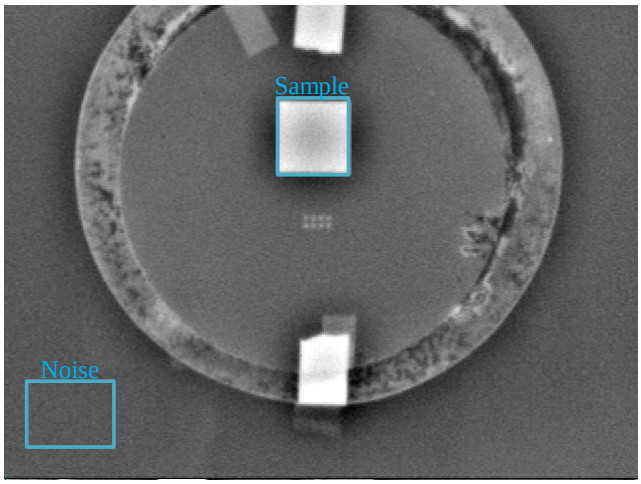

Figure 78: Example image taken from polarimetric system with annotated boxes outlining the areas that were selected for noise averaging and the sample area.

The second outlined box with the title of ‘sample’ in Figure 78 indicates the sample area of the planar periodic FSS structure that was evaluated. As shown in Figure 79, the resulting numerical gray-scale irradiance values after noise subtraction vary somewhat over the area of the sample. Thus, the entire sample area was averaged to yield a single value that represented the average

gray-scale irradiance of the received signal over the FSS area. This averaged intensity was computed for each of the 6 images that were taken for complete determination of the Stokes vector components.

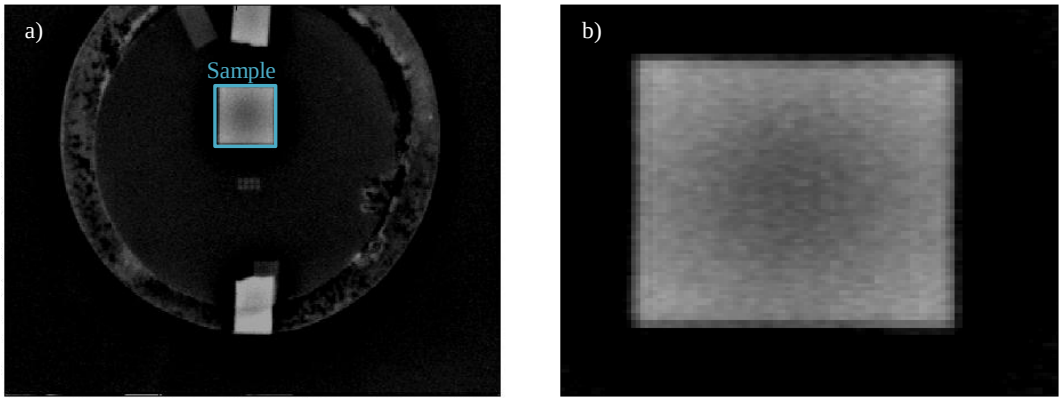

Figure 79: Same image as Figure 78, but with the baseline noise subtracted from the data. Part a) shows the sample area as before, with part b) as a zoomed-in image of the planar FSS area. Note the variation in local intensity of the thermally emitted fields over the area of the FSS.

Upon evaluation of the percent transmission through the achromatic meanderline QWP [ref], which yields the attenuation constant a^2, the normalized Stokes vector was obtained by inserting the appropriate area-averaged gray-scale intensities into Equations 74 through 77 and dividing each coefficient by S_0 [8]. This procedure was followed for each FSS device measured.

We will present our measured results in terms of the total degree of polarization (DOP), total degree of unpolarized radiation (DOUP), the total degree of linear polarization (DOLP), and the total degree of circular polarization (DOCP). In terms of the Stokes parameters of Equations 74–77, these quantities are defined as [8,9]:

$$DOP = \sqrt{S_1^2 + S_2^2 + S_3^2} \Big/ S_0 \tag{78}$$

$$DOCP = \left| S_3 / S_0 \right| \tag{79}$$

$$DOLP = \sqrt{DOP^2 - DOCP^2} = \sqrt{S_1^2 + S_2^2} \Big/ S_0 \tag{80}$$

$$DOUP = \sqrt{1 - DOP^2} \,. \tag{81}$$

Alternatively, the DOCP given by Equation 79 can be completely described in terms of images taken with the analyzing polarizer at the 45° and 135° angles, and with the achromatic multilayered meanderline QWP inserted into the system. In this way, the attenuation coefficient a^2 does not need to be taken into account, since the total normalized *DOCP* is evaluated with respect to the total intensity that passes through the linear polarizer and meanderline QWP components.

$$DOCP = \left| \frac{(I(\theta = 45^\circ, \varphi = \pi/2) - I(\theta = 135^\circ, \varphi = \pi/2))}{(I(\theta = 45^\circ, \varphi = \pi/2) + I(\theta = 135^\circ, \varphi = \pi/2))} \right| \tag{82}$$

This alternate expression for the *DOCP* was used in our computation of results.

4.5.3 Measurement Results

The normalized area-averaged Stokes vector coefficient results obtained are shown in Table 7, for the circular-spiral and L-shaped-element FSS arrays as well as the multilayer CP FSS structure.

Table 7: Measured polarimetric data for the structures investigated.

Polarimetric data	L-shaped elements	Spiral elements	Multilayer FSS structure
S_1/S_0	–0.0045	–0.1914	0.6264
S_2/S_0	0.0729	–0.1323	–0.4428
S_3/S_0	0.0399	0.0138	–0.3345
DOCP	0.0398	0.0137	0.2809
DOLP	0.0731	0.2327	0.7671
DOP	0.0832	0.2331	0.8368
DOUP	0.9965	0.9725	0.5475

The initial purpose of the planar FSS designs was to verify the validity of the FDT, such that cross-polarized thermal emission would ultimately be suppressed. The data shown on Table 7 clearly illustrates the lack of correlation between orthogonal surface currents, since the L-shaped wedge element array results in mostly unpolarized radiation, and the circular spiral elements emit negligible CP radiation. Thus, we have experimentally verified that the orthogonal field components are uncorrelated, and that thermal emission of CP radiation is not feasible with a planar structure. The data for the multilayer CP FSS structure incorporating the aerogel isolation layer shows a strong LP emission, which is expected from thermal excitation of the meanderline wires. However, the DOCP for this structure is also significant, at 28%. To our knowledge, this is the first time that a thermally emitted CP signature was obtained over a broad spectrum using planar multilayer FSS structures.

4.6 Implications of Results and Impact upon the Fluctuation Dissipation Theorem

The results of Table 7 are in no way contradictory of the consequential behavior imposed by the FDT. In fact, the data supports such claims, since purely planar structures in thermal contact with an elevated-temperature source did not exhibit any significant correlation between cross-polarized components, rendering these structures unable to emit broadband CP radiation. It is only when stratified layers are thermally isolated by a dielectric cavity of silica aerogel that we observe a steady-state temperature difference between the LP-radiating grid and the transmissive meanderline QWP layer, which yields a finite yet discernable DOCP coefficient. Nonetheless, the presence of a strong LP component that radiates from the meanderline wires is indicative of conductive thermal excitation that proliferates from the underlying emissive layers. Since the thermal barrier of silica aerogel can only provide a finite temperature difference, mostly because of its relatively compact thickness, the meanderline elements still exhibit a characteristic LP emission signature, which suggests that the FDT is not violated. In fact, in viewing the data from Table 7, we are witnessing the interplay between transmissive and emissive behavior, where one would predominate over the other if suitable conditions were provided. Thus, we can conclude that the FDT holds for structures that are brought up to the elevated emission temperature of the active blackbody source. Furthermore, as we have shown in this chapter, the FDT is able to be circumvented via thermal isolation, which enables the generation of thermally emitted broadband CP fields from planar periodic FSS meanderline components. Although this is a mere proof-of-concept demonstration, the technology and underlying concept could be applied to an assortment of devices and scenarios for IR detection, target recognition, and polarimetry system calibration.

CHAPTER 5: CONCLUSIONS

5.1 Summary

The present dissertation has demonstrated the ultimate versatility of planar periodic meanderline elements that can be incorporated into systems that exploit transmissive, reflective, or emissive behavior. Its broadband achromatic characteristics have been engineered and fabricated to result in ideal QWP performance for IR radiation that passes through or reflects from the multilayered meanderline components over a wide range of oblique incident angles. Pertinent focus upon real-world applications has resulted in fabrication and demonstration of low-profile, low-cost, easy-to-fabricate wide-area format QWPs for imaging CP via Stokes polarimetry, and extremely large-area CP tags that are able to produce CP light in the IR spectrum, and thus be discerned from any natural source of thermal polarized radiation. Finally, with the assistance of a thermal dielectric barrier of silica aerogel, subwavelength meanderline elements have also been shown to convert LP emission into CP, thereby providing an intrinsic source of CP thermal emission. Although the DOCP was not at its absolute maximum, mostly because of the finite temperature differential between the LP emitting wire grid layer and the transmissive meanderline QWP elements, the initial performance is promising enough for further investigations of such structures, which may find use in many relevant applications pertaining to broadband imaging polarimetry, target detection, and spectroscopy in the thermal IR spectrum.

5.2 Future Work

With regard to the devices and multilayered structures that have been presented thus far, there are some improvements that can be considered which may augment the performance in favor of increased power throughput. In particular, the transmissive multilayer meanderline QWPs could potentially yield throughput coefficients of 70% and higher with the right type of interlayer dielectric material. Even though such structures were simulated and fabricated with a low-loss cavity layer of YF_3 dielectric, other ideal materials were not considered or implemented, specifically because of the difficulty in locating a compatible spin-on dielectric resin that would exhibit low enough optical attenuation in the LWIR band. However, there has been, in recent years, continued research into low-loss sol-gel solutions, such as Calcium Fluoride (CaF), which may be able to provide optimum optical characteristics with the required spin-on coating capabilities that would facilitate multilayer device fabrication [158]. Other material composites of spin-on sol-gels may yield significant transmission throughput gains and impedance-matching capabilities for multilayer meanderline QWPs, which will all but guarantee the elevation of the transmittance throughput beyond the 70% mark. Such dielectrics could also be incorporated into the reflective meanderline QWP structures for similar benefits. Metamaterial-based effects, such as extraordinary optical transmission (EOT) and evanescent wave tunneling [55,56], could have potential value for increasing the power throughput, although such effects would have to surpass the present ohmic losses incurred by the finite-conductivity metallic elements [104].

Although the thermally emissive CP multilayer structure with silica aerogel was meant as a first principle demonstration of circumventing the FDT, there are some improvements that can be gained from the aerogel material processing and choice of thermal isolation layer. It was mentioned that, upon deposition of more than 2 layers of silica aerogel, the aerogel film started crack apart, which precluded further processing of any subsequent layers. This ultimately limited the integrated meanderline QWP device to a single-layer configuration, specifically because no other layers could be fabricated without substantial deterioration of the silica aerogel film. As shown in the following figure, the difference between 2-layer and 3-layer depositions of aerogel dielectric is significant enough to pose a hazardous threat to any stratified layers above the damaged film.

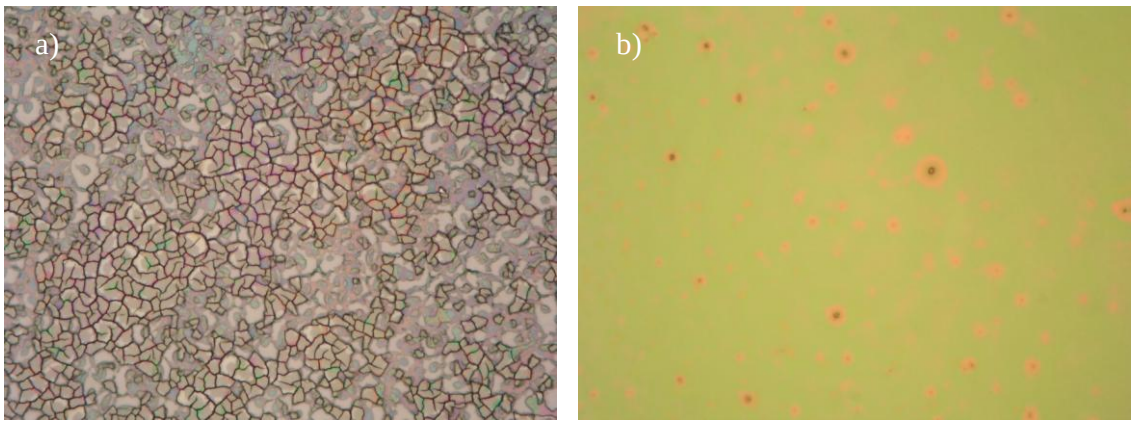

Figure 80: Pictures of silica aerogel surface resulting from complete fabrication process after a) 3 layers, and b) 2 layers of aerogel solution were deposited.

In order to mitigate such deterioration and cracking of the aerogel dielectric film, improved deposition and thermal curing processes could be implemented, such that increased stability between successive depositions of aerogel layers would result in successful build-up of more

than 3 layers [157]. As a result, the temperature differentiation between the emissive wire grid structures and the meanderline QWP layer would be increased, thereby yielding improved CP characteristics and, consequently, diminished values of the DOLP coefficient. Furthermore, other aerogel compounds may be even more transparent in the thermal IR than silica-based films [156,157]. Comprehensive investigations of such aerogel dielectrics with low thermal conductivity and increased thicknesses could potentially result in a drastically improved structure with an even higher coefficient of emitted DOCP.

Many planar metamaterial and FSS designs have undergone recent transformations to include exotic optical effects, such as nonlinear behavior and tunable switching characteristics. The latter has recently been demonstrated in the IR regime with thermochromic vanadium oxide (VO_2), which exhibits a material phase change across a range of applied temperature hysteresis [159]. As shown in Figure 81, the thin-film resistivity and optical constants change drastically upon heating and cooling of the VO_2 material, which effectively switches from dielectric to metallic-type behavior when the ambient temperature is increased.

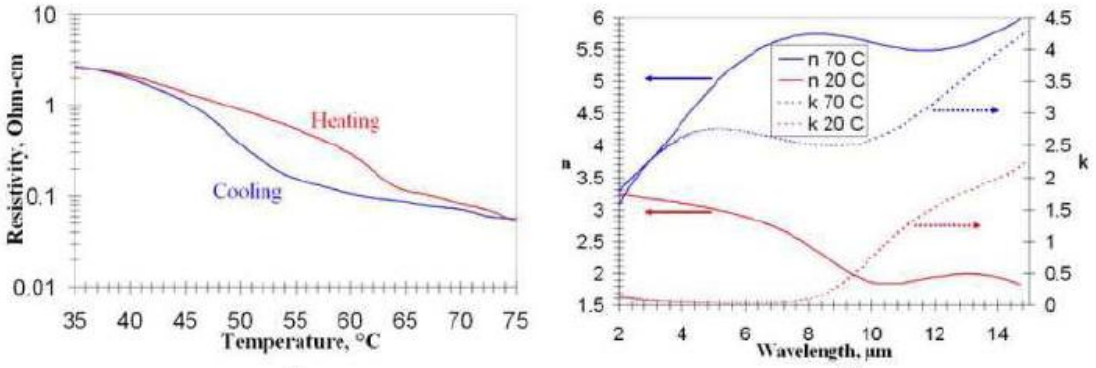

Figure 81: Thin-film resistivity hysteresis and temperature-dependent optical constants of thermochromic VO_2 (from [159]).

The modulation in thin-film resistivity indicates temperature switching behavior that can be applied to circuit elements of any conceivable planar periodic metamaterial and FSS structure. Such thermochromic material has already been incorporated into tunable phase-shaping reflectarray elements [159], so it would be logical to extend such behavior to provide tunable capability to subwavelength meanderline retarders and QWP components. The obvious limiting factor is that the structure would have to be heated under operational conditions, which would limit the functional behavior to reflective meanderline retarders for the time being. Additionally, the switching behavior is dependent upon the material hysteresis and the time lag between successive modulations in temperature. Apart from this, VO_2 could be successfully integrated into meanderline unit cells, such that tunable characteristics are achieved with regard to phase-shifting FSS structures. Although a particular design would have to be strictly optimized according to the material parameters, a possible application could involve having both QWP and half-wave plate (HWP) functionality on a single element, with the difference in operational behavior immediately accessible via a simple increase or decrease of applied temperature. This would reduce costs even further by decreasing the amount of components necessary for achieving a desired wave retardance, which would be available by sweeping through the range of temperatures corresponding to the material hysteresis of VO_2. Therefore, subwavelength tunable meanderline retarders would be a significant advancement in the field of IR QWP technology, which would practically herald the replacement of all existing IR QWP methods and apparatuses to-date.

APPENDIX: DETAILED PROCESS NOTES ON ELECTRON-BEAM MICROFABRICATION OF PLANAR PERIODIC SUBWAVELENGTH STRUCTURES

A.1 Fabrication of Multilayer Planar Periodic FSS Grid Arrays on Various Materials

The primary function of this appendix will be to clarify the exact procedures and methodologies that were implemented in the construction of the multilayer subwavelength meanderline retarders and polarization-selective devices presented in Chapters 3 and 4, with special attention paid to certain unconventional materials that are not typically classified as being compatible with e-beam lithography processing. Such exposition of methods is absolutely essential for re-production of the aforementioned devices, especially since e-beam exposure of subwavelength linewidth features is dependent upon the composition and the interaction of the material interface with the developer chemical and the ZEP 520-A7 resist. This concept will be further illuminated by the ensuing processing details concerning multilayer FSS fabrication on various substrates and planar dielectric materials.

A.1.1 Semiconductor Substrates

Although bulk semiconductor materials were not explicitly used in the current body of work, the description of the fabrication routine serves as a good foundation for building up the crucial knowledge that will be implemented for other 'exotic' material systems. Thus, we assume that the available semiconductor material is given as a typical 3" or 4" diameter substrate that is polished at least on one side, if not both for optimum transmission performance. The exact material in question is also assumed to be of low doping/impurity concentration, such that thermal IR light is not prone to excess free-carrier absorption within the bulk semiconductor substrate. Such examples of compatible semiconductor substrate material can be listed as un-

doped Gallium Arsenide (GaAs), Germanium (Ge), and high-resistivity Si, to name a few. With these assumptions taken into account, the fabrication procedure on semiconductor wafers is as follows:

1. Spin-clean polished side of wafer @ 4000 rpm with Acetone, Methanol, and Iso-Propanol Alcohol (IPA) dynamically applied to surface of substrate. Bake at 180° C for approximately 3 minutes to evaporate all the solvents out of the wafer. Follow up with an oxygenated plasma descum barrel etch at 200 W forward RF excitation for roughly 2 minutes.
2. Dynamically spin on ZEP e-beam resist at about 300 rpm, and then ramp up to final spin speed of 3000 rpm, which is held for approximately 60–80 seconds. Bake at 180° C for 3 minutes, so that solvents do not out-gas into the ultra-high vacuum e-beam chamber.
3. Submicron linewidth exposure on semiconductor wafers does not require any modification to the aforementioned materials and/or resists. This is due to the highly-reflective conducting surface of the substrate material, which allows for adequate reflection for internal height reference and substrate tilt calibration, and for conduction of the excess electrons which will otherwise overexpose the resist via substrate charging. For example, about 95 $\mu C/cm^2$ of e-beam dosage at 100 nA of beam current will net a 100 nm over-exposure when writing 300 nm lines with the Leica e-beam system (Figure 23) when developed with ZEP RD. Development with high-resolution Amyl Acetate will net approximately a 1:1 exposure to development ratio with regard to fractured linewidths.

4. After exposure is complete, development can be done either by ZEP RD or Amyl Acetate chemical solutions. The sample should be completely immersed in the chosen developer for approximately 1 minute, and then immediately rinsed in IPA to impede the development reaction. After blowing dry with Nitrogen (N_2) air, barrel-etch the remaining undeveloped resist for 2 minutes at 200 W.
5. The exposed and developed patterns can now be metalized by physical vapor deposition of the choice metals for optimum device performance. This can be done by either e-beam or thermal evaporation methods.
6. After deposition of the required metals, a liftoff process is necessary to remove the excess materials from the patterned surface, which will yield a completed structure, or at least the initial layer of a multilayered FSS device. Although Methylene Chloride has served as a liftoff chemical agent in the past, ZEP remover (N-dimethylacetamide) is employed because it aggressively attacks the remaining ZEP 520-A7 resist, thereby lifting off both excess resist and metals from the structured surface. Once the sample is thoroughly soaked in ZEP remover (preferably done in a Tupperware container), the entire ensemble is sonically agitated for about 5 minutes for initial metal and ZEP resist removal. Further agitation may be necessary for additional liftoff of excess detritus if the initial agitation process wasn't enough for complete dissociation of the remaining contaminants from the FSS. Once agitation is completed, the structure should be thoroughly rinsed with Acetone and IPA (in that order), and dried with N_2 air. The device is now ready for characterization and further processing.

A.1.2 Transparent Insulating Substrates

Unlike semiconducting wafers, transparent insulating substrates are not immediately compatible with e-beam lithographic processing. The Leica e-beam system requires a reflective surface so that substrate heights can be measured, which enables proper focusing of the impinging electron beam. Insulating wafers that are transparent in the visible are therefore susceptible to exposure errors due to incorrect height referencing, since the internal laser interferometer of the Leica system cannot register surfaces that have a weak back-scattered signal. Furthermore, the absence of a conducting material may overexpose the critical linewidth features, since excess electrons will lead to charging of the insulating substrate and dielectric layers. Because transparent insulators, such as fused silica (SiO_2) and Barium Fluoride (BaF_2), enable enhanced transmission throughput without the need for multilayer anti-reflection coatings, it would be desirable to formulate a process that would incorporate such materials into multilayer planar FSS microfabrication routines. The current section will outline the methods that were implemented in the construction of meanderline FSS components on SiO_2 and BaF_2 substrates.

1. As before, spin-clean the substrate at 4000 rpm with Acetone, Methanol, and IPA in that exact order. For the SiO_2 substrate, proceed to bake at 180° C for 3 minutes. However, since BaF_2 is susceptible to thermal shock, no thermal cure is necessary at this stage. SiO_2 may be subjected to oxygenated plasma descum at 200 W forward RF after baking

out the solvents. BaF_2, on the other hand, is a very fragile crystalline material that scratches easily, so no barrel etch processing should be performed as of yet.

2. Spin on ZEP resist using dynamic spin-coating application at 300 rpm, then ramp up to the final spin speed of 3000 rpm, which is held for approximately 80 seconds. After spinning, the SiO_2 wafer should be baked at 180° C for 3 minutes to drive out the remaining solvents. However, unlike SiO_2, BaF_2 cannot be subjected to rapid changes in ambient temperature, since it must be gradually cooled to avoid any instance of thermal fracturing. Thus, set a variable hot-plate at 110° C, set the ZEP-coated BaF_2 wafer upon it for 1 minute, and then turn the hot-plate off. Wait until the substrate has cooled down to room temperature (takes about 20–25 minutes).
3. In most circumstances, direct patterning of subwavelength features on a substrate requires no foreknowledge of design orientation or location, since it is usually the 1st FSS layer that is scribed upon the bare wafer. Thus, to enable accurate height reflection mapping and conduction of excess electrons, a thin layer of Nickel (Ni) can be sputtered directly onto the wafer. Although any thin metal film will do, Ni was chosen because it exhibits very poor adhesion characteristics with ZEP resist, and can thus be peeled off easily after exposure. Sputtering is a highly uniform and directional deposition procedure, so this benefits our circumstance in that it preserves the planar features of the un-patterned wafer. For the devices that were presented in Chapter 3, about 40 nm of Ni was sputtered over the ZEP resist on the 1st layer of the FSS structure.
4. E-beam exposure can be performed after completion of the Ni sputtering step. As was mentioned before, each material system has a unique surface chemistry that requires

separate conditions for proper development of the optimum linewidths. For example, 105–115 $\mu C/cm^2$ should be enough for development of 400 nm lines at 100 nA beam current with ZEP RD on SiO_2. Likewise, the same amount of dosage and beam current works well with similar linewidths on BaF_2 with ZEP RD as the developer. Thicker linewidths entail lower dosages, such as 75–85 $\mu C/cm^2$, when developed with Amyl Acetate. Thus, it should be apparent that the necessary electron dosage, beam current (which controls the spot-size), and developer depends upon the critical features of the subwavelength FSS pattern, thereby requiring some trial and error testing for optimal exposure results.

5. Once exposure is complete, the Ni film is peeled off very carefully with adhesive tape. As to not contaminate the surface composition of the ZEP resist, the tape should only be applied to areas that are coated with Ni. Although minor traces of Ni may be left behind, this should not affect the development of submicron features in ZEP resist. At this point, the development methods for SiO_2 and BaF_2 diverge due to the surface chemistry and interaction of each developer with the substrate material. For SiO_2, the wafer can be immersed in ZEP RD (or Amyl Acetate) for about 1 minute, and immediately rinsed thereafter with IPA and dried with N_2 air. The BaF_2 development process, on the other hand, requires a drastically separate approach, as complete immersion in developer for 1 minute or more will over-expose the critical linewidths. In fact, only 20 seconds of development time in either ZEP RD or Amyl Acetate is needed. Thus, it is much more convenient to directly dispense the developer onto the exposed portion of ZEP with pipettes, thereby enabling secure handling of the BaF_2 substrate once 20 seconds has

elapsed. At the conclusion of development, the structure should be immediately rinsed in IPA and dried with N_2 air.

6. Barrel etching is commenced after development to remove any stray ZEP particulates that remain after rinsing with IPA. A 2 minute plasma descum at 200 W forward RF power is sufficient for ZEP resist on SiO_2. However, due to the fragility of the BaF_2 surface, the barrel etching duration should be reduced to 1 minute for the same amount of RF power. Deposition of the requisite metals by thermal or e-beam evaporative methods follows the same procedure as before. Regarding BaF_2, it should be noted that thermal or e-beam evaporation may raise the internal temperature of the chamber, which must be allowed to cool to ambient levels. Also, one should exercise caution when handling BaF_2 wafers, as their respective surfaces are easily prone to scratching when hastily mounted in evaporation systems.
7. Liftoff should follow the same steps as the previous section, such that each sample is immersed in ZEP remover and sonically agitated for 5 minutes, or until all excess materials have detached from the surface of the metalized FSS structure. Upon termination of the sonic agitation process, the wafers are rinsed with Acetone and IPA (in that order), and dried with N_2 air. Again, caution must be wielded with respect to handling and care of BaF_2 wafers, especially since sonic agitation may increase the substrate temperature under prolonged liftoff cycles. Thus, after agitation, BaF_2 substrates should remain in the ZEP remover chemical until the material has arrived at ambient temperature. Once liftoff is finished, the patterned FSS structure is ready for inspection, characterization, and further processing.

A.1.3 Stratified Dielectric Layers

The current section covers the necessary procedures for planar FSS device fabrication on stratified dielectric layers. With respect to the multilayer devices that were presented in Chapters 3 and 4, we shall describe processing specifics exclusive to particular dielectric materials, such as BCB and ZnS, that were implemented in multilayer FSS construction. Thus, we begin with a description of the processing steps that enable fabrication of subwavelength FSS elements upon layers of Benzocyclobutene (BCB), a spin-on dielectric polymer provided by DOW Chemical.

1. Assuming that the 1st meanderline FSS layer is complete, a spin-clean with Acetone, Methanol, and IPA at 4000 rpm should be sufficient enough to prepare the substrate surface for deposition of BCB. A subsequent solvent bake and barrel etch may follow this initial cleaning step. Regarding the exact processes for substrates such as BaF_2, it would do well to glance over the previous section for a brief review of material handling concerns and specifics relating to thermal and mechanical shock tolerances.
2. Before spinning on the required thickness of BCB, the adhesion polymer must be deposited first to ensure stable chemical and mechanical bonds between the substrate and dielectric layers. Thus, dynamically spin on BCB adhesion promoter (HDMS) at 300 rpm, and ramp up to a spin speed of 2000 rpm, which is held for about 20 seconds. Afterwards, immediately spin on the desired BCB solution, which can be thinned with Mesitylene if a thinner layer is warranted. Dynamic application of BCB is done at about

300 rpm, and the final spin speed is usually kept around 3000 rpm for 60 seconds, although other speeds are used if different thicknesses are requested from the same solution of BCB.

3. Once the spin-on application of BCB is complete, the polymer dielectric requires curing at 250° C. This allows for the BCB film to be baked into a hard rigid dielectric layer that can withstand subsequent fabrication steps. However, to ensure a smooth transition up to the optimum curing temperature, the coated sample is first baked at 120° C for approximately 3 minutes. Then, the temperature is ramped up to 250° C, and the sample is encased within a N_2-purge environment. This precludes oxidation of the film under high temperature baking, and further inhibits the formation of oxygen bubbles within the BCB dielectric layer. The film is baked at 250° C for 5 minutes, after which the sample remains in the N_2-purge environment while the temperature ramps down to 180° C. Depending upon the substrate material, the sample can now be removed from the hot-plate, or in the case of BaF_2, remain until it has cooled down to room temperature. If additional layers of BCB are required, this same process can be repeated iteratively.
4. ZEP e-beam resist is applied in the usual manner (see the previous sections), with the exception of one important step. Since BCB is an insulating material, much like SiO_2 and BaF_2, we must apply some sort of coating that prohibits excess charging upon electron beam exposure. However, we cannot simply deposit a thin layer of Ni, since the to-be-written FSS features need to be visibly aligned with the preceding FSS grid layers. AquaSave, provided by Mitsubishi Corp., takes care of this dilemma, since it is a transparent yet conducting polymer that can easily route the excess electrons from the

exposure area. This solution is statically applied, spun at 3000 rpm for 60 seconds, and then baked at 110° C for about 3 minutes. As always, with BaF_2, bake at 110° C for 1 minute and turn the hot-plate off to let the substrate cool to room temperature. Ni can now be sputtered around edges of the wafer, which will provide suitable height registration for precise exposure. To avoid direct sputtering over the 1st FSS grid array, cover the to-be-exposed area with a thin sheet of aluminum (Al) foil while leaving the surrounding perimeter un-covered. This will preserve the visibility through the multilayer stack for precise alignment with the preceding FSS layers.

5. It has been found that e-beam exposure on stratified dielectric layers takes a little bit more electron dosage to arrive at the preferred structural dimensions, at least when using a layer of AquaSave above ZEP. Thus, for example, 125 $\mu C/cm^2$ with 100 nA beam current would be appropriate for exposure of 400 nm lines when using ZEP RD developer. Amyl Acetate would develop thinner lines closer to the fractured linewidths, so higher electron dosages may be necessary. In any case, because the area directly over the exposed pattern is covered in AquaSave, and not Ni, a pre-mapping height routine must be initialized in order to map the heights around the FSS grid array. The location of the pattern layout should be centered directly in the middle of the previous FSS array, and aligned so that the FSS features properly coincide between layers once development is completed. Apart from these minor details, the e-beam exposure process is the same as in the previous sections.
6. After exposure, the Ni film and the AquaSave layer can be removed from the ZEP resist. In terms of process sequencing, the Ni layer is usually peeled off with tape before the

AquaSave is rinsed away with deionized water. Once the exposed area of ZEP is clear of the aforementioned materials, the sample development, barrel-etch, metallization, and liftoff steps should follow the same exact procedure outlined in the previous sections.

Although the above processing methods are exclusive to BCB, they can be augmented to facilitate other dielectrics, such as Zinc Sulfide (ZnS) or silica aerogel.

ZnS dielectric layers were deposited via thermal evaporation in a low pressure environment. Deposition was performed over an adhesive layer of metallic Aluminum (Al) or Aluminum Oxide (Al_2O_3), depending upon the intended operation of the FSS structure (reflective vs. transmissive). The evaporation rate was sustained at 4.5 Angstroms per second throughout the deposition cycle. Upon completion of ZnS evaporation, the fabrication procedure almost follows that of BCB, except that no assistive materials were deposited above the spin-coated layer of ZEP resist, since the precursor Al layer provides a) ample height registration, and b) partial conduction of the excess electrons, which mitigates charging of the dielectric film. Furthermore, high-resolution Amyl Acetate was chosen as the developer, so neither conductive Ni or AquaSave were required in the e-beam exposure stages.

Silica aerogel, which was implemented as a thermal isolation standoff layer in Chapter 4, was deposited by spin-coating techniques. To achieve the required thickness of aerogel film, sequential spin-coatings were performed at 1500 rpm, with the aerogel solution applied statically to the plasma-cleaned semiconductor substrate. Because of the porous nature of silica aerogel, multiple spin coating applications were required before baking could be attempted. After spin-coating was complete, the aerogel film was baked at 120° C for 10 minutes to drive out the

remaining ethanol solvent. A layer of thinned BCB (approx. 350 nm thick) was subsequently deposited over the aerogel to cap and planarize the porous silica film. The rest of the process steps are the same as those for ZnS, as no other dielectric or metal layers were utilized for e-beam exposure of the ZEP resist.

LIST OF REFERENCES

[1] D.J. Griffiths, *Introduction to Electrodynamics*, (Prentice Hall, Upper Saddle River, NJ, 1999).

[2] L.D. Landau and E.M. Lifshitz, *Electrodynamics of Continuous Media*, (Pergamon Press, New York, 1960).

[3] L. Mandel and E. Wolf, *Optical Coherence and Quantum Optics*, (Cambridge, New York, NY, 1995).

[4] R.L. Liboff, *Introductory Quantum Mechanics*, (Addison Wesley, San Francisco, CA, 2003).

[5] T. Setala, A. Shevchenko, M. Kaivola, and A.T. Friberg, "Degree of polarization for optical near fields," Phys. Rev. E. **66**(1), 016615 (2002).

[6] T. Carrozi, R. Karlsson, and J. Bergman, "Parameters characterizing electromagnetic wave polarization," Phys. Rev. E **61**(2), 2024–2028 (2000).

[7] E. Hecht, *Optics*, (Addison Wesley, San Francisco, CA, 2002).

[8] D. Goldstein, *Polarized Light 2nd Ed.*, (Marcel Dekker, New York, NY, 2003).

[9] R.M.A Azzam and N.M Bashara, *Ellipsometry and Polarized Light*, (Elsevier North-Holland, New York, 1977).

[10] A. Yariv and P. Yeh, *Photonics: Optical Electronics in Modern Communications*, (Oxford University Press, New York, 2007).

[11] E.L. Geiszelmann, S.F. Jacobs, and H.E. Morrow, "Simple quartz birefringent quarter-wave plate for use at 3.39 μm," J. Opt. Soc. Am. **59**(10), 1381–1383 (1969).

[12] Meadowlark Optics, I. *Sources of Error in Retarders and Waveplates*. 2005 [cited; http://www.meadowlarkoptics.com/]

[13] P.D. Hale and G.W. Gay, "Stability of Birefingent Linear Retarders," Appl. Optics **27**(24), 5146–5153 (1988).

[14] M. Fox, *Optical Properties of Solids*, (Oxford, New York, 2001).

[15] E.D. Palik, *Handbook of optical constants of solids, vol. III.*, (Academic, San Diego, CA, 1997).

[16] E.H. Korte, B. Jordanov, D. Kolev, and D. Tsankov, "Total reflection prisms as achromatic IR retarders," Appl. Spectrosc. **42**(8), 1394–1400 (1988).

[17] R.M.A. Azzam and H.K. Khanfar, "In-line broadband 270° (3λ/4) chevron four-reflection wave retarders," Appl. Optics **47**(27), 4878–4883 (2008).

[18] W.C. Yip, H.C. Huang, and H.S. Kwok, "Achromatic wave retarder by phase subtraction," Appl. Optics **35**(22), 4381–4384 (1996).

[19] E. Cojocaru, T. Julea, and F. Nichitiu, "Infrared thin-film totally reflecting quarter-wave retarders," Appl. Optics **30**(28), 4124–4125 (1991).

[20] R.M.A. Azzam and C.L. Spinu, "Achromatic angle-insensitive infrared quarter-wave retarder based on total internal reflection at the Si-SiO2 interface," J. Opt. Soc. Am. A **21**(10), 2019–2022 (2004).

[21] J. Schirmer and T. Schmidt-Kaler, "Liquid crystal phase retarder with broad spectral range," Opt. Commun. **176**, 313–317 (2000).

[22] Q. Hong, T.X. Wu, R. Lu, and S.T. Wu, "Wide-view circular polarizer consisting of a linear polarizer and two biaxial films," Opt. Express **13**(26), 10777–10783 (2005).

[23] N.N. Nagib, S.A. Khodier, H.M. Sidki, and A.A. Abd El Megeed, "Polymeric sheets as phase retardation elements," Meas. Sci. Technol. **12**, 1714–1717 (2001).

[24] R.C. Sharp, D.P. Resler, D.S. Hobbs, and T.A. Dorschner, "Electrically tunable liquid-crystal wave plate in the infrared," Opt. Lett. **15**(1), 87–89 (1990).

[25] A. Lompado, E.A. Sornsin, and R.A. Chipman, "HN22 sheet polarizer, an inexpensive infrared retarder," Appl. Optics **36**(22), 5396–5402 (1997).

[26] L. Novotny and B. Hecht, *Principles of Nano-Optics*, (Cambridge, New York, 2006).

[27] G.P. Nordin and P.C. Deguzman, "Broadband form birefringent quarter-wave plate for the mid-infrared wavelength region," Opt. Express **5**(8), 163–168 (1999).

[28] D.C. Flanders, "Submicrometer periodicity gratings as artificial anisotropic dielectrics," Appl. Phys. Lett. **42**(6), 492–494 (1983).

[29] F. Xu, R.-C. Tyan, P.-C. Sun, Y. Fainman, C.-C. Cheng, and A. Scherer, "Fabrication, modeling, and characterization of form-birefringent nanostructures," Opt. Lett. **20**(24), 2457–2459 (1995).

[30] H. Kikuta, Y. Ohira, and K. Iwata, "Achromatic quarter-wave plates using the dispersion of form birefringence," Appl. Optics **36**(7), 1566–1572 (1997).

[31] D.L. Brundrett, E.N. Glytsis, and T.K. Gaylord, "Subwavelength transmission grating retarders for use at 10.6 μm," Appl. Optics **35**(31), 6195–6202 (1996).

[32] P.C. Deguzman and G.P. Nordin, "Stacked subwavelength gratings as circular polarization filters," Appl. Optics **40**(31), 5731–5737 (2001).

[33] G. Kang, Q. Tan, X. Wang, and G. Jin, "Achromatic phase retarder applied to MIWR & LWIR dual-band," Opt. Express **18**(2), 1695–1703 (2010).

[34] R.B. Boye, S.A. Kemme, J.R. Wendt, A.A. Cruz-Cabrera, G.A. Vawter, C.R. Alford, T.R. Carter, and S. Samora, "Fabrication and measurement of wideband achromatic waveplates for the mid-infrared region using subwavelength features," J. Microlith., Microfab., Microsyst. **5**(4), 043007 (2006).

[35] S.A. Kemme, A.A. Cruz-Cabrera, R.R. Boye, T. Carter, S. Samora, C. Alford, J.R. Wendt, G.A. Vawter, and J.L. Smith, "Micropolarizing device for long wavelength infrared polarization imaging," Sandia National Lab., Albuquerque, NM, Sandia Report SAND2006-6889 (2006).

[36] H. Kikuta, K. Numata, M. Muto, K. Iwata, H. Toyota, K. Moriwaki, T. Yotuya, and H. Sato, "Polarization imaging camera with form birefringent micro-retarder array," Frontiers in Optics, OSA Technical Digest (CD), (2003).

[37] J.C.W. Lee and C.T. Chan, "Polarization gaps in spiral photonic crystals," Opt. Express **13**(20), 8083–8088 (2005).

[38] C.S.L. Chun, "Microscale waveplates for polarimetric infrared imaging," Proc. SPIE **5074**, 286–297 (2003).

[39] L.-M. Li, "Two-dimensional photonic crystals: Candidate for wave plates," Appl. Phys. Lett. **78**(22), 3400–3402 (2001).

[40] Q.F. Dai, Y.W. Li, and H.Z. Wang, "Broadband two-dimensional photonic crystal wave plate," Appl. Phys. Lett. **89**(6), 061121 (2006).

[41] D.R. Solli and J.M. Hickmann, "Engineering an achromatic photonic crystal waveplate," New Journ. Phys. **8**, 132 (2006).

[42] D.R. Solli, C.F. McCormick, R.Y. Chiao, and J.M. Hickmann, "Experimental demonstration of photonic crystal waveplates," Appl. Phys. Lett. **82**(7), 1036–1038 (2003).

[43] M. Thiel, M. Hermatschweiler, M. Wegener, and G. von Freymann, "Thin-film polarizer based on a one-dimensional-three-dimensional-one-dimensional photonic crystal heterostructure," Appl. Phys. Lett. **91**(12), 123515 (2007).

[44] J. Liu and R.M.A. Azzam, "Infrared quarter-wave reflection retarders designed with high-spatial-frequency dielectric surface-relief gratings on a gold substrate at oblique incidence," Appl. Optics **35**(28), 5557–5562 (1996).

[45] V.N. Okorkov, V.Y. Panchenko, B.V. Russkikh, V.N. Seminogov, V.I. Sokolov, and V.P. Yakunin, "Phase retarder for transformation of polarization of high-power infrared laser beams based on resonant excitation of surface electromagnetic waves on metallic diffraction gratings," Opt. Eng. **33**(10), 3145–3155 (1994).

[46] Y. Pang and R. Gordon, "Metal nano-grid reflective wave plate," Opt. Express **17**(4), 2871–2879 (2009).

[47] S.A. Ramakrishna and T.M. Grzegorczyk, *Physics and Applications of Negative Index Materials*, (SPIE Press, Boca Raton, FL, 2009).

[48] H.O. Moser et al, "Free-standing THz electromagnetic metamaterials," Opt. Express **16**(18), 13773–13780 (2008).

[49] K. Busch, G. von Freymann, S. Linden, S.F. Mingaleev, L. Tkeshelashvili, and M. Wegener, "Periodic nanostructures for photonics," Phys. Reports **444**, 101–202 (2007).

[50] C. Rockstuhl, C. Menzel, T. Paul, C. Helgert, E. Pshenay-Severin, J. Petschulat, A. Chipouline, T. Pertsch, and F. Lederer, "Bulk properties of metamaterials," Proc. SPIE **6987**, 69871O (2008).

[51] E. Pshenay-Severin, U. Hubner, C. Menzel, C. Helgert, A. Chipouline, C. Rockstuhl, A. Tunnermann, F. Lederer, and T. Pertsch, "Double-element metamaterial with negative index at near-infrared wavelengths," Opt. Lett. **34**(11), 1678–1680 (2009).

[52] T.G. Mackay and A. Lakhtakla, "Negatively refracting chiral metamaterials: a review," SPIE Reviews **1**, 018003 (2010).

[53] J.B. Pendry, "Negative refraction makes a perfect lens," Phys. Rev. Lett. **85**(18), 3966–3969 (2000).

[54] I.V. Shadrivov, A.A. Zharov, Y.S. Kivshar, "Second-harmonic generation in left-handed nonlinear metamaterials," J. Opt. Soc. Am. B. **23**(3), 529–534 (2006).

[55] R. Marques, F. Mesa, L. Jelinek, and F. Medina, "Analytical theory of extraordinary transmission through metallic diffraction screens perforated by small holes," Opt. Express **17**(7), 5571–5579 (2009).

[56] F. Medina, F. Mesa, and R. Marques, "Extraordinary transmission through arrays of electrically small holes from a circuit theory perspective," IEEE Trans. Microwave Theory Tech. **56**(12), 3108–3120 (2008).

[57] C.E. Kriegler, M.S. Rill, S. Linden, and M. Wegener, "Bianisotropic photonic metamaterials," IEEE J. Sel. Top. Quant. Elect. **16**(2), 367–375 (2010).

[58] J.K. Gansel, M. Thiel, M.S. Rill, M. Decker, K. Bade, V. Saile, G. von Freymann, S. Linden, and M. Wegener, "Gold helix photonic metamaterial as broadband circular polarizer," Science **325**, 1513–1515 (2009).

[59] Z.Y. Yang, M. Zhao, P.X. Lu, and Y.F. Lu, "Ultrabroadband optical circular polarizers consisting of double-helical nanowire structures," Opt. Lett. **35**(15), 2588–2590 (2010).

[60] M. Thiel, H. Fischer, G. von Freymann, and M. Wegener, "Three-dimensional chiral photonic superlattices," Opt. Lett. **35**(2), 166–168 (2010).

[61] Z.Y. Yang, M. Zhao, and P.X. Lu, "A numerical study on helix nanowire metamaterials as optical circular polarizers in the visible region," IEEE Photon. Tech. Lett. **22**(17), 1303–1305 (2010).

[62] M. Iwanaga, "Ultracompact waveplates: approach from metamaterials," Appl. Phys. Lett. **92**(15), 153102 (2008).

[63] J.Y. Chin, J.N. Gollub, J.J. Mock, R. Liu, C. Harrison, D.R. Smith, and T.J. Cui, "An efficient broadband metamaterial wave retarder," Opt. Express **17**(9), 7640–7647 (2009).

[64] J. Hao, Y. Yuan, L. Ran, T. Jiang, J.A. Kong, C.T. Chan, and L. Zhou, "Manipulating electromagnetic wave polarizations by anisotropic metamaterials," Phys. Rev. Lett. **99**(6), 063908 (2007).

[65] M. Mutlu, A.E. Akosman, A.E. Serebryannikov, and E. Ozbay, "Asymmetric chiral metamaterial circular polarizer based on four U-shaped split ring resonators," Opt. Lett. **36**(9), 1653–1655 (2011).

[66] W. Sun, Q. He, J. Hao, and L. Zhou, "A transparent metamaterial to manipulate electromagnetic wave polarizations," Opt. Lett. **36**(6), 927-929 (2011).

[67] J.Y. Chin, M. Lu, and T.J. Cui, "Metamaterial polarizers by electric-field-coupled resonators," Appl. Phys. Lett. **93**(25), 251903 (2008).

[68] J. Yang and J. Zhang, “Subwavelength quarter-waveplate composed of L-shaped metal nanoparticles,” Plasmonics **6**, DOI: 10.1007/s11468-010-9196-x (2011).

[69] D.R. Smith, S. Schultz, P. Markos, and C.M. Soukoulis, “Determination of effective permittivity and permeability of metamaterials from reflection and transmission coefficients,” Phys. Rev. B. **65**(19), 195104 (2002).

[70] L. Fu, H. Schweizer, H. Guo, N. Liu, and H. Giessen, “Synthesis of transmission line models for metamaterial slabs at optical frequencies,” Phys. Rev. B. **78**(11), 115110 (2008).

[71] W. Zhang and S.T. Chui, “A generalized equivalent circuit theory for the electric and magnetic resonances of metallic wire networks,” J. Appl. Phys. **105**(11), 113121 (2009).

[72] H. Oraizi and M. Afsahi, “Transmission line modeling and numerical simulation for the analysis and optimum design of metamaterial multilayer structures,” Prog. Emg. Research B. **14**, 263–283 (2009).

[73] C.S.R. Kaipa, A.B. Yakovlev, F. Medina, F. Mesa, C.A.M. Butler, and A.P. Hibbins, “Circuit modeling of the transmissivity of stacked two-dimensional metallic meshes,” Opt. Express **18**(13), 13309–13320 (2010).

[74] B. Monacelli, J. Pryor, B. Munk, D. Kotter, and G. Boreman, "Infrared frequency selective surface based on circuit-analog square loop design," IEEE Trans. Antennas Propag. **53**(2), 745-752 (2005).

[75] W. Schaich, G. Schider, J. Krenn, A. Leitner, F. Aussenegg, I. Pusçasu, B. Monacelli, and G. Boreman, "Optical resonances in periodic surface arrays of metallic patches," Appl. Optics **42**(28), 5714-5721 (2003).

[76] I. Pusçasu, G. Boreman, R. Tiberio, D. Spencer, and R. Krchnavek, "Comparison of infrared frequency-selective surfaces fabricated by direct-write electron-beam and bilayer nanoimprint lithographies," J.V.S.T. B. **18**, 3578-3581 (2000).

[77] E.C. Zimmermasn and A. Dalcher, “Incoherent radiative properties of an opaque body,” J. Opt. Soc. Am. A **8**(12), 1947–1954 (1991).

[78] L. Mandel and E. Wolf, “Coherence properties of optical fields,” Rev. Mod. Phys. **37**(2), 231–287 (1965).

[79] C.L. Mehta and E. Wolf, “Coherence properties of blackbody radiation. II. Correlation tensors of the quantized field,” Phys. Rev. **134**(5A), A1149–A1153 (1964).

[80] F. Marquier, K. Joulain, J.-P. Mulet, R. Carminati, and J.-J. Greffet, "Coherent spontaneous emission of light by thermal sources," Phys. Rev. B. **69**(15), 155412 (2004).

[81] J.Le. Gall, M. Olivier, and J.-J. Greffet, "Experimental and theoretical study of reflection and coherent thermal emission by a SiC grating supporting a surface-phonon polariton," Phys. Rev. B. **55**(15), 10105–10114 (1997).

[82] J.-H. Lee, J.C.W. Lee, W. Leung, M. Li, K. Constant, C.T. Chan, and K.-M. Ho, "Polarization engineering of thermal radiation using metallic photonic crystals," Adv. Mater. **20**, 3244–3247 (2008).

[83] J.C.W. Lee and C.T. Chan, "Circularly polarized thermal radiation from layer-by-layer photonic crystal structures," Appl. Phys. Lett. **90**(5), 051912 (2007).

[84] J.-H. Lee, J.C.W. Lee, W. Leung, M. Li, K. Constant, C.T. Chan, and K.-M. Ho, "Polarization engineering of thermal radiation using metallic photonic crystals," Adv. Mater. **20**, 3244–3247 (2008).

[85] O.G. Kollyukh, A.I. Liptuga, V. Morozhenko, V.I. Pipa, and E.F. Venger, "Circular polarized coherent thermal radiation from semiconductor layers in an external magnetic field," Opt. Commun. **276**, 131–134 (2007).

[86] S.L. Wadsworth and G.D. Boreman, "Analysis of throughput for multilayer infrared meanderline waveplates," Opt. Express **18**(13), 13345–13360 (2010).

[87] S.L. Wadsworth and G.D. Boreman, "Broadband infrared meanderline quarter-wave plate," Opt. Express **19**(11), 10604–10612 (2011).

[88] S.L. Wadsworth and G.D. Boreman, "Angular sensitivity analysis of polarization and transmission metrics from crystalline, form-birefringent, and meanderline quarter-wave retarders in the LWIR spectrum," publication in-progress (2011).

[89] S.L. Wadsworth, P.G. Clem, and G.D. Boreman, "Broadband circularly-polarized infrared emission from multilayer metamaterials," publication in-progress for submission to Opt. Mat. Express (2011).

[90] B.A. Munk, *Frequency-selective Surfaces: Theory and Design*, (Wiley, New York, 2000).

[91] J.C. Vardaxoglou, *Frequency Selective Surfaces: Analysis and Design*, (Research Studies Press, Somerset, England, 1997).

[92] B.A. Munk, *Finite Antenna Arrays and FSS*, (Wiley, Hoboken, NJ, 2003).

[93] D. Shelton, J. Cleary, J. Ginn, S. Wadsworth, R. Peale, D. Kotter, and G. Boreman, "Gangbuster frequency selective surface metamaterials in terahertz band," Electronics Letters **44**(22), 1288-1289 (2008).

[94] L. Young, L.A. Robinson, and C.A. Hacking, "Meander-line Polarizer," IEEE Trans. Antenn. Propag. **21**(3), 376–378 (1973).

[95] R.S. Chu, and K.M. Lee, "Analytical model of a multilayer meander-line polarizer plate with normal and oblique plane-wave incidence," IEEE Trans. Antenn. Propag. **35**(6), 652–661 (1987).

[96] C. Terret, J.R. Levrel, and K. Mahdjoubi, "Susceptance computation of a meander-line polarizer layer," IEEE Trans. Antenn. Propag. **32**(9), 1007–1011 (1984).

[97] A.K. Bhattacharyya, and T.J. Chwalek, "Analysis of multilayer meanderline polarizer," Int. Journ. Microw. MM-Wave Comp.-Aided Engin. **7**(6), 442–454 (1998).

[98] J.S. Tharp, J.M. Lopez-Alonso, J.C. Ginn, C.F. Middleton, B.A. Lail, B.A. Munk, and G.D. Boreman, "Demonstration of a single-layer meanderline phase retarder at infrared," Opt. Lett. **31**(18), 2687–2689 (2006).

[99] J.S. Tharp, B.A. Lail, B.A. Munk, and G.D. Boreman, "Design and Demonstration of an Infrared Meanderline Phase Retarder," IEEE Trans. Antenn. Propag. **55**(11), 2983–2988 (2007).

[100] J.S. Tharp, J. Alda, and G.D. Boreman, "Off-axis behavior of an infrared meander-line waveplate," Opt. Lett. **32**(19), 2852–2854 (2007).

[101] B.J. Rubin and B. Singh, "Study of meander line delay in circuit boards," IEEE Trans. Microw. Theory Tech. **48**(9), 1452–1460 (2000).

[102] J.A. Weiss, "Dispersion and field analysis of a microstrip meander-line slow-wave structure," IEEE Trans. Mwave. Theory. Tech. **22**(12), 1194–1201 (1974).

[103] K. K. Chan, T. W. Ang, T. H. Chao, and T. S. Yeo, "Accurate analysis of meanderline polarizers with finite thicknesses using mode matching," IEEE Trans. Antenn. Propag. **56**(11), 3580–3585 (2008).

[104] J.E. Raynolds, B.A. Munk, J.B. Pryor, and R.J. Marhefka, "Ohmic loss in frequency-selective surfaces," J. App. Phys. **93**(9), 5346–5358 (2003).

[105] Z. Knittl, *Optics of thin films; an optical multilayer theory*, (Wiley, New York, NY, 1976).

[106] H.A. Macleod, *Thin-film optical filters*, (American Elsevier, New York, NY, 1969).

[107] P. A. Rizzi, *Microwave Engineering: Passive Circuits*, (Prentice-Hall, Upper Saddle River, NJ, 1988).

[108] K.C. Hwang, "Optimization of broadband twist reflector for Ku-band application," Electronics Letters **44**(3), 20082937 (2008).

[109] K.Y. Han and B.A. Lail, "Genetically-engineered meanderline twist reflector," Antennas and Propagation Society International Symposium, AP-S (2008).

[110] J.D. Hanfling, G. Jerenic, L.R. Lewis, "Twist reflector design using E-type and H-type modes," IEEE Trans. Antenn. Propag. **29**(4), 622–629 (1981).

[111] M.N.O Sadiku, *Numerical techniques in electromagnetics: 2nd edition*, (CRC Press, Boca Raton, FL, 2001).

[112] R.T. Remski, "Analysis of photonic bandgap surfaces using Ansoft HFSS," Mwave. Journ., Sept. (2000).

[113] A. Erentok and R.W. Ziolkowski, "HFSS modeling of a dipole antenna enclosed in an epsilon-negative (ENG) metamaterial shell," Antenn. Propag. Soc. Int. Symp. **3B**, 22–25 (2005).

[114] N.R. Labadie and S.K. Sharma, "A novel compact volumetric metamaterial structure with asymmetric transmission and polarization conversion," Metamaterials **4**, 44–57 (2010).

[115] J.P. Montgomery, "Scattering by an infinite periodic array of thin conductors on a dielectric sheet," IEEE Trans. Antenna Propag. **23**(1), 70–75 (1975).

[116] W.R. Folks, J.C. Ginn, D.J. Shelton, J.S. Tharp, and G.D. Boreman, "Spectroscopic ellipsometry of materials for infrared micro-device fabrication," Phys. Stat. Sol. (c) **5**(5), 1113–1116 (2008).

[117] H. Raether, *Surface Plasmons on Smooth and Rough Surfaces and on Gratings*, (Springer, Berlin Heidelberg, 1988).

[118] J.S. Tharp, D.J. Shelton, S.L. Wadsworth, and G.D. Boreman, "Electron-beam lithography of multiple-layer submicrometer periodic arrays on a barium fluoride substrate," J. Vac. Sci. Technol. B **26**(5), 1821–1823 (2008).

[119] C. Middlebrook, P. Krenz, B. Lail, and G. Boreman, "Infrared Phased-Array Antenna," Microwave and Optical Technology Letters **50**(4), 719-723 (2008).

[120] P. Krenz, J. Alda, and G. Boreman, "Orthogonal infrared dipole antenna," Infrared Physics and Technology **51**(4), 340-343 (2008).

[121] P. Garrou, "Polymer dielectrics for multichip module packaging," Proc. IEEE **80**(12), 1942–1954 (1992).

[122] M.J. Weber, *Handbook of Laser Wavelengths*, (CRC Press, Boca Raton, FL, 1999).

[123] D.F. Bezuidenhout, K.D. Clarke, and R. Pretorius, "The optical properties of YF_3 films," Thin Solid Films **155**, 17–30 (1987).

[124] J.Y. Robic, B. Rolland, J.C. Deutsch, and P. Gallais, "Ion-assisted deposition of yttrium fluoride as a substitute for thorium fluoride: Application to infrared anti-reflection coating on germanium," Proc. SPIE **2253**, 552–558 (1994).

[125] V. K. Arora, "Quantum size effect in thin-wire transport," Phys. Rev. B **23**(10), 5611–5612 (1981).

[126] J. Ginn, D. Shelton, P. Krenz, B. Lail, and G. Boreman, "Altering infrared metamaterial performance through metal resonance damping," J. Appl. Phys. **105**, 074304 (2009).

[127] D. Kim, "Performance uniformity analysis of a wire-grid polarizer in imaging polarimetry," Appl. Optics **44**(26), 5398−5402 (2005).

[128] H. Ryu, S. J. Yoon, and D. Kim, "Influence of surface roughness on the polarimetric characteristics of a wire-grid grating polarizer," Appl. Optics **47**(30), 5715−5721 (2008).

[129] K.C. Hwang, "Optimization of broadband twist reflector for Ku-band application," Electronics Letters **44**(3), 20082937 (2008).

[130] K.Y. Han and B.A. Lail, "Genetically-engineered meanderline twist reflector," Antennas and Propagation Society International Symposium, AP-S (2008).

[131] J.D. Hanfling, G. Jerenic, L.R. Lewis, "Twist reflector design using *E*-type and *H*-type modes," IEEE Trans. Antenn. Propag. **29**(4), 622–629 (1981).

[132] F. Marquier, C. Arnold, M. Laroche, J.J. Greffet, and Y. Chen, "Degree of polarization of thermal light emitted by gratings supporting surface waves," Opt. Express **16**(8), 5305–5313 (2008).

[133] K. Joulain, J.-P. Mulet, F. Marquier, R. Carminati, and J.-J. Greffet, "Surface electromagnetic waves thermally excited: Radiative transfer, coherence properties and Casimir forces revisited in the near field," Surf. Scien. Rep. **57**, 59–112 (2005).

[134] P.J. Hesketh, J.N. Zemel, and B. Gebhart, "Polarized spectral emittance from periodic micromachined surfaces. II. Doped silicon: angular variation," Phys. Rev. B. **37**(18), 10803–10813 (1988).

[135] M. Laroche, C. Arnold, F. Marquier, R. Carminati, J.-J. Greffet, S. Collin, N. Bardou, and J.-L. Pelouard, "Highly directional radiation generated by a tungsten thermal source," Opt. Lett. **30**(19), 2623–2625 (2005).

[136] N. Dahan, A. Niv, G. Biener, Y. Gorodetski, V. Kleiner, and E. Hasman, "Extraordinary coherent thermal emission from SiC due to coupled resonant cavities," J. Heat Trans. **130**, 112401 (2008).

[137] T. Setala, M. Kaivola, and A.T. Friberg, "Degree of polarization in near fields of thermal sources: effects of surface waves," Phys. Rev. Lett. **88**(12), 123902 (2002).

[138] A.V. Shchegrov, K. Joulain, R. Carminati, and J.-J. Greffet, "Near-field spectral effects due to electromagnetic surface excitations," Phys. Rev. Lett. **85**(7), 1548–1551 (2000).

[139] M. Laroche, R. Carminati, and J.-J. Greffet, "Coherent thermal antenna using a photonic crystal slab," Phys. Rev. Lett. **96**(12), 123903 (2006).

[140] B.J. Lee and Z.M. Zhang, "Coherent thermal emission from modified periodic multilayer structures," J. Heat Trans. **129**, 17–26 (2007).

[141] M. Florescu, H. Lee, A.J. Stimpson, and J. Dowling, "Thermal emission and absorption of radiation in finite inverted-opal photonic crystals," Phys. Rev. A. **72**(3), 033821 (2005).

[142] S. Enoch, J.-J. Simon, L. Escoubas, Z. Elalmy, F. Lemarquis, P. Torchio, and G. Albrand, "Simple layer-by-layer photonic crystal for the control of thermal emission," Appl. Phys. Lett. **86**(26), 261101 (2005).

[143] M. Garin, T. Trifonov, D. Hernandez, A. Rodriguez, and R. Alcubilla, "Thermal emission of macroporous silicon chirped photonic crystals," Opt. Lett. **35**(20), 3348–3350 (2010).

[144] D.L.C. Chan, M. Soljacic, and J.D. Joannopoulos, "Thermal emission and design in one-dimensional periodic photonic crystal slabs," Phys. Rev. E. **74**(1), 016609 (2006).

[145] S.-Y. Lin, J.G. Fleming, E. Chow, J. Bur, K.K. Choi, and A. Goldberg, "Enhancement and suppression of thermal emission by a three-dimensional photonic crystal," Phys. Rev. B. **62**(4), R2243–R2246 (2000).

[146] N. Dahan, A. Niv, G. Biener, V. Kleiner, and E. Hasman, "Space-variant polarization manipulation of a thermal emission by a SiO_2 subwavelength grating supporting surface phonon-polaritons," Appl. Phys. Lett. **86**(19), 191102 (2005).

[147] Z. Yang, M Zhao, and P. Lu, "How to improve the signal-to-noise ratio for circular polarizers consisting of helical metamaterials," Opt. Express **19**(5), 4255–4260 (2011).

[148] J. Ginn, D. Shelton, P. Krenz, B. Lail, and G. Boreman, "Polarized infrared emission using frequency selective surfaces," Opt. Express **18**(5), 4557–4563 (2010).

[149] A. Resnick, C. Persons, and G. Lindquist, "Polarized emissivity and Kirchhoff's law," Appl. Optics **38**(8), 1384–1387 (1999).

[150] J.J. Greffet and M. Nieto-Vesperinas, "Field theory for generalized bidirectional reflectivity: derivation of Helmholtz's reciprocity principle and Kirchhoff's law," J. Opt. Soc. Am. A. **15**(10), 2735–2744 (1998).

[151] L. Tsang, J.A. Kong, and K.H. Ding, *Scattering of Electromagnetic Waves. Theories and Applications*, (J. Wiley, New York, 2000).

[152] S.M. Rytov, Y.A. Kravtsov, and V.I. Tatarskii, *Principles of Statistical Radiophysics 3: Elements of Random Fields*, (Springer-Verlag, New York, 1989).

[153] G. S. Agarwal, "Quantum electrodynamics in the presence of dielectrics and conductors. I. Electromagnetic-field response functions and black-body fluctuations in finite geometries," Phys. Rev. A. **11**(1), 230–242 (1975).

[154] C. Henkel, K. Joulain, R. Carminati, and J.-J. Greffet, "Spatial coherence of thermal near fields," Opt. Commun. **186**, 57–67 (2000).

[155] M. Schmidt and F. Schwertfeger, "Applications for silica aerogel products," J. Non-Crys. Sol. **225**, 364–368 (1998).

[156] L.W. Hrubesh and R.W. Pekala, "Thermal properties of organic and inorganic aerogels," J. Mater. Res. **9**(3), 731–738 (1994).

[157] J.A. Ruffner, P.G. Clem, B.A. Tuttle, C.J. Brinker, C.S. Sriram, and J.A. Bullington, "Uncooled thin film infrared imaging device with aerogel thermal isolation: deposition and planarization techniques," Thin Solid Films **332**, 356–361 (1998).

[158] L.C. Klein, *Sol-gel Optics: Processing and Applications*, (Kluwer Academic, Boston, 1994).

[159] D. Shelton, K Coffey, and G. Boreman, "Experimental demonstration of tunable phase in a thermochromic infrared-reflectarray metamaterial," Opt. Express **18**(2), 1330–1335 (2010).